From Muscle–Tendon Units to Whole–Body Locomotion: Modelling Active and Passive Joint Dynamics

Erick Romo Rivera

School of Computer Science

The University of Leeds

Submitted in accordance with the requirements for the degree of

Doctor of Philosophy

January 2026

Intellectual Property

The candidate confirms that the work submitted is his own and that appropriate credit has been given where reference has been made to the work of others.

This copy has been supplied on the understanding that it is copyright material and that no quotation from the thesis may be published without proper acknowledgement.

The candidate declares that parts of the work presented in this thesis have been published in the following article. Details of the contributions by myself and other authors are provided below, including the chapter whose contents appear in:

Romo-Rivera, E., Boyle, J.H., Chakrabarty, S., Cohen, N. (2026). "The Role of Passive Mechanics in Asymmetrically Actuated Bioinspired Joints." In: Jiménez Rodríguez, A., *et al. Biomimetic and Biohybrid Systems. Living Machines 2025. Lecture Notes in Computer Science()*, vol 15582. Springer, Cham.

Author contributions. The research presented in this article is my own. Conceptualisation was developed jointly by **myself and NC.** I was responsible for the methodology, implementation, preparation of figures, and drafting of the manuscript. **NC, SC, and JHB** provided supervision, critical feedback, and general guidance throughout the project. In addition, **NC and SC** offered detailed comments on manuscript drafts and assisted with editorial refinement.

Chapter 6 is built directly on this work; it further guided the analysis and results in Chapter 7, especially Section 7.2.2.

Acknowledgements

There is no one more deserving of credit than my *pingu*, Mariana. My deepest gratitude for your unconditional love and unwavering support. Thank you for the countless things you chose to leave behind to follow me across the world in pursuit of my dreams, and then, our dreams. Without your encouragement, and your constant physical and emotional support, this work would not have been possible. This is for you, and because of you.

I would like to express my deepest gratitude to Netta Cohen and Samit Chakrabarty. Both of you welcomed me, rebuilt my confidence, and reshaped the way I think in ways that will stay with me far beyond this work. Thank you, Netta, for taking me in and helping me grow into a capable scientist. Your passion for science, relentless work ethic, and remarkable breadth of knowledge have been a constant source of inspiration. I am especially grateful that you always found space for me in an already demanding schedule. Thank you, Samit. An extraordinary scientist, and above all, a wonderful person, invariably able to connect even the most complex ideas to food facts. You welcomed me into your group and gave generously of your time, through countless discussions and conversations that never felt like supervision, but like speaking with a friend.

Special thanks to Jordan Boyle. Thank you for being the first to believe in me and in my work. Your insight and guidance have been invaluable; you are one of those rare people whose judgment is constantly right. I am deeply grateful.

My research has been strongly supported by the members of Netta's and Samit's groups. In particular, I would like to thank my office neighbour, Lukas. Your distinctive way of seeing science, and life, has inspired my work in so many different ways. I am deeply grateful for your feedback and your support throughout this journey, and I can happily say that I found a friend in you. I would also like to express my gratitude to the SChMobility Lab, and especially to Raf and Bowen. The many conversations we shared, scientific and otherwise, brought lightness, perspective, and a sense of community that made the PhD experience far richer than the work alone.

My time in Leeds brought into my life amazing people who made the city feel like home. A special mention goes to Moisés, whom I thank for becoming more than a friend, a brother. We have shared laughter and travels, stories and night outs, difficult moments, and above all, many pints. You are one of those people who enter your life and never truly leave. The same is true of Abraham, Loza

and Guada. Thank you guys for always being there to share a laugh or two, for your constant presence, and for the quiet, steady support that mattered more than you may realise. I cannot let Daniel, Daisy and Victor go unnoticed here. Thank you for the moments of lightness, the shared laughter, and the simple presence that made the difficult days easier and the good ones brighter. Friends like you quietly shape the journey in ways that only become clear with time.

My heartfelt thanks go to the staff of Lupe's Cantina Mexicana. In particular, to Igor and the García family: Rudy, Tansy, Delilah, Joaquin and Nacho. You guys have made Mariana and me fell as if we were in Mexico, even when we were far from it. I cannot fully express my gratitude for everything you gave us and all that you did for us. You became our family.

Finally, I wish to thank my parents, Edith and Ramses. Your love, guidance, and unwavering support have shaped who I am today. You have always made me feel supported and encouraged, no matter how far apart we have been. This work is a reflection of everything you have given me, an it stands because of you.

Abstract

Animal movement emerges from the combined action of neural activation, muscle dynamics, and the passive mechanical properties of the body. Muscles and joints do not simply relay neural commands but transform them through intrinsic viscoelastic dynamics, shaping how forces and motion emerge. Indeed, how active and passive forces interact across muscles and joints in the body remains a fundamental open question in biomechanics. This thesis addresses this question by focusing on the joint as a fundamental unit of neuromechanical organisation. Here we develop a hierarchical modelling framework that progress from a single muscle-tendon unit representation, to single- and antagonistic- muscle joint models, and ultimately to a multi-joint, whole-body insect model. At each level, the balance between active muscle-like actuation and passive joint viscoelasticity is systematically analysed to identify the mechanisms that govern joint torque generation and movement. Using experimental data from the locust femur-tibia as benchmark, the results showed that a single joint model actuated by a single muscle-tendon unit successfully reproduced realistic extension-flexion cycles and revealed that history-dependent mechanisms in muscle dynamics play a key role in shaping motion. Extending the model to include antagonistic muscle actuation revealed distinct dynamics regimes governed by the balance between active and passive contributions. These regimes determine joint amplitude, stability and frequency response under symmetric and asymmetric configurations. We show that joint passive can effectively compensate for imbalances between asymmetric actuators, preserving the dynamic range of the joint within specific viscoelastic regimes. Finally, the joint model was embedded in a physics-based simulator and used as a modular building block to construct multi-joint limbs and a whole-body insect model inspired by dung beetle morphology. The dynamical regimes identified at the joint level re-emerge in this mechanically more realistic setting, indicating that these regimes are intrinsic to muscle-joint mechanics. Under a simple closed-loop control framework, the insect model reproduced stable tripod-like walking and revealed an operational regime in which passive joint mechanics and low-level control are sufficient for robust locomotion, even in uneven terrain. Taken together, these results advance our understanding of how active and passive properties interact to shape joint dynamics and offer guidance for the design of bioinspired robotic system, in which viscoelastic properties can be exploited rather than neglected.

List of Variables

Throughout this thesis, a hat ($\hat{\cdot}$) denotes a dimensionless quantity, and an over-dot ($\dot{\cdot}$) denotes differentiation with respect to time.

Muscle–Tendon Unit (MTU) Model

$\boldsymbol{i}$	MTU index, $i = \{\text{fl, ext}\}$ (flexor, extensor)
$\boldsymbol{F_i}$	Total force generated by MTU i
$\boldsymbol{f_a^{(i)}}$	Active contractile force component
$\boldsymbol{f_p^{(i)}}$	Passive force component
$\boldsymbol{\kappa_a^{(i)}}$	Active spring stiffness, $\kappa_a = \kappa_{\max}\,\sigma(A_m)$
$\boldsymbol{\kappa_p^{(i)}}$	Passive spring constant
$\boldsymbol{\kappa_{\max}^{(i)}}$	Maximum active stiffness (constant)
$\boldsymbol{\beta_a^{(i)}}$	Active damping coefficient, $\beta_a = \beta_{\max}\,\sigma(A_m)$
$\boldsymbol{\beta_p^{(i)}}$	Passive damping coefficient
$\boldsymbol{\beta_{\max}^{(i)}}$	Maximum active damping (constant)
$\boldsymbol{L_m^{(i)}}$	Current muscle (spring) length
$\boldsymbol{\dot{L}_m^{(i)}}$	Muscle contraction rate
$\boldsymbol{L_t^{(i)}}$	Activation-dependent tension length
$\boldsymbol{L_0^{(i)}}$	Muscle resting length
$\boldsymbol{L_{\min}^{(i)}}$	Minimum muscle length at full activation
$\boldsymbol{A_m^{(i)}}$	Muscle activation signal
$\boldsymbol{\sigma(\cdot)}$	Piece-wise linear clipping function, clips its argument to $[0, 1]$

Joint Model

$\boldsymbol{\theta}$	Joint angle
$\boldsymbol{\dot{\theta}}$	Angular velocity
$\boldsymbol{\ddot{\theta}}$	Angular acceleration
$\boldsymbol{\theta_{\text{rest}}}$	Rest joint angle

$\boldsymbol{\theta_{\min}}$	Lower range-of-motion limit
$\boldsymbol{\theta_{\max}}$	Upper range-of-motion limit
$\boldsymbol{\Delta\theta}$	Angular displacement from rest, $\Delta\theta = \theta - \theta_{\text{rest}}$
$\boldsymbol{r}$	Muscle moment arm
$\boldsymbol{r_{\text{ext}}}$, $\boldsymbol{r_{\text{fl}}}$	Extensor and flexor moment arms
$\boldsymbol{F_e}$, $\boldsymbol{F_f}$	Extensor and flexor forces
$\boldsymbol{F_{\text{ext}}}$	Extensor MTU force
$\boldsymbol{F_{\text{effective}}}$	Combined effective single-MTU force
$\boldsymbol{T_e}$, $\boldsymbol{T_f}$	Extensor and flexor torques
$\boldsymbol{T_{\text{MTU}}}$	Total muscle torque on the joint
$\boldsymbol{T_{\text{net}}}$	Net joint torque
$\boldsymbol{T_{\text{pass}}}$	Passive joint torque
$\boldsymbol{T_{\text{in}}}$	Torque input supplied to the MuJoCo joint
$\boldsymbol{T_{\text{phys}}}$	Physical (rescaled) torque
$\boldsymbol{\kappa_j}$	Passive joint stiffness
$\boldsymbol{\beta_j}$	Passive joint damping
$\boldsymbol{J}$	Moment of inertia of the distal link, $J = \frac{1}{3}ml^2$
$\boldsymbol{m}$	Mass of the distal link
$\boldsymbol{l}$	Length of the distal link
$\boldsymbol{g}$	Gravitational acceleration

Nondimensional Parameters

$\boldsymbol{\tau}$	Characteristic time scale
$\boldsymbol{\hat{L}_m}$	Dimensionless muscle length
$\boldsymbol{\hat{L}_t}$	Dimensionless tension length
$\boldsymbol{\hat{t}}$	Dimensionless time
$\boldsymbol{\hat{F}_i}$	Dimensionless total MTU force
$\boldsymbol{\hat{f}_a}$	Dimensionless active MTU force
$\boldsymbol{\hat{f}_p}$	Dimensionless passive MTU force
$\boldsymbol{\eta_a^{(i)}}$	Active stiffness-to-damping ratio
$\boldsymbol{\eta_p^{(i)}}$	Passive (MTU) stiffness-to-damping ratio
$\boldsymbol{\eta_j}$	Passive (joint) stiffness-to-damping ratio

$\boldsymbol{\mu_j^{(i)}}$	MTU active-to-passive damping ratio
$\boldsymbol{\mu_c}$	Active-to-passive (MTU-to-joint) ratio
$\boldsymbol{\mu_m}$	MTU asymmetry parameter
$\boldsymbol{\gamma}$	Gravitational-to-viscous force ratio (model-specific; see note below)
$\boldsymbol{\hat{J}}$	Dimensionless moment of inertia (model-specific; see note below)
$\boldsymbol{\tau_a}$	Active intrinsic time constant
$\boldsymbol{\tau_p}$	Passive intrinsic time constant
$\boldsymbol{S_m}$	Torque scaling factor (whole-body insect model)

Muscle Activation Model

$\boldsymbol{t_i}$	Time of discrete spike event i
$\boldsymbol{U(t)}$	Excitatory drive signal
$\boldsymbol{\tau_s}$	Spike-response timescale
$\boldsymbol{A_m(t)}$	Muscle activation state, with range $[0,\ A_{m,\max}]$
$\boldsymbol{A_{m,\max}}$	Maximum activation level
$\boldsymbol{C_a}$	Activation capacity constant
$\boldsymbol{g_a}$	Deactivation rate constant
$\boldsymbol{g_u}$	Neural-input gain (neuromuscular transmission gain)
$\boldsymbol{\tilde{\tau}_a}$	Activation time constant
$\boldsymbol{g_{a,\max}}$	Maximum contribution of the adaptive deactivation component
$\boldsymbol{S_{g_a}}$	Steepness of the sigmoidal g_a transition
$\boldsymbol{A_{m,\,\mathrm{off}}}$	Activation level at which the reduction in g_a becomes pronounced
$\boldsymbol{g_{a,\,\mathrm{off}}}$	Constant offset ensuring a non-zero lower bound on g_a

Notes on model-specific symbols.

- γ takes a model-specific form: in the single-MTU joint model $\gamma = \dfrac{mgl}{2(L_0^{\mathrm{ext}})^2\,\beta_{\max}^{\mathrm{ext}}}\,\tau$, whereas in the antagonistic-MTU joint model $\gamma = \dfrac{mgl}{2\beta_j}\,\tau$.
- $\hat{J}$ is likewise model-specific: single-MTU $\hat{J} = \dfrac{J}{(L_0^{\mathrm{ext}})^2\,\beta_{\max}^{\mathrm{ext}}\,\tau}$; antagonistic-MTU $\hat{J} = \dfrac{J}{\beta_j\,\tau}$.

Contents

List of Figures

List of Tables

Chapter 1

Introduction

The beauty of nature lies in its capacity to give rise to complex, adaptive behaviour from interaction among many individual components. Across scales, biological systems exhibit a remarkable ability to organise, regulate, and respond to their environment, producing behaviour that is both robust and flexible. Nowhere is this more evident than in animal movement, where neural signals, muscles, and mechanical structures are coordinated to generate purposeful motion. Indeed, rather than being imposed by control alone, biological movement emerges from the tight coupling between neural control circuitry and the biomechanics of the body, as well as the interaction with the environment.

How do neural control mechanisms and biomechanics combine to yield coordinated motion? This seemingly simple yet deeply fascinating question has drawn sustained attention of thousands of researchers across multiple disciplines. All sharing the common goal of deciphering the underlying principles of animal movement. Despite major advances in this field, a complete understanding of the complexity of animal movement remains out of reach.

At the core of the coupling between control and biomechanics lies the transformation of neural commands into physical forces and motion. Neural activity does not act directly on the body, but is mediated by the musculoskeletal system, whose material and dynamical properties shape how control signals are expressed over time. Muscles do not merely relay neural commands; through activation and contraction dynamics they transform neural input into force, acting as dynamical systems that filter, delay, and scale the signal. These forces propagate via tendons and skeletal structures, while the mechanical properties of tissues further modulate their effects. As a result, movement is not simply prescribed by the nervous system alone but emerges from the interaction among neural drive, muscle dynamics, and the passive mechanical structure through which those forces act.

Addressing the full complexity of how control and mechanics interact to produce ani-

mal movement spans multiple levels of organisation and lies beyond the scope of a single thesis. For this reason, the present work focuses on a specific but fundamental aspect of this problem: how muscle activity is transformed into torque at an individual joint through muscle–tendon dynamics, joint geometry, and intrinsic mechanical properties. By concentrating on this mechanical interface, the thesis isolates a level of description at which active muscle forces and passive joint mechanics interact to shape motion, without attempting to model the entirety of neural control or behavioural complexity. While the principles of active-passive interaction at the joint are general, the empirical grounding and models developed in this thesis are drawn mainly from insects, whose small scale makes intrinsic mechanical properties especially influential relative to inertial and gravitational loads.

At the joint level, torque generation is shaped not only by active muscle contraction but also by intrinsic passive mechanical properties. These properties arise from elements including ligaments, joint capsules, cartilage, synovial structures, tendons (or apodemes in insects), fascia and titin fibres of muscles [40, 69, 79, 118], and they strongly shape how forces are transmitted and dissipated. In fact, experimental studies have shown that passive joint mechanics contribute substantially to joint behaviour in invertebrates and small vertebrates [3, 63, 64, 90]. Despite the growing interest in muscle-joint passive properties [32, 44, 47, 112] and their inclusion in many biomechanical modelling frameworks [47, 48, 74, 85, 98, 117, 127], the passive mechanical behaviour of joints remains incompletely characterised. As a result, the contribution of passive structures to the interplay with active muscle forces, and to the stability and temporal characteristics of joint motion, is still not fully understood.

Importantly, the question concerning how joint torque arises from the interaction between active actuation and passive mechanical properties is not confined to biological systems. In the design of robotic limbs, joints likewise must transform actuation into controlled motion while maintaining stability and robustness under uncertainty and external disturbances. Yet many robotic systems often minimise or omit viscoelastic elements at the joints. Rather than being leveraged as a functional resource, viscosity and elasticity are often treated as sources of energy dissipation, not contributors to torque production or disturbance rejection. Improving our understanding of how passive and active elements interact at the joint level could therefore inform biological theory, and also guide the design and control of robotic systems that tune passive stiffness and damping alongside control to exploit, rather than suppress, intrinsic mechanical dynamics.

A natural question is whether the prominence of passive joint mechanics is specific to small animals or holds across scales. Body size is known to strongly condition the relative importance of the forces acting at a joint. In insects, for example, elastic and viscous forces dominate joint behaviour. In larger animals such as humans, on the other hand, inertia and gravitational forces play a greater role than passive viscoelastic forces, so the same

passive structures occupy a different position in the overall force balance. The methodology developed in this thesis makes this dependence explicit by capturing the relative contribution of elastic, viscous, inertial, and gravitational forces with parameters that scale with body size. The claim here is therefore not that passive mechanics dominate universally, but that they are functional participants whose influence is pronounced at small scales and modulated, although not eliminated, as size increases.

1.1 Research Questions and Approach

Building upon these considerations, this thesis is guided by a set of research questions concerned with the organisation of joint dynamics and their role in shaping movement. Specifically, the work addresses the following questions.

1. How does the interaction between active muscle-tendon dynamics and passive joint viscoelasticity shape joint torque generation and motion?
2. Under what conditions do passive joint mechanics dominate, stabilise, or meaningfully constrain joint motion, and to what extent can intrinsic joint mechanics themselves structure movement without requiring complex or finely tuned control strategies?
3. How can insights into passive joint dynamics be applied to the design and control of robotic joints?

Addressing these questions requires an approach that allows the biomechanical properties of the system to be systematically tuned while accounting for its physical interactions with the environment. Computational modelling provides a particularly effective framework in this regard, as it enables explicit specification of individual system components, offers access to mechanical quantities that are difficult to measure in animals, and allows systematic exploration of how changes in biomechanical parameters shape joint behaviour. Moreover, modelling makes it possible to probe regimes and scenarios in which the system is pushed toward its functional limits. Accordingly, this thesis adopts a modelling approach to study the intrinsic mechanical processes underlying joint torque generation, examining them through mathematical formulations and computational simulations. The fact that this work is situated within the School of Computer Science naturally complements this methodology, providing the analytical and computational tools required to address the questions posed.

The modelling approach adopted in this thesis follows a bottom-up progression across three levels of organisation: muscle, joint, and whole-body dynamics. Fig. 1.1 shows a schematic of this progression. At the first level, muscle actuation is represented in a generic

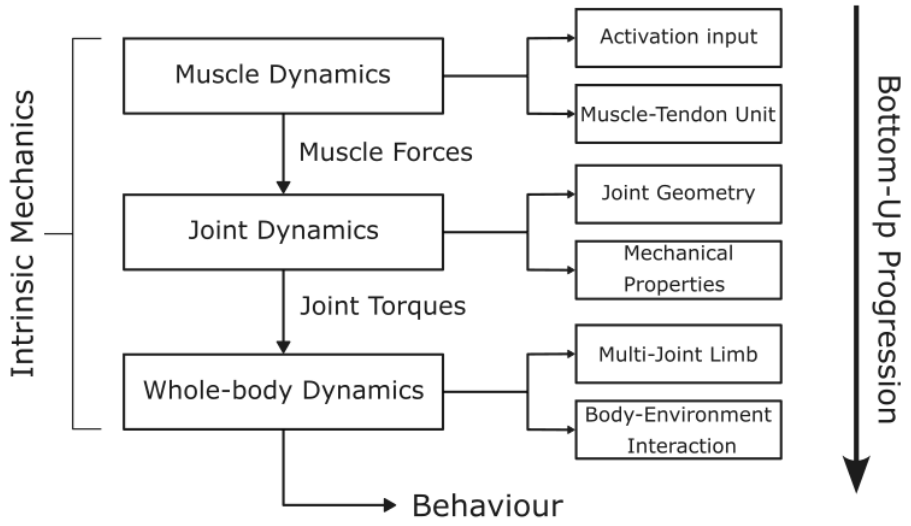

Figure 1.1: Bottom-up modelling framework adopted in this thesis. Muscle–tendon dynamics generate forces that act through joint geometry and passive joint mechanics to produce joint torques and motion. Joint-level models are analysed in isolation using mathematical and physics-based approaches and are subsequently embedded within multi-joint limbs and a whole-body model to examine the emergence of coordinated behaviour.

and abstracted form of the muscle–tendon unit and its activation, capturing essential dynamics of force production without committing to specific details. At the second level, the muscle-like actuation is coupled to joint dynamics to examine how force is transformed into torque through joint geometry and intrinsic mechanical structure. The mapping from muscle force to joint torque is studied using complementary mathematical and physics-based models. At the third level, the resulting joint models are embedded within multi-joint limbs and a complete articulated body to demonstrate how mechanical principles identified at the joint scale extend to coordinated, whole-body motion. In this way, the thesis seeks to characterise essential mechanical interactions at the joint level while remaining sufficiently general to support biological interpretation and to inform the design and control of engineered systems.

1.2 Thesis Outline

This thesis is organised to progressively build conceptual and methodological foundations for understanding joint torque generation, before applying these ideas to increasingly integrated joint models.

Chapter 2 provides the biological and theoretical background required for contextualising this work. It reviews relevant concepts in muscle–tendon dynamics, passive joint mechanics, and biomechanical modelling, and situates the thesis within existing literature and motivates the need for a joint-centred perspective on movement generation.

Chapter 3 introduces the conceptual modelling framework adopted in the thesis. The aim of this chapter is to present a set of computational joint models that span different levels of complexity, outlining their structure and scope while highlighting how each model captures distinct aspects of joint dynamics. Subsequently, Chapter 4 presents the mathematical formulations and computational methods underlying the models introduced previously. This chapter details the governing equations, parameter definitions, and numerical implementation used throughout the thesis.

Chapter 5 focuses on a single joint actuated by a single muscle–tendon unit, using a locust joint as a biological case study. This chapter examines how passive joint mechanics interact with muscle activation to shape joint torque and motion, and evaluates the extent to which experimentally observed kinematics can be reproduced without complex control strategies.

Chapter 6 extends this analysis by introducing an antagonistic muscle configuration within a single joint. This chapter investigates how the balance between active and passive elements gives rise to distinct dynamical regimes, and how these regimes structure joint behaviour across symmetric and asymmetric configurations.

Chapter 7 embeds the joint-level principles developed in earlier chapters within a whole-body insect model. This chapter examines how joint-level mechanics scale to multi-joint interactions and coordinated limb motion, and assesses whether insights derived from simplified joint models remain informative in more complex mechanical systems.

Finally, Chapter 8 synthesises the findings of the thesis, discussing their implications for understanding biological joint mechanics and for the design and control of robotic limbs. The chapter highlights key contributions, limitations, and avenues for future work.

1.3 Contributions

The modelling framework developed in this thesis builds upon established representations of muscle and joint dynamics. The single muscle–tendon unit template is based on the model introduced by Boyle *et al.* [14], while the joint dynamics takes inspiration on several existing biomechanical formulations [85, 98, 116, 127]. Rather than proposing entirely new component models, the contribution of this work lies in how these elements are combined,

reformulated, and systematically analysed.

A central contribution of the thesis is the formulation, implementation, and numerical validation of a nondimensional representation of the joint equations of motion. This framework enables identification of key dimensionless parameters that govern the interaction between active muscle–tendon dynamics and passive joint viscoelasticity, providing a unifying description of joint behaviour across parameter regimes and scales.

Using this framework, the thesis presents a detailed exploration of the dynamic response of the joint to twitch-like muscle actuation, including: i) reproducing realistic passive joint behaviour, consistent with that observed in insect joints; ii) characterisation of the temporal structure of passive joint motion; and iii) estimation of mechanical parameters that yield biologically plausible passive responses, grounding the model in experimental observations.

The thesis further examines joint dynamics under antagonistic muscle actuation using the same modelling framework, including: i) identification of distinct dynamical regimes arising from passive joint mechanics alone, each characterised by qualitatively different response properties; ii) analysis of the interaction between active and passive elements under symmetric actuation, where antagonistic muscles possess equal strength; and iii) elucidation of the role of passive joint mechanics under asymmetric actuation, where muscles differ in strength.

Finally, the joint model is extended beyond isolated joint dynamics toward multi-joint and whole-body analysis, including: i) generalisation of the joint formulation as a modular building block for viscoelastic, multi-joint limbs; ii) integration of these limbs into a whole-body insect model based on the dung beetle; and iii) evaluation of whole-body model walking gait performance under low-level control, with particular emphasis on forward speed and distance travelled.

Chapter 2

Background

The purpose of this chapter is to establish the biological and biomechanical foundations necessary to contextualise the work presented in this thesis. It begins with Section 2.1, providing overview of muscle mechanics, input activation and force production, before introducing how muscles interact with joints to generate torque and drive limb dynamics (Section 2.2. Building on this, the principles of neuromechanical control and the role of passive mechanics in locomotion are outlined in Section 2.3. The discussion then narrows to insect muscle-joint mechanics (Section 2.4, outlining why insects provide a powerful model system for studying the coupling between active and passive forces. Finally, Section 2.5 reviews existing muscle and joint models in computational biomechanics and their relevance for small-scale limbs.

2.1 Muscles as Biological Actuators

Muscles are key elements of animal movement as they act as the main source of actuation. Through their response to neural signals, muscles generate contractile forces that are transformed into joint torques and limb motion [28]. Although often compared to motors and other types of engineered actuators, biological muscles differ fundamentally from these due to their complex biophysics, nonlinear behaviour, and multi-scale organisation.

The foundations of our understanding of muscle contraction dates back to the late 18th century. Luigi Galvani's experiments on frog legs demonstrated that nerves are electrically coupled to muscle fibres, and that electrical signals transmitted along the nerve can initiate muscle contraction [15]. Based on this experiment, scientists have refined the idea that muscles respond to electrochemical signals transmitted though nerves.

A major theoretical advance came with the Hodgkin-Huxley framework, initially developed for the squid giant axon [60]. This framework provided the mathematical foundation for describing action potential generation and propagation, forming the conceptual bridge between neural excitation and muscle activation. Subsequent work extended these ideas to motor units, the fundamental functional unit of muscle activation, and to activation dynamics, capturing how muscle force develops and decays in response to neural input.

These developments laid the grounds for muscle electrophysiology and clarified how neural signals travel to muscle fibres. However, they do not entirely explain how electrical activation is transformed into mechanical force. Bridging this gap requires a shift in perspective: from electrophysiology to mechanics. This shift must introduce the work of Archibald Hill, who approached muscle not as an electrical system, but a force-producing actuator. Through his experiments on isolated muscles, Hill characterised the fundamental mechanical relationships governing muscle contraction, most notably the force-velocity relationship. One of Hill's key insights was that muscle contraction is an energetically active process, whereas relaxation occurs without additional energy input and is largely governed by passive processes [59].

Based on this, Hill proposed a muscle model composed of three main elements: a contractile element in series with a damped elastic spring, together in parallel with a damped spring [59]. This model provided the first quantitative description of how activated muscle generates force, and lays the foundation for treating muscle as a mechanical component within a dynamics system. Importantly, it treats muscle dynamics as a lumped mechanical actuator rather than as a microscopic contractile medium, with neural excitation as the input and tensile muscle-tendon force as the output. Mechanically, the elements of this model act together as a viscoelastic actuator whose force depends on muscle length, shortening and lengthening velocity, and history of deformation.

The contractile element represents the active, force-generating capacity of the muscle and is the only component directly modulated by neural excitation. In modelling terms, neural excitation becomes, typically, a first-order activation dynamics that filters the control input before it reaches the contractile element [51, 124, 126]. This limits how quickly muscle force can change. However, this force depends not only on activation level, but also on the length and shortening or lengthening velocity of the muscle fibres. These dependencies capture two fundamental experimental observations: a force-length relationship reflecting the geometry of actin-myosin overlap [38, 58, 62, 96], and a force-velocity relationship [2, 59, 68]. Thus, the relationships define how much force an activated muscle can produce under different mechanical conditions, as well as constrain the operating range of muscle within a dynamical system.

These relationships provide the contractile element with effective stiffness and damping

properties that vary with activation level, muscle length and contraction velocity [14, 126]. Stiffness and damping are mechanical concepts used throughout this thesis to describe the behaviour of muscles and joints. Therefore, it is worth to clearly define these concepts. Stiffness refers to the resistance of a system to deformation and is defined as the relationship between force and displacement. The related concept of compliance describes the extent of elastic deformation under load and can be viewed as the inverse of stiffness. Damping characterises the resistance of a system to motion that is proportional to velocity and is associated with the dissipation of mechanical energy. Two further terms used throughout this thesis require clarification. On the one hand, active stiffness and damping refer to the mechanical properties of the muscle-tendon unit that are modulated by neural activation; thus they are present only when the muscle receives an activation signal. On the other hand, passive stiffness and damping refer to the mechanical properties that contribute to joint mechanics independently of neural activation, arising from the intrinsic material properties of the tissues involved. Clarified these, the force-length relationship contributes stiffness dependent on activation, and the force-velocity relationship introduces a nonlinear, direction-dependent dissipative behaviour that acts analogously to damping that resists rapid shortening and strongly opposes lengthening [126].

On the other hand, the series and parallel elements act passively to shape how contractile force is transmitted and regulated. The series element introduces compliance between the contractile element and the acting point, allowing muscle length and velocity to differ from the overall muscle-tendon length changes. The parallel element represents viscoelastic properties of muscle tissue itself, and generates force independent of activation when the muscle is stretched beyond its resting length [56, 112].

Viewed as a whole, the Hill model clarifies why muscle cannot be treated as a simple motor. The properties of its elements vary with posture, loading, and activation. Indeed, these properties are not incidental in locomotion, they are the primary mechanism by which animals tune limb dynamics, redistribute mechanical work between tissues, and achieve robust movement.

2.2 Muscle-Joint Coupling and Joint Dynamics

While biological muscles generate force and their models describe force production at the actuator level, movement arises only when those forces act across joints to produce rotation. Muscles transmit tensile forces to skeletal elements via tendons in vertebrates and via cuticular apodemes in arthropods (*e.g.* insects and crustaceans), generating torques whose magnitude depends on both muscle force and joint geometry. Consequently, joint dynamics represents the essential link between muscle mechanics and limb motion. Overall,

joints transform muscle force into rotational dynamics that govern posture, stability and locomotion.

The conversion of muscle force into joint torque is fundamentally governed by musculoskeletal geometry. In biomechanical modelling, muscle–tendon units are commonly idealised as frictionless tensile elements that connect skeletal segments in vertebrates or exoskeletal structures in arthropods [110, 126, 127]. Under this assumption, each muscle transmit a single tensile force along a defined line of action between its attachment points. The geometry of this line of action determines both where the force is applied and the direction in which it acts relative to the joint. As a result, the muscle-tendon unit generates a torque about the joint whose magnitude depends on the perpendicular distance between the joint centre of rotation and the force line of action. This torque, T, can be expressed as

$$T = rF\,,$$

where r is the muscle moment arm and F the muscle force. The moment arm therefore sets the mechanical advantage of the muscle and determines how effectively muscle force is converted into joint rotational motion.

In general, moment arms vary with joint angle due to changes in muscle routing and attachment geometry. An equivalent and widely used definition of the muscle moment arm is given by the tendon-excursion formulation [9]. This relates joint rotation to changes in muscle-tendon length under the assumption that this length changes arise purely from joint rotation and not from elastic stretch of the tendon. Consequently, the moment arm can be defined as the partial derivative of muscle-tendon length, L, with respect to joint angle,

$$r = \frac{\partial L}{\partial \theta}\,.$$

This definition highlights that the moment arm quantifies how joint rotation induces muscle-tendon length changes, independent of force magnitude. As such, it provides a general description of muscle-joint coupling, particularly useful in computational models where muscle-tendon length is expressed as a function of joint configuration.

Through the geometric coupling between muscles and joints, muscle-tendon units contribute not only to joint torque generation but also to the effective stiffness and damping of the joint. Joint stiffness describes how joint torque emerges from muscle force-length properties and antagonistic co-contraction [1, 54, 114, 127]. Because muscle moment arms generally vary with joint angle, joint stiffness is posture dependent and can change substantially across the range of motion. Joint damping, on the other hand, characterises velocity-dependent resistance to motion and reflects energy dissipation arising from the intrinsic force-velocity relationship of muscle contraction, viscoelastic properties of biological

tissues, and internal friction. In addition to viscoelasticity derived from muscles, joints possess passive viscoelastic structures intrinsic to the joint itself, such as ligaments, cartilage, and cuticular elements, which act mechanically in parallel with muscle-tendon units [32, 47] and introduce passive torques that may assist or resist motion [3, 63]. Together, these stiffness and damping properties determine how the joint resists and responds to angular displacement and velocity, shaping its response to muscle activation, external loads, and perturbations during locomotion.

2.3 Neuromechanical Control of Joint Dynamics

Joint movement arises from the coordinated interaction between neural signals and muscle mechanics. Muscles serve as the primary actuators in biological systems, converting neural excitation into mechanical force. This section examines the physiological mechanisms and modelling principles that govern this transformation. Muscles are organised to receive signals from the central nervous system via motor neurones. When a motor neurone is sufficiently stimulated, an action potential propagates along its axon reaching specialised synapses known as neuromuscular junctions. Here, neurotransmitter release initiates an action potential in the muscle fibre membrane, leading to depolarisation and calcium ion release within the fibre, which ultimately triggers contraction [37]. When neural excitation ceases, action potentials are no longer generated and calcium ions are actively transported back into intracellular storage sites, allowing the muscle fibres to relax. This relaxation process is generally slower than contraction because calcium transport requires energy to move ions against their concentration gradient [124]. Consequently, muscle force development and decay are temporally asymmetric, a property with important implications for movement dynamics and control.

The central nervous system modulates muscle force primarily by varying the number of action potentials delivered to the muscle and the rate at which they arrive. A single action potential evokes a brief twitch-like response, where force rises rapidly, reaches a peak, and then decays more slowly back to baseline, *i.e.* zero force [17]. When action potentials arrive as a train, a subsequent twitch can begin before the preceding twitch has fully relaxed; thus, the resulting temporal overlap produces summation, so the net force increases with each closely spaced impulse [93, 94]. As firing frequency is raised further, individual twitches merge and can no longer be distinguished. At this point, force approaches a sustained maximum—tetanic contraction, at the corresponding tetanic frequency [52, 124]. By modulating firing frequency, the central nervous system smoothly scales muscle output from single-twitch forces to maximal tetanus, thereby achieving a wide dynamic range of controllable force [113].

Moreover, the nervous system controls the amount of muscle force by recruiting only some of the muscle fibres available within a whole muscle. To do so, the muscle is structured into motor units: fundamental units composed of a single motor neurone and the muscle fibres it innervates. Motor units vary widely in size, with small motor units innervating relatively few fibres and providing fine force control, and larger motor units innervating many fibres and producing greater force [16, 61]. To meet task demands, the central nervous system adjusts the number of active motor units according to the size principle, first described by Henneman [55], whereby small, fatigue-resistant motor units are recruited first, followed by progressively larger and more forceful units as required. This recruitment strategy allows smooth gradation of force, as well as delays the onset of fatigue during low-intensity movements. Through the combined regulation of motor unit recruitment and firing frequency, the nervous system can modulate muscle force output for a wide range of tasks, providing both precision and adaptability in movement control.

Neural excitation specifies the timing and intensity with which a muscle is driven. However, the resulting mechanical response is shaped by the activation dynamics of the muscle. Through the biomechanical process of excitation-contraction coupling within the muscle fibres, neural signals are transformed into a time-varying muscle activation state [126]. Muscle activation reflects the combined effects of calcium release following action potentials, calcium binding to the contractile machinery, and subsequent calcium reuptake, and therefore embodies the intrinsic delays and asymmetries in force development and relaxation described above. As a result, activation acts as a dynamic filter on neural input, limiting the rate at which muscle force can rise or fall.

From a modelling perspective, muscle activation is commonly represented as an explicit state variable that links neural excitation to force generation [126]. Activation dynamics are typically approximated using low-order differential equations that capture the asymmetric rise and decay of activation observed experimentally. In this framework, neural excitation serves as the input to the activation model, while muscle activation evolves continuously in time according to characteristic time constants for activation and deactivation. A commonly used formulation is

$$\frac{dA(t)}{dt} = \frac{u(t) - A(t)}{\tau},$$

where $u(t)$ denotes the excitatory signal from motor neurone to muscle, $A(t)$ the muscle activation state, and τ a the time constant determining the characteristic rate of change of activation. Typically, both excitation and activation signals are normalised to vary between values of 0, representing no excitation, and 1, representing maximum excitation corresponding to fused tetaninc contraction with all motor units recruited. Despite its simplicity, this formulation captures the essential temporal characteristics of excitation-contraction and it is widely used in biomechanical and neuromechanical models [35, 51, 85,

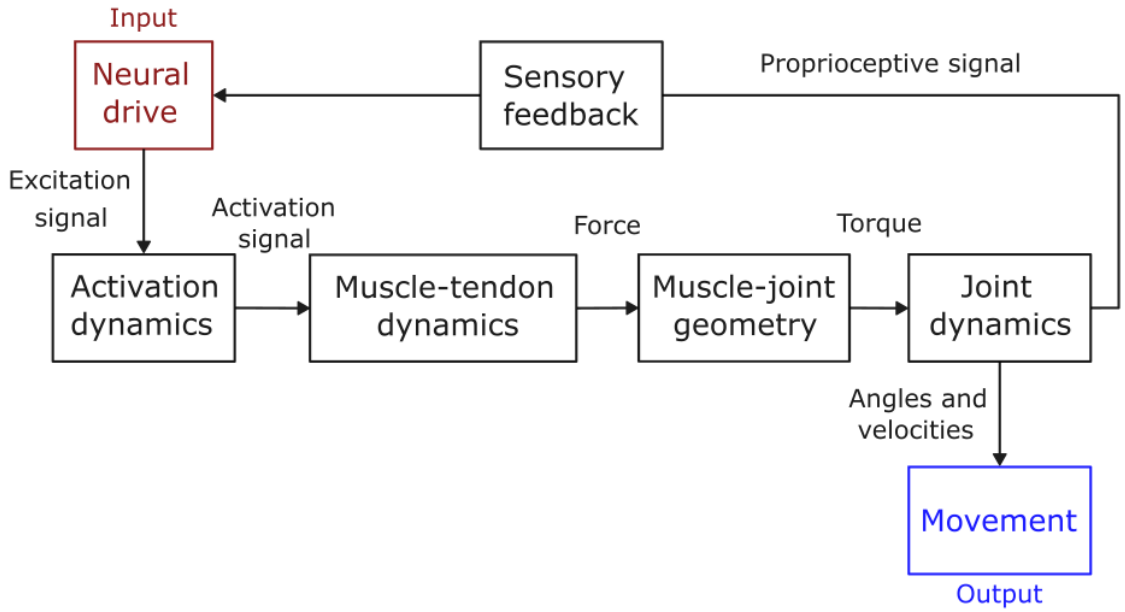

Figure 2.1: Schematic overview of the neuromechanical framework. Neural drive is transformed through muscle activation dynamics into muscle–tendon force generation, which, through muscle–joint geometry, produces joint torques and joint dynamics that give rise to movement. Sensory feedback from the mechanical state of muscles and joints closes the control loop by influencing neural drive. Passive mechanical properties of muscles and joints contribute alongside active force generation throughout the neuromechanical pathway.

88, 111, 127].

Within muscle modelling, muscle activation provides the direct link between neural excitation dynamics and mechanical force production. The activation state scales the force the contractile element can generate, thereby modulating how much of the maximum force of the muscle can be produced at a given length and contraction velocity. Indeed, activation does not generate force on its own but regulates the contribution of the active force-length and force-velocity relationships that define contractile dynamics. Hence, the instantaneous muscle force depends on activation dynamics as well as on the current mechanical state of the muscle.

The processes linking neural excitation to muscle activation and muscle-tendon force generation into joint torques and movement define a feedforward control pathway from neural signals to mechanical output. In biological systems, however, movement is not governed by feedforward control alone. Sensory feedback arising from the mechanical state of muscles and joints provide proprioceptive information about muscle length, contraction velocity, and force, as well as joint position and motion. These can influence neural excitation trough spinal and supraspinal pathways [45]. Even though the detailed organisation

of sensory feedback is beyond the scope of this thesis, it is important to recognise that neuromechanical control operates as a closed-loop system in which feedforward commands interact with intrinsic muscle-joint mechanics and sensory feedback to regulate movement. Fig. 2.1 illustrates a schematic overview of the neuromechanical framework described here. It shows how the feedforward transformation from neural signals through activation dynamics, muscle–tendon mechanics, and joint dynamics gives rise to movement, and how sensory feedback pathways close the control loop.

The neuromechanical framework outlined in Fig. 2.1 captures the general principles of movement generation. While these principles apply broadly, their relative contributions and organisation range widely between organisms. How they manifest in practice depends on the mechanical regime in which an animal operates, which is shaped by factors such as body size, limb morphology, and the viscoelastic properties of muscles and joints [105, 122]. These factors influence the relative importance of inertial, elastic, and viscous forces in shaping motion of the limb. In smaller animals, reduced limb mass diminishes inertial effects, while elastic and viscous forces arising from muscle–tendon units and passive joint structures play a proportionally larger role in determining limb dynamics. Because this thesis focuses on how active and passive forces interact across muscles and joints, insects provide a particularly informative case study. Insect limb dynamics are strongly shaped by viscoelastic muscle–joint mechanics, allowing these interactions to be examined in limb and joint dynamics without being dominated by inertial effects.

2.4 Relevant Insect Anatomy

To understand how viscoelastic muscle-joint mechanics shape limb dynamics in insects, it is first necessary to consider the structural organisation of insect limbs and joints. Insects are hexapod invertebrates, possessing six legs that are each composed of a series of rigid exoskeletal segments connected by compliant joints. From proximal to distal, these segments are coxa, trochanter, femur, tibia, and tarsus [21, 29]. Adjacent segments are connected by joints that permit relative motion between segments, forming an articulated leg. The joint connecting the thorax and coxa, thorax-coxa, attaches the leg to the body and is generally considered to have three degrees of freedom [24, 75, 107]. In contrast, the more distal joints, coxa-trochanter, trochanter-femur, femur-tibia, and tibia-tarsus, are considered to have a single degree of freedom [107]. The tarsus itself is composed of five tarsal segments whose motion is passively actuated. Fig. 2.2 shows the typical anatomical organisation of an insect leg and its respective joints.

At the joint level, insect leg articulation is achieved through specialised regions of the exoskeleton that combine rigidity, localised compliance, and muscle actuation. Function-

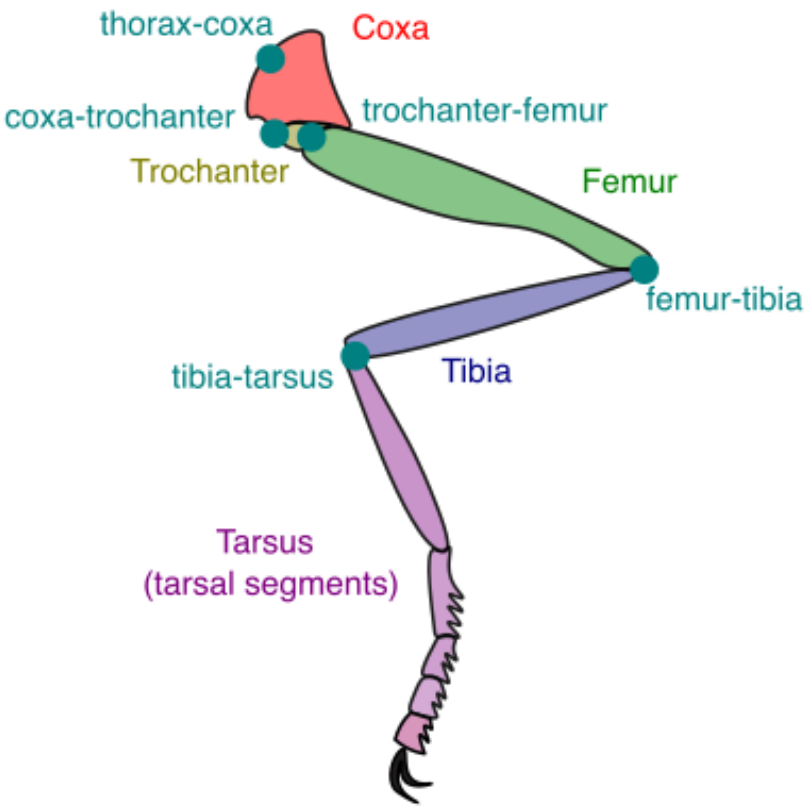

Figure 2.2: Schematic of an insect leg showing the main exoskeletal segments and joint degrees of freedom.

ally, these joints connect adjacent segments, enable controlled intersegmental motion, and maintain stability and precision during movement. The organisation of insect limbs follows a sequential articulation principle, where each joint constrains and guides the motion of the distal segment [92]. Commonly, each joint is actuated with at least two muscles arranged antagonistically [70], although some joints are driven by multiple muscles acting together [73]. These muscles transmit forces via cuticular structures known as apodemes, which serve as attachment and force-transmission elements [40]. In addition to active muscle actuation, insect joints incorporate cuticle, resilin-rich membranes, and surrounding connective tissues that endow them with inherent elastic and viscous properties. These anatomical features define the structural basis of insect joint function and provide the substrate upon which limb mechanics emerge.

The anatomical organisation of insect muscles and joints provides a natural basis for simplified mechanical modelling. The combination of rigid exoskeletal segments, defined joint axes, muscle force generation and transmission, and intrinsic viscoelasticity within joints can be approximated as low-degree-of-freedom mechanical systems with identifiable

active and passive components. Accordingly, a range of muscle and joint models have been proposed that abstract insect muscles as force-generating elements spanning individual joints, and joints as mechanical elements with passive elastic and viscous properties. In the following section, these modelling approaches are overviewed to clarify how muscle actuation and joint mechanics have been represented in insect systems.

2.5 Biomechanical Models of Insect Muscles and Joints

Insects have served as a modelling systems for more than fifty years across studies aimed at understanding the generation and control of locomotion. Pioneering work dates back to computational models established by Holke Cruse [25, 100] in the late 90s. Cruse *et al.* developed the neural network Walknet, a decentralised controller built from experimentally motivated inter-leg coordination rules and local joint control structures from stick insects [24]. The main achievement of Walknet was to demonstrate that stable and adaptive insect walking can emerge from local interactions between leg controllers. Leg coordination did arise from sensory driven modulation of swing-stance transitions and inter-leg influences.

Following generations of this modelling line progressively extended the original Walknet framework to address broader range of behaviours and coordination mechanisms. Later computational implementations introduced additional hierarchical structure for action selection and behavioural switching, as well as body representations used to coordinate multi-joint leg motion in a coherent manner [101]. These developments enabled the decentralised control architecture to generate and stabilise different locomotor modes and to coordinate multiple joints within and across legs, going beyond the primarily local swing–stance decisions of earlier implementations.

Another implementation of Walknet was presented by Thor *et al.* [108], who extended the original decentralised control architecture by coupling it to a refined kinematic representation of insect body and legs. Using anatomically informed multi-joint models based on the dung beetle, their study investigated how leg geometry, joint coordination, and body morphology influence locomotor performance. By integrating distributed, sensory-driven control with a more realistic kinematic description of limb structure, Thor *et al.* demonstrated that stable and adaptable walking behaviour can be achieved across different body configurations without altering the underlying control principles. They showed that multiple behaviours could be generated by the same mechanical system. This work highlighted that a common body morphology, when coupled with different local control architectures, can support distinct behaviours.

However, these models primarily emphasised neural control architectures and sensory

feedback mechanisms underlying motion. They were evaluated using purely kinematic body simulations, in which controller outputs were applied as imposed joint motions rather than arising from force-based actuation, and leg mechanics were not explicitly modelled. While such sensory-driven control strategies can reproduce stable locomotion, they are most applicable to relatively slow-moving organisms, for which sensory feedback can be integrated on appropriate timescales [25]. In faster-moving organisms, by contrast, the intrinsic mechanics and dynamics of the musculoskeletal system play a more prominent role in shaping movement, as reliance on temporally delayed sensory feedback alone becomes insufficient [7, 8, 41, 43, 65].

Motivated by these limitations, a complementary class of models has sought to account explicitly for the mechanical properties of insect muscles and joints. Instead of prescribing motion or relying solely on joint control signals, these models represent muscles as force-generating elements and joints as mechanical systems with intrinsic stiffness and damping. In many models, joints are treated as idealised mechanical constraints, with joint torques emerging from muscle forces and limb geometry, while passive compliance is incorporated primarily through muscle dynamics.

Early efforts to incorporate muscle-level mechanical realism into computational models include the work of Ekeberg *et al.* [36]. Their study aimed to investigate insect walking as an emergent outcome of the interaction between neural control and musculoskeletal dynamics. To this end, Ekeberg *et al.* developed a forward-dynamics model of stick-insect locomotion in which each leg is represented as a system of rigid segments connected by hinge joints, and muscles are formulated as force-generating elements whose output depends on neural activation, muscle length, and contraction velocity. Joint motion emerges from the interaction between muscle forces, limb geometry, and rigid-body dynamics, with system compliance attributed to the muscle models.

Other studies have focused more specifically on how muscle architecture and intrinsic muscle mechanics shape joint behaviour in insect limbs. Full and Ahn [40] developed a 3D musculoskeletal model of the cockroach hind leg with the goal of linking experimentally measured muscle anatomy and attachment geometry to force transmission across joints during locomotion. By explicitly incorporating muscle attachment points and apodeme geometry, their study quantified how moment arms, mechanical advantage, and posture-dependent force transmission influence joint loading and limb function. Extending this line of work toward dynamic analysis, Ghigliazza and Holmes [46] investigated how muscle activation dynamics and intrinsic muscle properties contribute to insect leg dynamics and stability. They introduced a Hill-type muscle model to systematically explore how active force– length and velocity relationships, together with passive muscle elasticity, shape joint torques during rhythmic motion.

Another study that explicitly models viscoelastic Hill-type muscles is presented in [106]. Szczecinski *et al.* developed a neuromechanical model of mantis posture control with the specific goal of shaping joint impedance through parametrised muscle–joint mechanics. In this framework, muscles are represented using a Hill-type actuator formulation, and joint viscoelasticity is implemented through the combined effects of muscle elasticity and damping rather than through prescribed kinematics. Each joint is equipped with a neural mapping that relates muscle length to joint rotation, enabling feedback regulation of posture. Mechanical parameters are determined by estimating the stiffness of the series elastic element associated with the apodeme, defining the parallel elastic stiffness as a fixed proportion of this value, and selecting muscle damping coefficients according to expected joint speeds and torques. The resulting joint dynamics are evaluated in terms of their frequency response and stability to ensure that the closed-loop system operates over behaviourally relevant timescales.

In contrast to [106], the series of models by Tóth *et al.* adopts explicit forward dynamics to connect local neural circuitry to joint motion. The central goal of these studies was to explain how rhythmic activity and sensory-triggered switching give rise to specific behaviours. Early studies focused on forward and backward stepping [109, 111], while later work addressed the modulation and recovery of search movements following perturbations [110]. Mechanically, joints are represented as rigid hinges with inertia, and muscles provide the dominant source of viscoelasticity. Antagonistic Hill-like muscle pairs generate elastic forces through length-dependent stiffness terms together with a linear viscous term proportional to joint angular velocity [109, 111]. A key modelling decision in this framework is that motor neurone activity directly modulates these stiffness terms. In their later work on search movements, this same formulation is extended to incorporate fast and slow muscle fibres as well as muscle recruitment, enabling the authors to test hypotheses about how changes in recruitment and intrinsic muscle stiffness contribute to the observed recovery dynamics after perturbations [110].

These studies, together with many others not reviewed here, have advanced our understanding of insect locomotion by demonstrating how muscle-level mechanical properties influence joint behaviour. Importantly, the level of abstraction adopted in each each model reflects the specific hypothesis being tested. Thus, models range from more detailed anatomical reconstruction to reduced-order formulations designed to isolate particular dynamical effects. Nonetheless, modelling muscle mechanics alone does not fully specify the mechanical environment in which insect joints operate. As discussed before, insect joints have intrinsic passive properties that can strongly shape joint motion. Incorporating such properties into joint models is therefore essential to capture their contribution to movement. For this reason, more recent studies have represented passive joint mechanics explicitly, enabling more direct investigation of how active muscle forces interact with joint elasticity and damping

to produce limb dynamics.

Zaktonik *et al.* [127] examined the mechanical properties of the muscle-joint system in a locust femur-tibia joint during aimed limb movements under changes in load. Their joint model used antagonistic viscoelastic muscles with additional passive viscous damping at the joint. By systematically comparing model variants with and without active force–length/velocity properties, passive muscle elasticity, and joint damping, they showed that passive elastic and viscous properties of the muscle–joint system are both necessary and sufficient for robust load compensation. Passive elastic forces are comparable in magnitude to active muscle forces and can dominate joint mechanics, effectively endowing the joint with substantial stiffness. The combined action of antagonistic passive elastic elements yields an approximately linear damped spring over the functional range, allowing accurate movements across loads with minimal changes in neural drive and highlighting the primacy of intrinsic joint mechanics over complex neural control.

A more recent model with explicit passive properties included in the joint is presented in Naris *et al.* [85]. This model explain how intrinsic muscle and joint mechanics shape control at a single insect leg joint, with particular emphasis on the role of the common inhibitory motor neurone [125]. The joint is modelled with antagonistic Hill-type actuators, including joint inertia, passive elastic restoring torque, and viscous damping. With their model, Naris *et al.* showed that the passive elastic and viscous elements of the femur–tibia joint impose a strong restoring torque toward a preferred rest angle and resist motion through damping and sustained muscle activation is required to counteract the passive elasticity. As a result, the joint–muscle system behaves like a temporal integrator, where muscle force must accumulate over time to overcome passive stiffness and maintain posture. This property is essential for stable, load-resistant positioning, but it also introduces a slow relaxation when the desired joint state changes. The passive joint elasticity therefore creates the need for a control inhibition mechanism that can rapidly remove stored muscle tension to allow the passive joint elasticity to dominate, driving the joint toward a new equilibrium.

In whole-body models, the explicit inclusion of passive properties of the joint has also been explored. In [98], Rubeo *et al.* presented a full-body cockroach that can walk with realistic dynamics. Each of the model legs is actuated by an antagonistic pair of Hill-type, viscoelastic muscles and the joints include a damped spring that contribute to passive restoring torques and resist rapid motion. This means that muscle activation must continuously counteract intrinsic stiffness. As a result, joint motion emerges from the interaction between neural drive and intrinsic mechanics, not from neural commands alone. The authors showed that these passive properties dominate joint behaviour over large portions of the gait cycle, contributing significantly to stability and robustness but also complicating control, since muscles must work against substantial elastic resistance. This motivates their

design approach; rather than minimising passive stiffness, the controller is tuned to exploit it, coordinating antagonistic muscle activity to shape joint impedance appropriately across stance and swing.

A whole-body model of the fruit fly was developed by Vaxenburg *et al.* [116]. In this anatomically detailed physics-based model, joint are implemented with passive viscoelastic properties, modelled as rotational spring-damper systems, to ensure stable and realistic rigid-body dynamics. However, the main goal of this model is to build a flexible simulation platform suitable for learning-based control rather than a biologically faithful representation of insect musculoskeletal mechanics. Consequently, passive joint properties are not treated as central determinants of behaviour, and stability and movement are achieved largely through active control and actuator tuning. Nonetheless, the explicit physics-based formulation provides a valuable platform in which passive viscoelasticity can be measured and manipulated, enabling future investigations into the role of passive mechanical properties within a whole-body context.

The studies reviewed here demonstrate that passive mechanical properties of insect muscles and joints are increasingly recognised as essential contributions to locomotor stability [66, 98, 109, 111], robustness to perturbations [85, 127], and load compensation [106, 127]. From reduced single joint models, to full-body neuromechanical simulations, passive elasticity and damping are shown to shape joint dynamics, impose equilibrium configurations, and in some cases dominate joint behaviour over large portions of movement. These findings challenge a control-centred view of insect locomotion and emphasise the fundamental role of intrinsic joint mechanics.

However, despite this growing recognition of the importance of passive mechanics, most models still do not examine, in a clear and systematic way, how variations in passive joint properties interact with active muscle dynamics to shape joint behaviour across different task and conditions. Passive properties are either subsumed into muscle formulations, introduced as stabilising elements, or tuned to support a particular behaviour, rather than interrogated as functional design components. Because of this, their role in concert with active muscle dynamics remains only partially characterised. Specifically, in terms of how they jointly shape joint impedance, temporal response, and control demands across behaviours and operating regimes.

We address this gap by investigating active muscle dynamics and passive joint mechanics and systematically analysing their interaction within a neuromechanical framework, which will be presented in the chapters that follow.

Chapter 3

Joint Model: Overview

3.1 Overview

Joint dynamics play a key role in the generation and control of movement. Joints act as mechanical interfaces where muscle actuation, passive tissue properties, and skeletal geometry converge to produce movement. Even in relatively small and apparently simple limbs, the way torque is generated at the joint is complex. Active muscle forces interact with passive elastic and viscous elements, and the geometry of the limb affects mechanical advantage and leverage. Understanding how these factors combine to produce controlled movement remains a challenging task.

One way to deal with this challenge is through experimental measurement, which provides important information. However, they are never perfect; measurements of muscle properties, joint stiffness, and activation patterns are often limited by technical constraints, biological variability, and difficulties in isolating individual contributions. As a result, it is not always clear which mechanisms are essential for producing a particular movement and which are secondary or redundant.

Computational models offer a complementary and powerful strategy. They provide a structured framework in which hypotheses about the role of muscles, joints, and passive properties can be formalised and tested. By developing a model, it is possible to focus on the key components that are likely to govern joint behaviour while ignoring details that are either unknown or less important for the purpose of the analysis. At the same time, the process of building a model also acts as a reality check, as it tests whether assumptions that seem reasonable on their own still hold when combined in a functioning system [34]. Models can also make predictions that guide experiments, reveal unexpected interactions, and show how different factors contribute to torque generation. In this way, a model is not

just a tool for reproducing observed behaviour but also a hypothesis about the mechanisms behind it [42, 115].

The aim of this chapter is to present a hierarchy of computational joint models that gradually increases in complexity. This approach seeks to isolate specific mechanisms of joint torque generation while keeping a framework general enough to be applied to a range of joints in both biological and engineered systems. As illustrated in Fig. 3.1, the modelling workflow is grounded in a schematic of a muscle-tendon unit (MTU), which serves as the basic mechanical element underlying all subsequent models. The hierarchy consists of three levels: (i) A single MTU driving a rigid joint, allowing investigation of how active and passive forces from a single muscle contribute to joint torque. (ii) A pair of MTUs acting antagonistically on a passive joint enabling the study of the interactions between antagonistic muscles and intrinsic joint viscoelasticity. And (iii) embedding the level-(ii) joint model in a physics-based simulation environment to allow evaluation of joint dynamics under more realistic mechanical conditions including inertia, gravity, and multi-body interactions. While the hierarchy ends at the physics-based joint for the purposes of this thesis, the framework is designed to scale toward whole-body models, where joint-level principles integrate into coordinated and more complex locomotor systems.

This bottom-up approach has two main advantages. First, it allows us to examine the simplest mechanisms in isolation before adding complexity; thus providing a clear understanding of how each component influences joint behaviour. Second, it ensures that insights obtained at lower levels can be generalised and applied in more complex and realistic settings. By progressively adding antagonistic muscles, passive joint elements, and full-body dynamics, the hierarchy captures increasingly complex interactions while remaining conceptually and computationally manageable.

Although the models are general, they are inspired by insect hinge joints. The goal is to replicate realistic joint behaviour and gain insight into how active muscles and passive joint properties interact. Previous models of insect joints range from phenomenological torque approximations [28, 82, 116] to full musculoskeletal simulations with explicit muscle models and anatomically grounded actuation [78, 109–111, 127], but they rarely explored the interactions between active and passive components or examined the regimes in which each dominates joint dynamics. The models presented here aim to fill this gap, providing a conceptual framework for understanding torque generation in lightweight limbs.

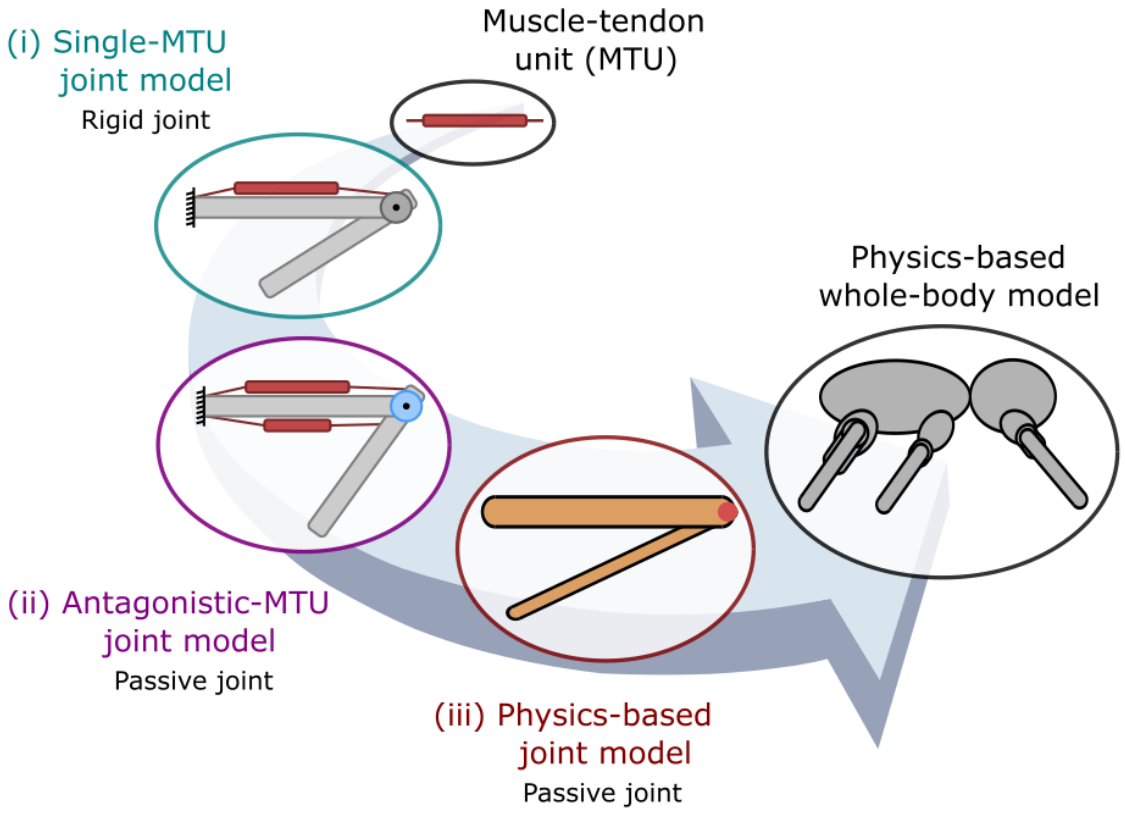

Figure 3.1: A muscle–tendon unit (MTU) forms the starting point of the modelling framework. Progressing along the arrow, the figure illustrates the three hierarchical joint model levels: (i) the single-MTU model, (ii) the antagonistic-MTU model, and (iii) the physics-based joint model. At the head of the arrow, the whole-body model represents the intended direction of the framework, showing how joint-level principles ultimately scale to complete articulated systems.

3.2 General Joint Framework

All three model formulations are built upon a shared biomechanical framework for joint dynamics, inspired by the functional organisation of an insect limb. Fig. 3.2 illustrates a schematic of a biological insect leg, included here to define the elements that will appear in the modelling framework.

In the biological limb, two segments, the femur and the tibia, articulate around a single axis of rotation. Although each segment has its own material properties and internal structure, their deformation is negligible compared to the rotational motion at the joint. For modelling purposes, they can therefore be approximated as rigid bodies. The femur forms the proximal segment, while the tibia is the distal segment that rotates relative to the

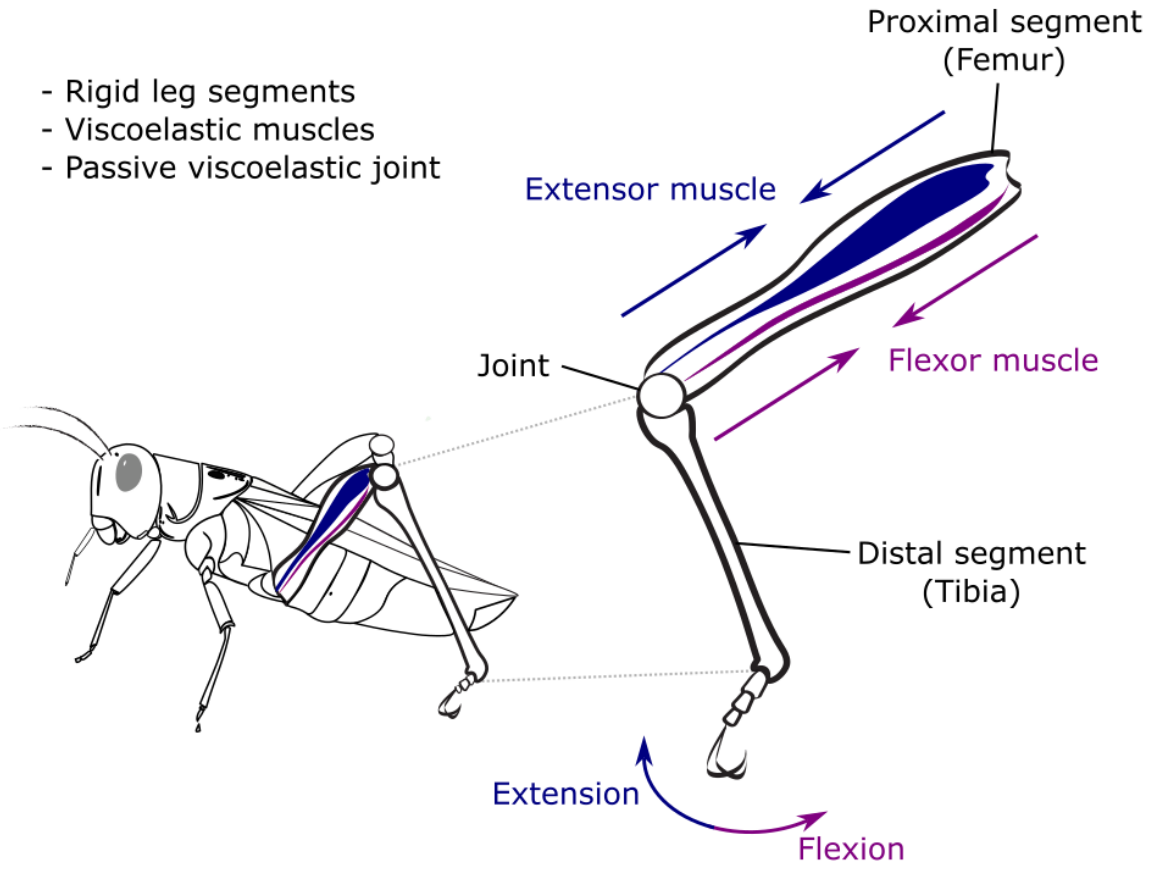

Figure 3.2: Schematic of a biological insect leg. The figure shows a whole-body diagram of an insect with one of the hind leg zoomed for details. Two rigid segments, proximal (femur) and distal (tibia), are connected by a hinge joint with intrinsic viscoelastic properties. The joint is actuated by antagonistic viscoelastic muscles, the extensor and the flexor, which move the tibia. Arrows indicate the direction of muscle contraction and the resulting tibial motion: flexor contraction draws the tibia toward the femur, whereas extensor contraction moves the tibia away from the femur.

femur. Their lengths and geometry define the mechanical leverage available at the joint, since moment arms depend on the relative orientation of the two segments. In the modelling framework, these segments are reduced to ideal rigid links with fixed lengths and uniform mass properties.

A hinge joint connects the femur and the tibia, which defines a single axis of rotation for the distal link. In the biological limb, this joint allows the tibia to swing relative to the femur, enabling flexion and extension movements. Although real insect joints are mechanically complex, with multiple sources of compliance and resistance, the key feature of our modelling framework is that the joint acts as a rotational pivot. In the model, the hinge joint is represented as an ideal revolute joint with a single rotational degree of freedom (DoF).

Joint motion in biological joints is primarily driven by muscles, which generate forces that produce joint torque. In most insect limbs, antagonistic muscle pairs are arranged to enable opposing movements. As shown in Fig. 3.2, the flexor muscle decreases the angle between the tibia and femur, whereas the extensor increases it. Each muscle exhibits active contractile properties, generating force in response to neural activation. Moreover, muscle mechanical properties are activity-dependent: as activation rises, muscles stiffen and produce greater force, while their damping characteristics vary with contraction velocity. These forces are transmitted via tendons (or apodemes in insects), which act as compliant links between muscles and bones (or the exoskeleton in insects) and influence the effective leverage at the joint.

In the modelling framework, we retain these essential features while simplifying the anatomy and mechanics. Muscle and tendons are represented as linear actuators with parallel spring-damper elements. The active spring and damper capture the activity-dependent stiffness and viscosity of the muscle, respectively. Muscle forces are applied to the distal link of the joint through fixed attachment points, while the effective moment arm varies with the joint angle; thus preserving the mechanical leverage throughout the range of motion. This abstraction of the muscle-tendon unit allowed capture of the core role of muscles and tendons in generating torque.

Biological joints also exhibit intrinsic passive properties that resist motion and help restore the joint to its resting configuration. These properties arise from both muscles and the joint itself. Muscles contribute passively to resistance and force transmission even in the absence of activation, while the joint provides intrinsic viscoelasticity through ligaments, cuticle, and surrounding tissues. In the modelling framework, these passive contributions are represented using spring-damper elements. The exact partitioning of passive properties, whether within the muscle or the joint, depends on the specific level of hierarchy.

The proximal (femur) and distal (tibia) links, the hinge joint connecting them, the muscle-tendon units, and the passive elements form the core elements of the joint model. These components provide the structural and functional basis upon which all modelling levels of hierarchy are built.

3.3 Single-MTU Joint Model

The single-MTU joint model is designed to isolate the contribution of an individual muscle–tendon unit (MTU) to joint torque generation. In biological joints, torque normally arises from the coordinated action of antagonistic muscle pairs. Clearly, reducing this system to a single actuator appears contradictory. However, in this model, we assume that the

antagonistic muscles are mechanically equal and operate in a strictly anti-phase manner, such that when one muscle is active or being activated, the opposing muscle is inactive or relaxing, and offers only passive resistance. Under this assumption, the combined effect of the pair can be approximated by a single effective MTU. This representation corresponds to an abstracted rhythmic regime in which the muscles alternate roles without co-contraction and contribute equal and opposite mechanical effects. The aim here is to explore a simplified scenario that reveals the essential interactions between active force production, passive mechanical resistance, and joint motion.

In this model, the joint is actuated by the extensor muscle. The joint itself is represented as a rigid hinge with high stiffness and low damping, meaning it does not include any intrinsic passive elements. As a result, all viscoelastic passive behaviour that would normally arise from both muscles and the joint tissues is incorporated into the MTU. The MTU therefore provides both the active contractile force and the passive resistance needed to stabilise the joint and restore it toward its equilibrium position. To capture these behaviours, the MTU is modelled as a dual spring–damper system arranged in parallel, with one spring–damper pair representing the active element and the other representing the passive element. This formulation allows us to test whether active extension combined with passive recoil can generate coherent joint motion and to establish a mechanical baseline before introducing additional biological detail in subsequent models.

While the single-MTU model provides a minimal baseline and reveals how active and passive forces alone can shape joint motion, it cannot capture behaviours that rely on the interaction between two antagonistic muscles. For this reason, the next level of the hierarchy introduces an explicit pair of MTUs acting on a passive joint.

3.4 Antagonistic-MTU Joint Model

In most limbs, including insect joints, joint motion emerges not from an isolated actuator but from the coordinated interaction of opposing muscles that alternate between producing force, yielding under load, or resisting motion through their passive properties. Additionally, a pair of antagonistic muscles also help to regulate joint stiffness, modulate impedance, and stabilise the limb during dynamic tasks. Naturally, introducing a flexor-extensor pair therefore represents the next step in increasing the biological fidelity of the model.

This model introduces two main adjustments compared with the single-MTU joint model. First, it establishes the common biological configuration of antagonistic actuation by explicitly including both flexor and extensor MTUs. Second, it relocates the viscoelastic passive properties from the MTUs into the joint itself. This arrangement allows us to define

dynamic regimes in which the passive characteristics of the joint play a dominant or modulatory role in shaping overall joint behaviour, providing a more realistic representation of how active and passive forces interact.

Additionally, the inclusion of a pair of antagonistic muscles enables the investigation of mechanical asymmetry between muscles. In most biological systems, antagonistic muscles are not identical; one muscle may be larger, stiffer, or capable of producing greater force than its antagonist. Such differences can influence the distribution of torque across the joint and modulate limb control in task-specific conditions. Incorporating this asymmetry allows the model to explore how different muscle properties contribute to joint behaviour.

In this antagonistic-MTU joint model, both flexor and extensor MTUs are represented as active elements (linear spring–damper systems), tethered to the joint via fixed attachment points. Passive joint viscoelasticity is captured through a rotational spring–damper system, which models the resistance provided by the joint tissues and allows the tibia to return toward its resting configuration when not driven by muscle forces. This separation of active and passive contributions enables the muscles to generate torque without embedding passive resistance within the MTUs. MTU forces remain activity-dependent, produced in response to anti-phase activation patterns. Each muscle applies force through its attachment point, producing torque based on the instantaneous joint angle and the mechanical leverage of its moment arm, which varies with joint orientation.

This model therefore captures three hallmarks of biological joints: (i) pairs of antagonistic and asymmetric actuators; which are modelled as (ii) compliant muscle-like elements that control (iii) passive viscoelastic joints. The goal of this model is to identify dynamical regimes in which active and passive elements shape joint motion and to explore the effects of actuation asymmetry on torque production and overall joint behaviour. It extends the single-MTU baseline, and in the next section, we further increase complexity by embedding the joint model into a fully physics-based simulation environment to investigate joint dynamics under realistic mechanical conditions.

3.5 Physics-Based Joint Model

The physics-based joint model represents the third and final level of hierarchy, where the MTUs are embedded into MuJoCo, a physics engine well-suited to neuromechanical simulation of articulated bodies [83]. Although the previous models accounted for inertia and gravity in the equations of motion (see Sections 4.3 and 4.4), they remained abstracted and simplified, with limited representation surrounding mechanical interactions. Embedding the MTUs and the joint into a physics engine enables the evaluation of joint behaviour under

mechanically realistic conditions.

In this model, leg segments are represented using MuJoCo's primitive *geom* elements which approximate the morphology of the femur and tibia as simple cylinders. Each segment is assigned a fixed mass and MuJoCo automatically computes the corresponding moments of inertia, assuming uniform density. The global coordinate frame is defined such that the femur is fixed while the tibia rotates relative to it around the hinge axis. The joint is implemented as a revolute joint with a single DoF which allows the distal segment to pivot around the proximal segment. The passive viscoelastic properties of the joint are incorporated directly within the MuJoCo environment through rotational stiffness and damping parameters. The joint is actuated using a MuJoCo torque actuator, which is fed with torques produced by the MTUs according to its activation profile and the current state of the joint. In this way, the simulation captures the interaction between active MTU forces, passive joint resistance, and the mechanical behaviour of the tibia.

This model allows us to test whether the principles derived from the single and antagonistic MTU joint models, such as the roles of active and passive contributions in shaping joint motion, remain valid in a physically grounded simulation that includes inertial effects, gravitational forces, and ground reaction forces rather than isolated joint conditions of the earlier model levels. By embedding muscle-tendon units and passive joint elements in a physics-based environment, the model enables systematic exploration of torque generation, joint dynamics, and limb mechanics under more realistic conditions. In addition, the model is thought to set a baseline as it provides a flexible and general framework for a single joint that can serve as a foundation for more complex models, including multi-joint limbs and whole-body neuromechanical simulations.

Together, the three levels of the hierarchy; from a single effective actuator to antagonistic MTUs, to a physics-based joint, provide a progressive framework for dissecting the mechanisms of torque generation and joint behaviour. The physics-based model closes this hierarchy by situating the joint within a realistic mechanical setting, completing the transition from abstract formulations to embodied simulation.

3.6 Model Assumptions

The construction of a biomechanical framework for joint dynamics requires certain simplifications that are not only inevitable but necessary. Rather than attempting to mirror the anatomical and physiological complexity of biological muscle-tendon-joint systems, our framework adopts abstractions that emphasise mechanical clarity, interpretability, and modularity. The key assumptions concern active muscle behaviour, passive mechanical

properties, activation dynamics, and the geometry governing the force transmission. These assumptions are applied across all three models presented in this chapter.

Active dynamics The active MTU element is modelled as a spring in parallel with a damper, where stiffness, spring length, and damping coefficient vary linearly with muscle activation level. This provides a linear approximation of the force-length and force-velocity relationships observed in biological muscle [59, 96], as shown in Fig. 3.3. The spring represents the active force-length component (Fig. 3.3A). At zero activation the spring has no stiffness and the MTU produces no force. As activation increases, stiffness rises linearly to a maximum value, and the MTU length shortens from its default value towards a minimum length. The active element therefore behaves as an activation-dependent restoring spring, generating force that decreases linearly with the shortening of the MTU. This linear dependence is a simplification of the nonlinear bell-shaped force-length relationship of biological muscle (see Fig. 3.3A, left), adopted to maintain computational modularity. So instead of reproducing the bell curve, the model approximates the relationship locally over the ascending segment of the force-length curve (see Fig. 3.3A, right). The shaded region in Fig. 3.3A marks this region over which the linear approximation is applied.

Similarly, the damping element provides a linear approximation of the force-velocity relationship. In biological muscles this relationships is asymmetric, with higher forces produced during eccentric (lengthening) contractions and lower forces during concentric (shortening) ones. This relationship is represented in the left column of Fig. 3.3B. Here, force is proportional to contraction velocity and scaled by activation (see Fig. 3.3B, right). Because this force acts in either direction, the damping behaves as a viscous resistance that opposes the direction of motion, growing in magnitude with the speed of contraction and equally so for shortening and lengthening. This linear damping captures the dependence of muscle force on contraction velocity while omitting the eccentric-concentric asymmetry of the Hill relationship.

Adopting a linear formulation for the active MTU has important implications for how model behaviour is interpreted. By representing force–length and force–velocity relationships as linear elastic and viscous elements scaled by activation, the model provides a local approximation of muscle mechanics around the operating regimes typical of the femur-tibia joint in the model. Muscles operate predominantly on the ascending region of the force-length curve (see shaded band in Fig. 3.3A) and across a moderate range of contraction velocities, regimes in which linear spring and damper elements provide adequate local approximations of the Hill relationships rather than a global description of muscle behaviour. In contrast to nonlinear Hill-type formulations, which capture asymmetric and state-dependent force production, the MTU model emphasises interpretability and causal

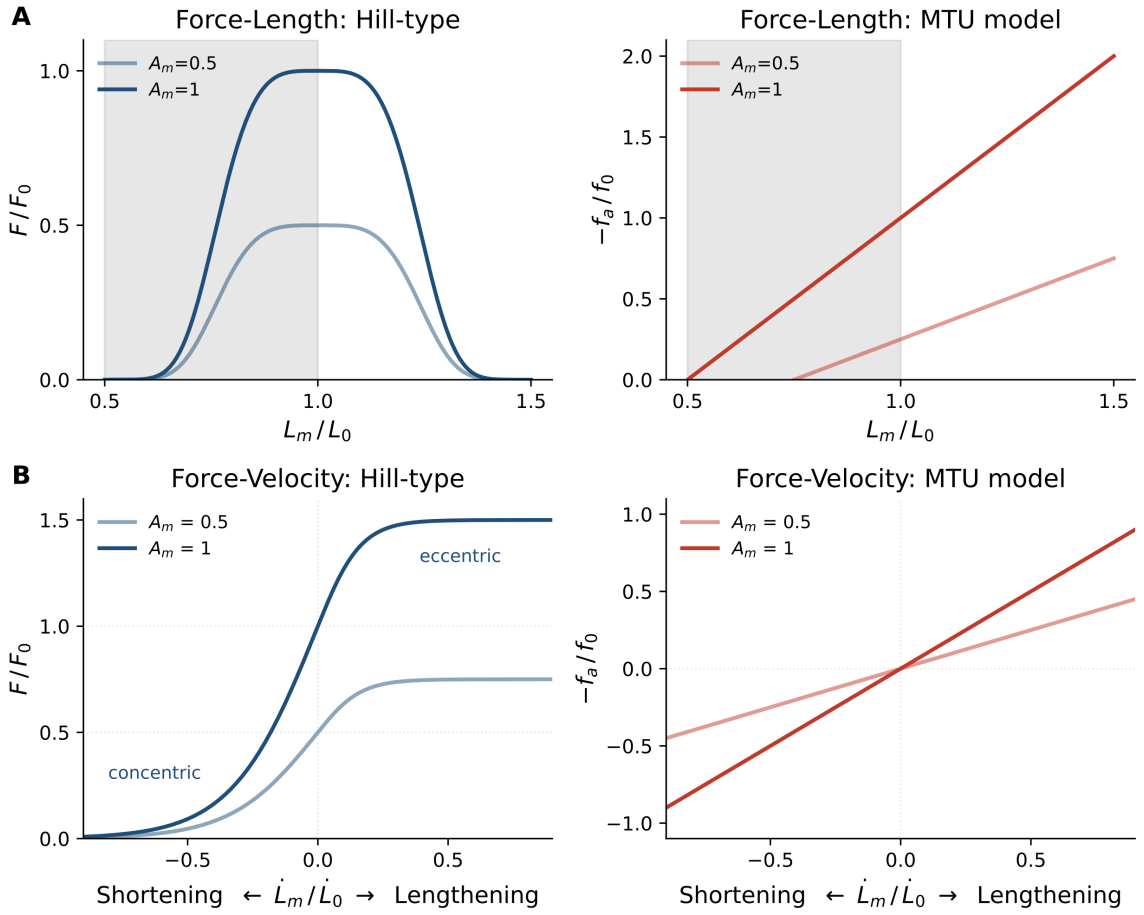

Figure 3.3: Comparison of the Hill-type force–length and force–velocity relationships (left column) with the corresponding relationships of the active muscle-tendon unit (MTU) model used in this thesis (right column), shown at activation levels $Am = 0.5$ and $A_m = 1$. (A) Force–length. Left: representation of the Hill-type relationship, characterised by a plateau of maximal force near the optimal length and declining force to either side. Right: the MTU model approximates Hill relationship with a linear spring, whose stiffness and length are both modulated by activation. The shaded band indicates the region in which the MTU model approximates Hill's relationship, demonstrating that muscle force decreases as the muscle shortens. (B) Force–velocity. Left: the asymmetric Hill-type relationship, with lengthening (eccentric) contractions producing higher forces than shortening (concentric) ones. Right: the MTU model approximates the force-velocity dependence with a linear damping term that is symmetric about the isometric point. In both model panels the force is shown as $-f_a \,/\, f_0$ since contractile forces are defined as negative in the model. Forces are normalised by the peak isometric forces F_0 and f_0, lengths by the optimal length L_0, and velocities by $\dot{L}_0$.

transparency, at the cost of omitting saturation, eccentric force enhancement, and other nonlinear physiological effects that lie beyond its intended scope.

Passive dynamics Muscles and joints contribute passive forces that resist deformation. In biological systems, passive tension arises from connective tissues, titin filaments, tendon elasticity, and the mechanical properties of joint capsules and surrounding cuticle. These structures exhibit nonlinear force–length relationships, with minimal tension near the resting length and rapidly increasing resistance when stretched. In our framework, these diverse contributions are reduced to linear viscoelastic behaviour. Passive forces increase proportionally with extension and velocity, providing a restorative tendency that helps stabilise the joint. Tendon compliance is not represented explicitly as a separate series element. Instead, we assume that when the tendon is sufficiently short or stiff relative to the muscle fibre, the muscle-tendon unit can be treated as a single element without significant loss of dynamic fidelity [126], tendon stiffness is here merged into the active spring constant κ_a. It should be noted, however, that this merging conflates two physically distinct stiffness contributions. Tendon stiffness is independent of activation and engages only after the tendon has been stretched beyond its slack length, whereas the active spring stiffness κ_a in this model scales directly with activation. The length-dependent engagement of the tendon is therefore not captured. This is a recognised simplification that omits the series elastic energy storage associated with tendon compliance.

Muscle activation dynamics When neural activity is explicitly modelled, activation is generated from discrete motor neurone spikes through a low-pass filtering process, approximating the combined effects of calcium dynamics, cross-bridge recruitment, and other intracellular processes. In other parts of the thesis, activation is prescribed directly as a time-varying signal, such as square or sinusoidal signals, to explore joint responses independently of neural control. In this way, we assume a single, lumped activation pathway, linear summation of inputs, and saturating activation, while neglecting motor neurone recruitment order and detailed sarcomere-level mechanisms.

Muscle and joint geometry The lengths of the flexor and extensor MTUs and their corresponding moment arms are represented as continuous functions of the joint angle. While real musculoskeletal geometry involves curved muscle paths, compliant tendons, and spatially distributed attachment points, this simplified representation is a practical approximation that preserves the essential relationship between joint rotation and the mechanical advantage of the muscles [113]. We adopt this assumption to maintain a clear and predictable mapping between joint kinematics and the mechanical effects of muscle contraction. By allowing moment arms to vary systematically with joint angle, the model preserves the key feature that torque generation depends on both muscle length and leverage, without requiring detailed anatomical reconstruction. This approach enables the study of fundamental principles of force production and the interaction between active and passive elements,

while keeping the geometry simple enough to isolate and interpret the contributions of each component.

Across the three modelling levels, we observe a consistent theme: joint behaviour emerges not from any single component, but from the interaction between active force production, passive mechanics, and limb geometry. What changes across the hierarchy is which factors become the main determinants of motion. In the single-MTU model, the MTU's properties dominate. With two MTUs, the interplay between antagonists and joint stiffness become decisive. In the physics-based model, inertial and environmental forces progressively shape the resulting dynamics.

Chapter 4

Joint Model: Methods

4.1 Overview

The previous chapter presented an overview of the three hierarchical levels of the joint model. Here, we detailed the mathematical methods used to implement each model, moving from the MTU formulation to the full physics-based joint. The goal is to provide the reader with a clear description of how the joint, muscles, activation dynamics, and passive elements are represented at each level, and how these components are combined to produce the results analysed in the remainder of the thesis.

Section 4.2 introduces the mathematical formulation of the muscle-tendon unit, which is the primary source of actuation. This includes the active and passive components, the representation of the muscle-tendon length, and the dependency of force production on activity level, length, and contraction velocity. After establishing this, the formulation of the single-MTU joint model is presented in Section 4.3. We include the assumptions under which two antagonistic muscles can be approximated by a single effective actuator, and the way passive system properties are incorporated into the MTU. Next, Section 4.4 describes the antagonistic-MTU joint model, in which a flexor and extensor act on a joint with explicit passive viscoelasticity. This section also includes the representation of muscle asymmetry.

Having presented the first two models, Section 4.5 then introduces their nondimensional formulation. The aim of this reformulation is not to restate the models, but to reveal the underlying structure that governs their behaviour. By rescaling time, length, and force, the MTU and joint equations are expressed in terms of a set of dimensionless parameters that capture the balance between the active and the passive elements of the system. This provides the conceptual basis for the parameter sweeps and frequency-response analysis performed in following chapters, where variations in these dimensionless ratios are used to

interrogate the mechanical principles underlying joint motion.

Then, Section 4.6 the implementation of the physics-based joint model in MuJoCo [83]. Here, the general mathematical formulation is embedded within a simulated environment that provides rigid-body dynamics, contact interactions, and gravitational loading. We describe how the MuJoCo joint is constructed, and how the MTU models interface with MuJoCo's physics engine to generate joint motion (Section 4.6.1). Building on this foundation, we extend the same formulation to a multi-joint and whole-body configuration presented in Section 4.7, linking several joint units to form limbs and, ultimately, a more complex articulated body. This generalisable structure uses the principles developed for a single joint to scale to a larger biomechanical model to explore coordinated movement, inter-joint coupling, and body-level mechanical interactions.

Finally, Section 4.8 describes the activation model implemented later in Chapter 5.

4.2 The Muscle-Tendon Unit Model

The muscle-tendon unit is represented using separate active and passive mechanical components acting in parallel, each contributing to the total force transmitted to the joint. This model takes inspiration from the work presented by Boyle *et al.* [14], which represent the active muscle and passive body forces with spring-damper systems to model the undulatory locomotion of a slender swimmer.

As discussed in Section 3.2, the active component is modelled by a spring-damper system whose properties depend on the muscle activation signal A_m (see Fig. 4.1). Activation modulates the spring stiffness κ_a, the spring length L_t, and the damping coefficient β_a. These dependencies give a piece-wise linear approximation of the intrinsic force-length and force-velocity relationships described by Hill [59], as showed in Section 3.6. In the joint model, actuation is produced by two MTUs, the flexor and the extensor, each contributing forces accordingly to the same formulation. For each MTU $i = \{\text{fl},\ \text{ext}\}$, the total active contractile force is given by:

$$f_a^{(i)} = \kappa_a^{(i)}(L_t^{(i)} - L_m^{(i)}) - \beta_a^{(i)}\dot{L}_m^{(i)} \tag{4.1}$$

where L_m denotes the spring length, and the dot denotes time differentiation (hence $\dot{L}_m$ is the muscle contraction rate). For the sake of simplicity, we chose the length of the flexor and extensor MTUs to be defined geometrically as $L_m^{\text{fl}} = -L_m^{\text{ext}} = -\cos\theta$, which provides a symmetric mapping between the joint angle and muscle length while reflecting the opposing changes in length of ideal antagonistic muscles [49, 85]. L_t denotes the activation-dependant

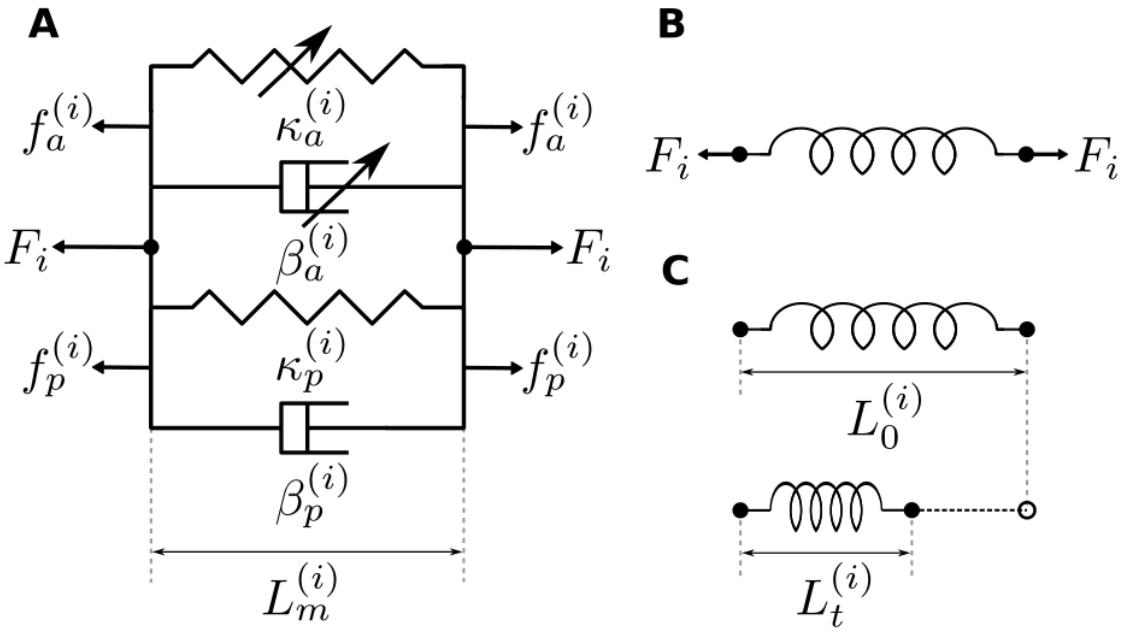

Figure 4.1: The Muscle-Tendon Unit Model (MTU). (A) Schematic representation of the active (contractile) and passive spring-damper systems arranged in parallel, where $\kappa_a^{(i)}$ is the spring constant of the active system, and $\beta_a^{(i)}$ is the damping coefficient of the active system. $f_a^{(i)}$ corresponds to the force produced by the active elements, and $f_p^{(i)}$ is the force produced by the passive elements. Thus, F_i is total force generated by the MTU. $L_m^{(i)}$ is the current muscle-tendon length. (B) Simplified symbol for the comprehensive dual spring-damper MTU model. (C) $L_0^{(i)}$ is the spring's resting length, and $L_t^{(i)}$ represents the activation-dependent spring length. In all panels, $i = \mathrm{fl}, \mathrm{ext}$.

tension length of the spring element, given by:

$$L_t^{(i)} = L_0^{(i)} - \sigma(A_m^{(i)})(L_0^{(i)} - L_{\min}^{(i)}) \,,$$

where L_0 (see Fig. 4.1C) is the spring resting length and $L_{\min}$ is the minimum spring length during full activation. The dynamic stiffness κ_a and damping β_a are defined as:

$$\begin{aligned} \kappa_a^{(i)} &= \kappa_{\max}^{(i)} \sigma(A_m^{(i)}) \,, \\ \beta_a^{(i)} &= \beta_{\max}^{(i)} \sigma(A_m^{(i)}) \,, \end{aligned}$$

where $\kappa_{\max}^{(i)}$, $\beta_{\max}^{(i)}$ and are constants. The piece-wise linear function $\sigma(\cdot)$ clips the muscle

activation signal A_m to the allowable range; it is defined as:

$$\sigma(y) = \begin{cases} 0: & y \leq 0 \\ y: & 0 < y < 1 \\ 1: & y \geq 1\,. \end{cases}$$

The active component is complemented by a passive spring-damper system, which generates force when the MTU is stretched beyond its resting length, thereby restoring the muscle towards its equilibrium configuration. In the absence of muscle activation A_m, the MTU generate passive force according to:

$$f_p^{(i)} = \kappa_p^{(i)}(L_0^{(i)} - L_m^{(i)}) - \beta_p^{(i)}\dot{L}_m^{(i)}\,, \tag{4.2}$$

where κ_p denotes the passive spring constant and β_p is the passive damping coefficient. This way, passive forces provide a restoring force that contributes to the system's intrinsic stability without the need for muscle activation or active force of the opposing muscle.

Given that the active contractile element acts in parallel with the passive components, the total MTU force is:

$$F_i = f_a^{(i)} + f_p^{(i)}\,. \tag{4.3}$$

This model provides a unified representation of muscle mechanics, combining active contractile forces with passive viscoelastic resistance, and serves as the main source of actuation for the joint models.

4.3 The Single-MTU Joint Model

The single-MTU joint model isolates the contribution of an individual MTU to joint torque generation. For the purpose of this model and as discussed in Section 3.3, we assume that both MTUs have the same mechanical properties and operate in anti-phase. Mathematically, the total muscle torque on the joint generated by two antagonistic muscles can be expressed as

$$T_{\text{MTU}} = T_{\text{ext}} - T_{\text{fl}} = F_{\text{ext}}\, r_{\text{ext}} - F_{\text{fl}}\, r_{\text{fl}}\,,$$

where F_{ext} and F_{fl} are the forces of the extensor and flexor, respectively, and r_{ext} and r_{fl} are their corresponding moment arms. Under the assumption of mechanical symmetry ($F_{\text{ext}} = F_{\text{fl}}$, $\kappa_{\text{ext}} = \kappa_{\text{fl}}$, $\beta_{\text{ext}} = \beta_{\text{fl}}$, $r_{\text{ext}} = r_{\text{fl}}$) and strict anti-phase activation, the inactive muscle contributes primarily through its passive properties. The total muscle torque T_{MTU}

simplifies to

$$T_{\text{MTU}} \approx F_{\text{effective}}\, r\,,$$

where $F_{\text{effective}}$ combines the active force of the currently contracting MTU and the passive contribution of the relaxed MTU. Therefore, the two antagonistic muscle-tendon units can be approximated by a single effective MTU producing the same torque profile at the joint while capturing both active and passive contributions.

Following this rationale, this joint model is represented as a rigid hinge joint actuated by the extensor MTU, which represents the net effect of the antagonistic pair of MTUs. The distal link is modelled as a rigid rod of length l and mass m with uniform density, while the proximal link is assumed to be fixed, providing a static anchor for the joint. At rest, the distal link hangs perpendicular to the proximal link, defining a reference joint angle of $\theta_{\text{rest}} = 90°$. The MTU applies force to the distal link in a horizontal direction, from a fixed attachment point relative to the joint's axis of rotation. At θ_{rest}, the moment arm of length r_{ext} is perpendicular to the distal link. As the joint angle θ changes, the moment arms vary in length accordingly: $r_{\text{ext}} = -\sin(\theta)$. This follows the commonly accepted relationship between the muscle length, L_m, and the muscle's moment arm, r, dictated by $r = d\,L_m/d\theta$ [9]. Fig. 4.2 presents a schematic of the single-MTU model.

The net torque on the joint results from the extensor torque $F_{\text{ext}}\, r_{\text{ext}}$, and the weight of the distal link mg acting at its centre of mass $l/2$:

$$T_{\text{net}} = F_{\text{ext}}\, r_{\text{ext}} - \frac{mgl\sin\theta}{2}\,. \tag{4.4}$$

Including the moment of inertia J of the distal link accounts for the distribution of mass along the segment and its resistance to angular acceleration. The moment of inertia determines how much torque is required to achieve angular acceleration. For a uniform rigid rod of length l and mass m rotating about one end, $J = 1/3\, m\, l^2$. This assumption reflects the geometry of the distal link, which rotates about the joint as a pendulum. Using the definition of J, the rotational equation of motion follows:

$$J\ddot{\theta} = T_{\text{net}}\,.$$

Substituting the expression for T_{net} yields the complete equation governing joint motion:

$$\ddot{\theta} = \frac{1}{J}\left[F_{\text{ext}}\, r_{\text{ext}} - \frac{mgl\sin\theta}{2}\right]\,. \tag{4.5}$$

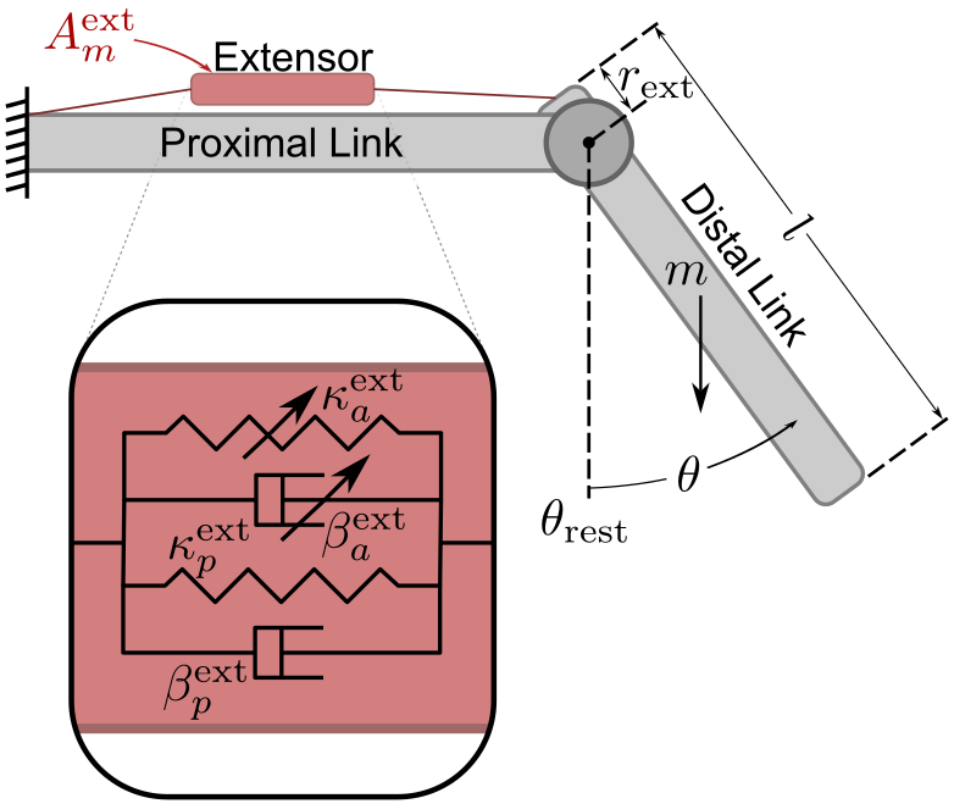

Figure 4.2: Schematic of the single-MTU joint model. At rest, the joint angle θ between the proximal and distal links is $\theta_{\text{rest}} = 90°$. The distal link, with mass m, is connected to the proximal link via a rigid hinge joint, represented by the grey circle. Extensor MTU is positioned on either side of the proximal link, tethered to its free end and the near end of the distal link. This MTU is driven by the activation input signals A_m^{ext}, and modelled using the muscle-tendon unit formulation.

4.4 The Antagonistic-MTU Joint Model

The single-MTU model incorporates the overall passive properties of the system within the extensor MTU. However, experimental evidence indicates that the joint itself has sufficiently strong passive properties to generate motion even without muscle activation. This observation motivates the antagonistic-MTU joint model, which transfers the passive viscoelastic elements from the MTU to the joint structure. The motivation for this modification will be discussed in detail in Chapter 5.

In this model, the joint is now actuated by a pair of antagonistic MTUs, with the extensor and flexor muscles providing opposing torques. With the flexor included, we can capture the coordinated interplay between antagonistic muscles while isolating the joint's

passive contributions. The passive spring and damper elements originally embedded in the MTUs are removed, and the joint itself includes a rotational spring and damper directly to represent its intrinsic passive elastic (κ_j) and viscous (β_j) elements, see Fig. 4.3 for illustrative details. With these elements embedded in the joint, we analyse how the joint's passive mechanics shape overall torque generation and flexion-extension dynamics (see Section 5.3.1 for details).

With the removal of the passive elements from the MTUs, equation 4.3 modifies to:

$$F_i = f_a^{(i)} = \kappa_a^{(i)}(L_t^{(i)} - L_m^{(i)}) - \beta_a^{(i)}\dot{L}_m^{(i)}\,,$$

where the length of the MTU varies as $L_m^{\text{fl}} = -L_m^{\text{ext}} = -\cos\theta$.

Consequently, the total muscle torque is now given by:

$$T_{\text{MTU}} = \sum_{i=\{\text{fl},\,\text{ext}\}} F_i\, r_i\,,$$

where the moment arms of the MTUs are defined as $r_{\text{fl}} = -r_{\text{ext}} = \sin\theta$.

Structurally, the distal and proximal links remain unchanged from the configuration described in Section 4.3. However, the net torque balance now includes contributions from the joint's intrinsic passive properties. The torque generated by the passive joint is given by:

$$T_{\text{pass}} = -(\,\kappa_j\,\Delta\theta + \beta_j\,\dot{\theta}\,)\,,$$

where $\Delta\theta = \theta - \theta_{\text{rest}}$ represents the angular displacement from the joint's rest position. Thus, the net torque on the joint (equation 4.4) becomes:

$$T_{\text{net}} = \sum_{i=\{\text{fl},\,\text{ext}\}} F_i\, r_i - \kappa_j\,\Delta\theta - \beta_j\,\dot{\theta} - \frac{mgl\sin\theta}{2}\,, \tag{4.6}$$

which accounts for the active muscle torques, the passive joint properties, and the gravitational torque acting at the centre of mass of the distal link.

Including the moment of inertia J of the distal link, the rotational equation of motion is derived from Newton's second law of rotation:

$$\ddot{\theta} = \frac{1}{J}\left[\sum_{i=\{\text{fl},\,\text{ext}\}} F_i\, r_i - \kappa_j\,\Delta\theta - \beta_j\,\dot{\theta} - \frac{mgl\sin\theta}{2}\right]. \tag{4.7}$$

This formulation provides an accurate representation of joint dynamics by explicitly modelling the passive mechanical contributions of the joint itself.

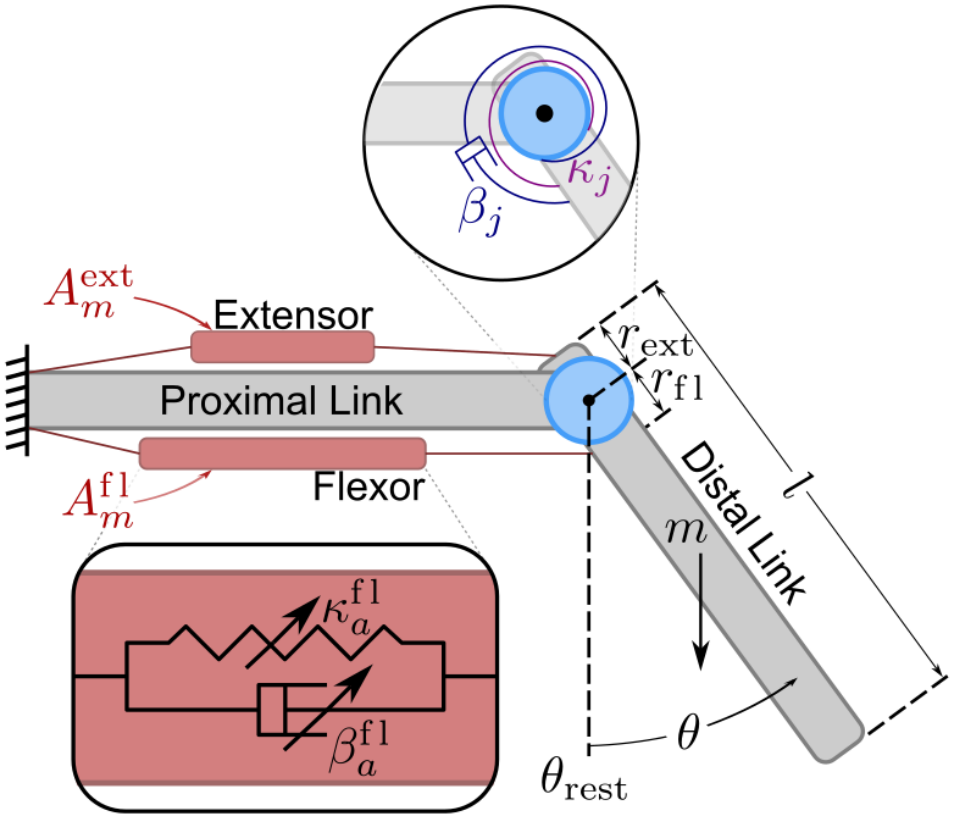

Figure 4.3: Schematic of the antagonistic-MTU joint model. At rest, the joint angle θ between the proximal and distal links is $\theta_{\text{rest}} = 90°$. The distal link, with mass m, connects to the proximal link via a rotational spring and damper with passive stiffness κ_j and damping β_j, represented by the blue circle. Flexor and extensor MTUs are modelled as linear spring-damper systems with variable stiffness κ_a and damping β_a, driven by activation signals A_m^{fl} and A_m^{ext}. The schematic illustrates the flexor MTU model as an example.

While the single-MTU and antagonist-MTU joint models capture the mechanical principles governing joint motion, their parameters (particularly stiffness and damping) are often challenging to determine with precision. Experimental measurements of these properties vary widely across species and are influenced by multiple biological and methodological factors, making direct parameter estimation unreliable. To address this limitation and generalise model behaviour beyond species-specific parameter sets, we derive a nondimensional representation of the MTU and joint models.

4.5 Nondimensionalisation

When developing mathematical models of musculoskeletal dynamics, it is often useful to reformulate the governing equations in a dimensionless form. Nondimensionalisation rescales variables and parameters by introducing characteristic reference quantities, which reduces the number of independent parameters in the system. This process not only simplifies the mathematical analysis but also reveals the essential parameter groupings that govern the behaviour of the model. In the context of muscle and joint dynamics, this provides a systematic way to highlight the relative importance of mechanical properties and timescales, enabling general insights that are not tied to specific choice of measurable units or parameter values.

In this section, we derive a nondimensional form of the equations of motion 4.3 and 4.5 presented in Sections 4.2 and 4.3, respectively. In order to do it, we normalise the muscle length L_m by the characteristic muscle length L_0 to obtain $L_m = L_0\,\hat{L}_m$, and the time t by the characteristic time scale τ to give $t = \tau\,\hat{t}$. Here, $\hat{\cdot}$ denotes a dimensionless variable. For the purposes of our analysis, we choose the characteristic length L_0 to correspond to the resting muscle length, and the characteristic time τ to represent the typical cycle period of the joint oscillation.

4.5.1 The Muscle-Tendon Unit Model

Substituting L_0 and τ into equations 4.1, 4.2, 4.3 produces the dimensionless muscle force equation for both flexor and extensor (i):

$$\hat{f}_a^{(i)} = A_m^{(i)}\left[\eta_a^{(i)}(\hat{L}_t^{(i)} - \hat{L}_m^{(i)}) - \hat{\dot{L}}_m^{(i)}\right], \tag{4.8}$$

$$\hat{f}_p^{(i)} = \eta_p^{(i)}(1 - \hat{L}_m^{(i)}) - \hat{\dot{L}}_m^{(i)}, \tag{4.9}$$

$$\hat{F}_i = \mu_j^{(i)}\hat{f}_a^{(i)} + \hat{f}_p^{(i)}, \tag{4.10}$$

where

$$\eta_a^{(i)} = \frac{\kappa_{\max}^{(i)}}{\beta_{\max}^{(i)}}\,\tau, \quad \eta_p^{(i)} = \frac{\kappa_p^{(i)}}{\beta_p^{(i)}}\,\tau, \quad \mu_j^{(i)} = \frac{\beta_{\max}^{(i)}}{\beta_p^{(i)}}.$$

4.5.2 The Single-MTU Joint Model

Likewise, the substitution of the dimensionless variables L_0 and τ into equation 4.4 results in the dimensionless net torque:

$$\hat{T}_{\text{net}} = \hat{F}_{\text{ext}}\,\hat{r}_{\text{ext}} - \gamma\,(\sin\theta)\,, \tag{4.11}$$

where

$$\hat{r}_{\text{ext}} = \frac{r_{\text{ext}}}{L_0^{\text{ext}}}\,, \quad \gamma = \frac{mgl}{2\,(L_0^{\text{ext}})^2\,\beta_{\max}^{\text{ext}}}\,\tau\,.$$

Including the scaled moment of inertia of the distal rod $\hat{J}\ddot{\theta} = \hat{T}_{\text{net}}$, yields the dimensionless equation of motion:

$$\ddot{\theta} = \frac{1}{\hat{J}}\left[\hat{F}_{\text{ext}}\,\hat{r}_{\text{ext}} - \gamma\,(\sin\theta)\right]\,, \tag{4.12}$$

where the dimensionless moment of inertia is defined as:

$$\hat{J} = \frac{J}{(L_0^{\text{ext}})^2\,\beta_{\max}^{\text{ext}}\,\tau}\,.$$

The nondimensional formulation allows us to define a key set of parameters that encapsulate critical physical properties of the joint system.

The parameters $\eta_a^{(\text{fl},\,\text{ext})}$ and $\eta_p^{(\text{fl},\,\text{ext})}$ denote the ratios of stiffness to damping for the active (contractile) and passive elements of the muscle-tendon units, respectively. They indicate whether each element behaves more like an elastic spring (large η) or a viscous damper (small η). Note that the inverse of these parameters, $\tau_a = 1/\eta_a$ and $\tau_p = 1/\eta_p$, correspond to the intrinsic time constants of the active and passive elements. τ_a characterises how quickly the MTU generates force and restores displacement under activation. On the other hand, τ_p characterises how quickly the MTU relaxes back to its resting length once activation ceases. Thus, η_a and η_p capture the relative speeds of the active and passive muscle dynamics, playing a key role in shaping the overall joint response.

The dimensionless parameter μ_j compares the damping contributions of the active and passive elements of the MTU. Values of $\mu_j > 1$ indicate that viscous resistance is dominated by the contractile element, whereas $\mu_j < 1$ indicates that passive damping dominates. In terms of the total MTU force, μ_j determines how strongly active muscle contraction influences the overall joint torque compared to passive viscoelastic forces. A high μ_j amplifies the contribution of active force generation, while a low μ_j emphasises passive resistance in shaping the net MTU force response.

The dimensionless gravitational torque, γ, is a specific example of a mechanical load. It denotes the ratio between the mechanical load, here the gravitational torque of the distal link, and the passive joint damping. For $\gamma \gg 1$, gravitational forces will have a dominant effect on joint motion regardless of passive damping. For $\gamma \ll 1$, damping resists motion, and gravity has only a minor effect. Biologically, this distinction highlights that in small limbs, where masses are low, gravitational loading may often be negligible compared to viscoelastic forces.

Finally, the dimensionless moment of inertia $\hat{J}$ encapsulates the effect of the distal link's rotational inertia on the joint dynamics. High values of $\hat{J}$ indicates that inertial forces dominate, leading to delayed responses, oscillations, or overshoot in joint motion. In contrast, a low $\hat{J}$ implies that the joint is overdamped, with motion determined primarily by viscoelastic and active MTU forces rather than inertia.

4.5.3 The Antagonistic-MTU Joint Model

The same nondimensionalisation procedure is applied to the antagonistic-MTU joint model. In this case, the the dimensionless muscle force equation for both flexor and extensor (i) is given by

$$\hat{F}_i = \eta_a^{(i)}(\hat{L}_t^{(i)} - \hat{L}_m^{(i)}) - \hat{\dot{L}}_m^{(i)}\,, \tag{4.13}$$

where

$$\eta_a^{(i)} = \frac{\kappa_{\max}^{(i)}}{\beta_{\max}^{(i)}}\,\tau\,.$$

Likewise, the dimensionless net torque on the joint follows as

$$\hat{T}_{\text{net}} = \mu_c\,(\hat{F}_{\text{fl}}\,\hat{r}_{\text{fl}} + \mu_m(\hat{F}_{\text{ext}}\,\hat{r}_{\text{ext}})\,) - \eta_j(\Delta\theta) - \dot{\theta} - \gamma\,(\sin\theta)\,, \tag{4.14}$$

where

$$\mu_c = \frac{\Sigma_{i=\text{fl, ext}}\,\beta_{\max}^{(i)}\,(L_0^{(i)})^2}{\beta_j},$$

$$\mu_m = \frac{\beta_{\max}^{\text{ext}}\,(L_0^{\text{ext}})^2}{\beta_{\max}^{\text{fl}}\,(L_0^{\text{fl}})^2}\,, \quad \eta_j = \frac{\kappa_j}{\beta_j}\,\tau, \quad \gamma = \frac{mgl}{2\beta_j}\,\tau\,.$$

Similarly as in the original joint model, we include the dimensionless moment of inertia to obtain the rotational equation of motion as follows

$$\ddot{\theta} = \frac{1}{\hat{J}}\left[\mu_c\,(\hat{F}_{\text{fl}}\,\hat{r}_{\text{fl}} + \mu_m(\hat{F}_{\text{ext}}\,\hat{r}_{\text{ext}})\,) - \eta_j(\Delta\theta) - \dot{\theta} - \gamma\,(\sin\theta)\right], \tag{4.15}$$

where the dimensionless moment of inertia is defined as:

$$\hat{J} = \frac{J}{\beta_j \tau} .$$

Because the joint angle θ is already dimensionless, we do not include a $\hat{\cdot}$ symbol for its scaled form in the joint models. Note that in this antagonistic-MTU model, η_j represents the ratio between the stiffness and damping of the passive joint, scaled by the time scale τ. This parameter is analogous to the dimensionless parameter $\eta_p^{(i)}$, with the distinction that η_j is normalised by the passive damping of the joint, whereas $\eta_p^{(i)}$ is normalised by the passive damping of the corresponding muscle-tendon unit. Similarly, the parameter μ_c is analogous to $\mu_j^{(i)}$, and the same scaling considerations apply.

In addition, this model introduces the dimensionless asymmetry parameter μ_m, which quantifies the relative torque capacity of the extensor compared to the flexor. In other words, μ_m indicates how much the torque production of the extensor outweighs, or is outweighed by, that of the flexor. In a symmetric case ($\mu_m = 1$), both muscles contribute equally, while asymmetric regimes, $\mu_m > 1$ or $\mu_m < 1$, correspond to a stronger or weaker extensor, respectively.

We summarise all the dimensionless parameters defined for both the MTU-based joint model and its joint-level viscoelastic variant in Table 4.1. The table includes their definitions and corresponding interpretations for clarity and completeness. For those interested in a detailed derivation of the nondimensional muscle-tendon unit and joint models equations of motion, please refer to Section A.1 in Appendix A.

Both the dimensional and nondimensional models were implemented and simulated in `Python` (version 3.11), using `NumPy` for numerical computation. For numerical integration of the governing equations, the explicit Euler method was used with a time step of 0.1 ms, which was verified to produce stable and consistent results across the parameter ranges explored.

To conclude, we have presented the nondimensional equations of motion for the muscle-tendon unit and the joint models. In addition, we have identified key dimensionless parameters that characterise the relative contributions of stiffness, damping, inertia and external loading. These parameters provide compact measures of how active and passive elements interact to shape joint dynamics and allow direct comparison across systems of different scales, from insect limbs to larger biological or robotic joints.

Parameter	Definition	Interpretation
The Single-MTU Joint Model		
η_a^{ext}	$\frac{\kappa_{\max}^{\text{ext}}}{\beta_{\max}^{\text{ext}}}\,\tau$	Active stiffness–to–damping ratio
η_p^{ext}	$\frac{\kappa_p^{\text{ext}}}{\beta_p^{\text{ext}}}\,\tau$	Passive stiffness–to–damping ratio
μ_j^{ext}	$\frac{\beta_{\max}^{\text{ext}}}{\beta_p^{\text{ext}}}$	MTU active–to–passive ratio
γ	$\frac{mgl}{2\,(L_0^{\text{ext}})^2\,\beta_{\max}^{\text{ext}}}\,\tau$	Gravitational–to–viscous forces ratio
$\hat{J}$	$\frac{J}{(L_0^{\text{ext}})^2\,\beta_{\max}^{\text{ext}}\,\tau}$	Dimensionless moment of inertia
The Antagonistic-MTU Joint Model		
$\eta_a^{(i)}$	$\frac{\kappa_{\max}^{(i)}}{\beta_{\max}^{(i)}}\,\tau$	Active (MTU) stiffness–to–damping ratio
η_j	$\frac{\kappa_j}{\beta_j}\,\tau$	Passive (joint) stiffness–to–damping ratio
μ_c	$\frac{\sum_{i=\text{fl, ext}}\beta_{\max}^{(i)}\,(L_0^{(i)})^2}{\beta_j}$	Active–to–passive (MTU–to–joint) ratio
μ_m	$\frac{\beta_{\max}^{\text{ext}}(L_0^{\text{ext}})^2}{\beta_{\max}^{\text{fl}}(L_0^{\text{fl}})^2}$	MTU asymmetry ratio
γ	$\frac{mgl}{2\beta_j}\,\tau$	Gravitational–to–viscous forces ratio
$\hat{J}$	$\frac{J}{\beta_j\,\tau}$	Dimensionless moment of inertia

Table 4.1: Dimensionless parameters derived for the single-MTU and antagonistic-MTU joint models. In the antagonistic-MTU model, $i = \{\text{fl, ext}\}$.

4.6 The Physics-Based Joint Model

In the previous sections, we introduced the equations of motion for the muscle-tendon unit and two joint model formulations used to simulate joint behaviour, together with their nondimensional derivations. While the nondimensional joint model provides a compact and generalisable framework to analyse the relative influence of the different parameters that characterise the system's dynamic behaviour, it remains an abstracted description. Such derivations are useful for theoretical insight and parameter exploration. However, they do not directly capture the full complexity of multi-body dynamics and interaction forces that occur in mechanical systems.

To address this and complement the nondimensional analysis, we introduce a physics-based model of the joint implemented in MuJoCo, a physics engine designed for simulation of musculoskeletal and robotic systems [83]. In this formulation, the torque output generated by the nondimensional MTU model is used as an input to actuate the MuJoCo joint. This hybrid strategy bridges the theory and physics-based simulation, the nondimensional model provides biologically interpretable torque generation, while MuJoCo ensures physically consistent joint motion within a realistic mechanical environment.

With this model, we test whether the principles derived from the single-MTU nondimensional model remain valid when embedded into a full rigid-body dynamics simulation. Additionally, the model enables direct comparison to experimental and robotic setups, where limb inertia, contact dynamics, and gravitational force are unavoidable. The physics-based joint model thus serves as an intermediate step between theory and experimental reality.

4.6.1 Model Configuration in MuJoCo

The MuJoCo physics engine provides a direct way to specify different mechanical properties of the simulated joint, including its stiffness and damping. In this implementation, these properties are defined at the joint level, where MuJoCo expresses viscoelasticity as a rotational spring-damper system [84]. This setup parallels the structure introduced in the antagonistic-MTU model, where passive behaviour is assigned to the joint rather than the muscle-tendon units. Fig. 4.4 illustrates the physics-based joint model. It shows a frame of the joint in the simulated environment, indicating the femur, tibia, and FeTi joint.

In contrast to the antagonistic-MTU configuration, however, the physics-based model is actuated by a single MTU representing the extensor muscle. This MTU includes only the active component responsible for generating force based on its activation state. All passive mechanical effects, including joint elasticity, viscous resistance, and gravitation load, are

specified directly at the joint level through MuJoCo. Therefore, the extensor MTU provides the sole torque input, while the joint's passive response is handled by the physics engine.

Under these assumptions, the total torque input $\hat{T}_{\text{in}}$ applied to the MuJoCo joint is

$$\hat{T}_{\text{in}} = \hat{F}_{\text{ext}}\, \hat{r}_{\text{ext}}\,, \tag{4.16}$$

where each $\hat{F}_{\text{ext}}$ is given by equation 4.13.

The muscle lengths and moment arms follow the same geometric definitions used introduced earlier: $L_m^{\text{ext}} = \cos\theta$, and $r_{\text{ext}} = -\sin\theta$. Because MuJoCo evaluates the passive mechanics of the system, the rotational equation of motion (equation 4.15) no longer needs to be integrated explicitly. Instead, joint motion is computed automatically from the supplied torque input and the specified mechanical parameters.

The physics-based joint model follows the structural configuration described in Section 3.2, but is parametrised using measurements from the femoral-tibial (FeTi) joint of the locust hind leg. This biological system serves as a reference for the results presented later in Sections 5.3.2 and 5.3.3. Consequently, the tibial segment in the simulation is assigned with dimension and mass values obtained from experimental studies of the locust hind leg [127]. Specifically, we use a tibial length of $l_{\text{tibia}} = 22.8\,\text{mm}$ and mass of $m_{\text{tibia}} = 14.9\,\text{mg}$. These values determine the geometry, mass distribution, and resulting inertial properties supplied to the simulation.

To ensure that simulated movements remain within physiologically realistic bounds, the range of motion of the joint is constrained using experimentally measured limits of FeTi joint motion [3]. Based on this data, the allowable angular range in the model is set to 150° (see Fig. 4.4), keeping the simulated kinematics within the natural operating limits of the locust hind leg.

Actuation is implemented using a torque actuator applied to the joint. At each simulation step, the extensor MTU model outputs a dimensionless torque based on the muscle activation level A_m, scaled muscle-tendon length $\hat{L}_m$, and scaled muscle-tendon contraction velocity $\hat{\dot{L}}_m$. Because of MuJoCo operates entirely in physical units, this dimensionless torque needs to be converted into physically meaningful torque before it can be applied to the joint. This conversion uses the torque scale obtained in the nondimensionalisation derivation (see Appendix A.1.2 for details), where the characteristic length, damping, and time scales of the extensor MTU define the physical torque magnitude. The resulting conversion is

$$T_{\text{phys}} = \hat{T}_{\text{in}}\, \frac{(L_0^{\text{ext}})^2\, \beta_{\text{max}}^{\text{ext}}}{\tau}\,, \tag{4.17}$$

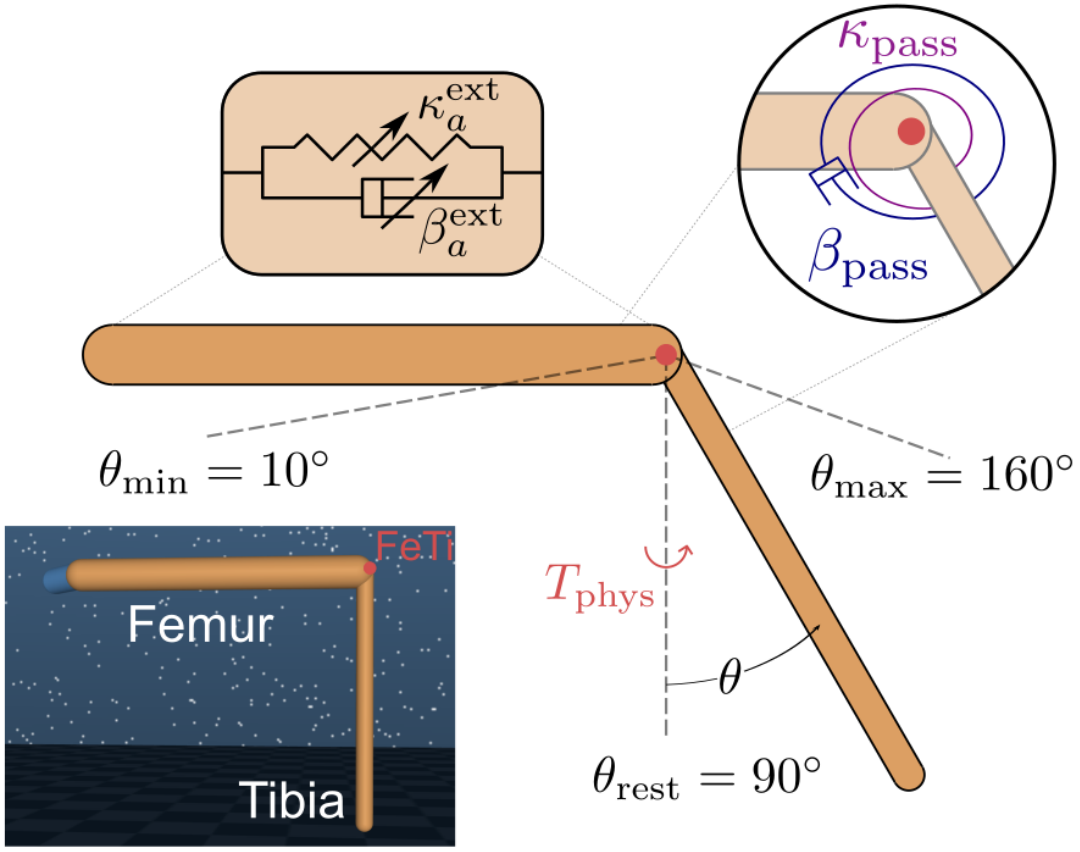

Figure 4.4: Schematic of the physics-based joint model representing the femoral-tibial (FeTi) joint of the locust hind leg, highligted with a red circle. The femur and tibia are modelled using primitive geometric bodies defined in MuJoCo. In the restin configuration (θ_{rest}), the tibia hangs perpendicularly to the femur. Tibial rotation occurs about the FeTi joint within a defined range of motion, bounded by θ_{min} and θ_{max}. The direction of the extensor-generated torque T_{in} is indicated relative to the rotational axis. Two insets illustrate the components contributing to joint dynamics: (i) the active extensor MTU, characterised by its linear stiffness κ_a^{ext} and damping β_a^{ext}, and (ii) the passive joint mechanism, represented as a rotational stiffness κ_{pass} and damping β_{pass}. A a snapshot of the MuJoCo model is included in the corner, identifying the femur, tibia and the FeTi joint (highlighted in red), linking the schematic to its physical implementation in the simulation environment.

where

$$L_0^{\text{ext}} = 20.52\,\text{mm}\,, \quad \beta_{\text{max}}^{\text{ext}} = 20\,\frac{\text{dyn}\,\text{s}}{\text{cm}}\,, \quad \tau = 1\,\text{s}\,.$$

These values are taken from experimentally reported measurements of the locust extensor tibiae muscle [19, 49, 127], ensuring that the physical torque scale remains grounded in biologically realistic parameters. The term $\hat{T}_{in}$ corresponds to the nondimensional MTU torque defined in equation 4.16.

We use the physical torque T_{phys} to drive the MuJoCo actuator, ensuring that the torques applied to the joint correspond to the nondimensional prediction. The simulation is implemented the CGS unit system to remain consistent with the anatomical and biomechanical data available for the locust hind leg. Gravity is enabled and acts along the negative z-axis with magnitude $g = 981\,\text{cm}\,\text{s}^{-2}$.

The model is simulated using MuJoCo's semi-implicit Euler integrator with a time step of 0.001 s. The joint is initialised at its resting configuration (a 90° tibial angle relative to the femur) with zero angular velocity. This setup provides a well-defined reference state from which the effects of active MTU torque, passive joint mechanics, and gravitational loading can be evaluated in isolation or combination, completing the specification of the physics-based joint model.

4.7 The Insect Whole-Body Model

Here, we present an insect model that builds directly on the physics-based joint model introduced in Section 4.6. This joint model is used as the fundamental building block from which multi-joint limbs and, ultimately, a full articulated body are constructed. Naturally, by assembling multiple instances of the same joint architecture, each with its own geometry, passive viscoelasticity, and muscle-driven torque input, the model scales from a single DoF to a multi-segment structure capable of producing coordinated limb motion. The whole-body model provides a generalisable framework for physics simulation to study musculoskletal coordination at the scale of an individual limb or the entire organism.

To construct the insect whole-body model, we use the morphology and kinematic structure of a dung beetle. This insect is selected because detailed measurements of segment lengths, masses, and joint locations have been reported in previous robotic and biomechanical studies [11, 108]. These measurements thus provide us with a coherent anatomical reference for model parametrisation. However, the modelling framework is sufficiently general to adopt the morphology and joint architecture of other insect species, making the approach broadly transferable beyond the dung beetle exemplar.

Using the anatomical values reported in these studies, we recreate an approximate 3D representation of the animal in Blender [13], as illustrated in Fig. 4.5A. The relative simplicity of the model relies on the use of simple geometric primitives, such as spheres, cylinders, and ellipsoids, to capture the shape and proportions of the thorax, abdomen, and limb segments of the insect, following the framework provided in [116].

The model consists of 20 body segments. Two ellipsoids represent the main body:

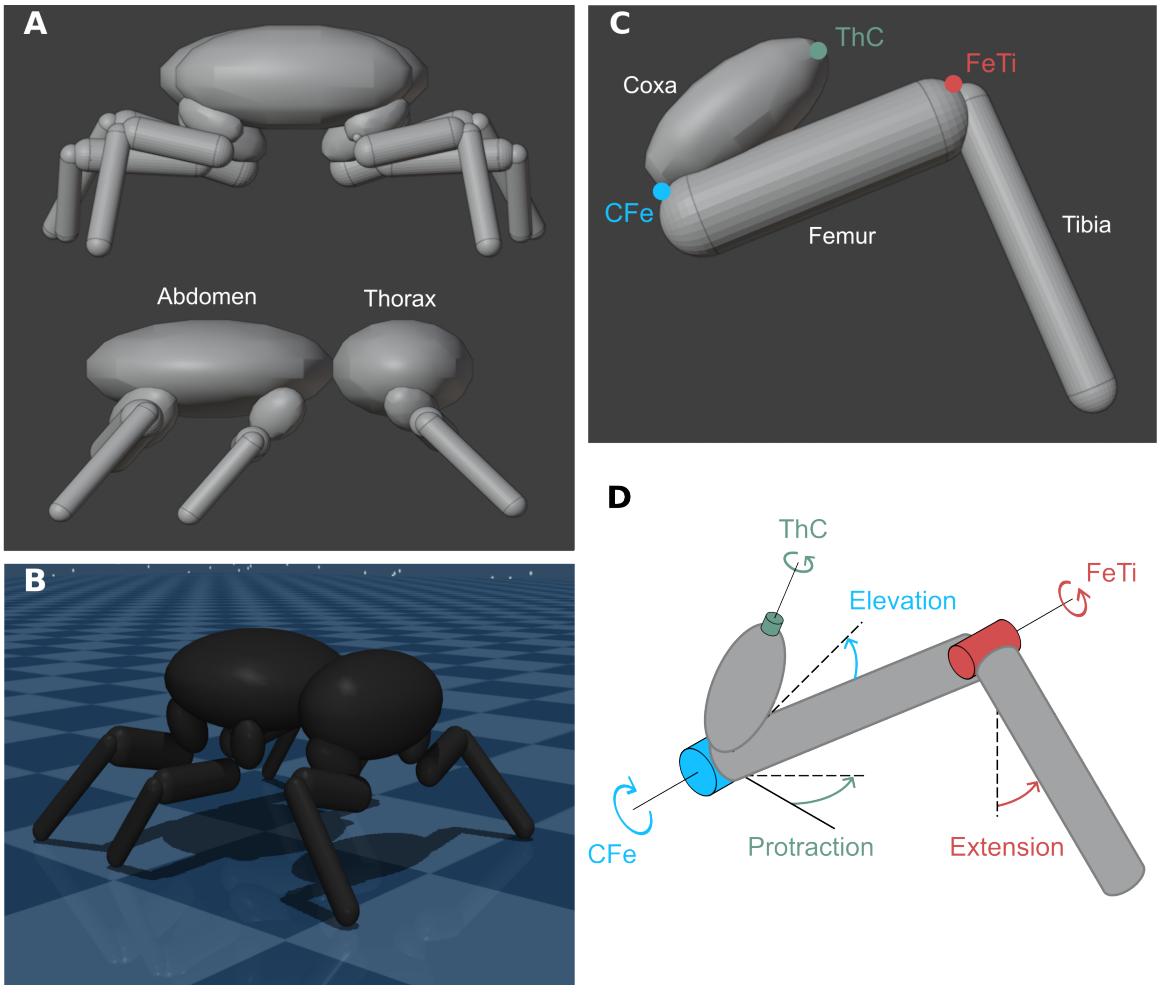

Figure 4.5: The insect whole-body model. (A) Frontal and sagittal views of the Blender model. The sagittal view highlight the ellipsoidal geometries representing the the abdomen and thorax. (B) MuJoCo rendering of the model in its passive standing posture. (C) A representative leg of the model showing its three segments: coxa, femur and tibia. The thorax-coxa (ThC, green), coxa-femur (CFe, blue), and femur-tibia (FeTi, red) joints are marked with circles. (D) Schematic of the same representative leg illustrating its kinematic configuration. Positive torques about the ThC joint produces leg protraction. Positive torque at the ThC joint protracts the leg, at the CFe joint elevates the femur, and at the FeTi joint extends the tibia.

thorax, and abdomen (Fig. 4.5A). Each of the six legs is composed of three segments: an ellipsoidal coxa and two capsule-shaped (cylinders capped with hemispheres) representing the femur and tibia. The joint centres and rotational axes are positioned according to the anatomical values reported in [11]. Thus, ensuring that the simulated DoFs match the natural kinematic configuration of the dung beetle. These geometric segments are then organised into a hierarchical kinematic structure, *i.e.* armature, within Blender.

This simplified anatomical representation in Blender is used as a structural basis for

Body part		
	Thorax	Abdomen
Length [cm]	0.51	0.90
Width [cm]	0.91	1.03
Height [cm]	0.43	0.40
Mass [g]	0.0238	0.0304

Leg segments			
	Front	Middle	Hind
Coxa			
Length [cm]	0.24	0.21	0.40
Width [cm]	0.16	0.16	0.16
Mass [g]	0.0012	0.0015	0.0030
Femur			
Length [cm]	0.32	0.42	0.46
Width [cm]	0.18	0.20	0.24
Mass [g]	0.0028	0.0022	0.0026
Tibia			
Length [cm]	0.46	0.37	0.55
Width [cm]	0.10	0.09	0.09
Mass [g]	0.0015	0.0013	0.0021

Table 4.2: Dimensions of body (thorax and abdomen) and legs (coxa, femur, and tibia), in CGS units, used to parameterise the whole-body insect model. Values are taken from [108].

building the insect model in the MuJoCo physics engine (see Fig. 4.5B). The geometric components corresponding to the thorax, abdomen, and leg segments are assigned with length and masses values using the reported measurements in [108]. See Table 4.2 for full parameter specifications. As in the physics-based joint model, MuJoCo uses these masses and geometric values to compute the moments of inertia of each segment under the assumption of uniform density. Each body part is treated as a rigid segment; we assume that there are no joints and movement in the thorax and abdomen.

Every leg joint in Blender armature maps directly onto a revolute joint in MuJoCo. The coxa attaches to the thorax through the thorax–coxa (ThC) joint, which has three DoFs. The coxa connects to the femur via the coxa–femur (CFe) joint with two DoFs, and the femur connects to the tibia via the femur–tibia (FeTi) joint with a single DoF. For the purposes of this thesis, and to maintain the model simple, we reduce the joint complexity by locking two DoFs of the ThC joint and one DoF of the CFe joint during simulation time. Fig. 4.5C shows a representative leg, indicating the three leg segments and joints. As a result, each leg consists of a functional kinematic chain with three active DoFs: 1) one at the ThC joint enabling protraction–retraction of the coxa, 2) one at the CFe joint enabling elevation–depression of the femur, and 3) one at the FeTi joint enabling flexion–extension of the tibia (see Fig. 4.5D).

Joint	Proximal–Distal	Front Leg	Middle Leg	Hind Leg
ThC	Proximal	27	25	30
CFe	Intermediate	9	8	10
FeTi	Distal	4	3	5

Table 4.3: The joint-specific values of the torque scaling factor S_m used to convert nondimensional joint torques into physical units. Thorax-coxa (ThC) joints are proximal, coxa-femur (CFe) joints are intermediate, and femur-tibia (FeTi) joints are distal.

For each joint, we assign physiologically informed limits based on observations reported for dung beetles [108]. These limits ensure that the simulated ranges of motion remain consistent with the joint movements observed experimentally. Specifically, we set the ThC joint limits differently across the three pair of legs: 95° for the front legs, 115° for the middle legs, and 160° for the hind legs. In contrast, the CFe and FeTi joints share equal rotational ranges across all legs. Accordingly, we assign 90° of rotation to the CFe joint and 170° to the FeTi joint.

To actuate each DoF of the leg joints, we use torque actuators. These are driven by antagonistic pairs of nondimensional MTUs, allowing each joint to produce its characteristic movements: protraction-retraction, elevation-depression, and flexion-extension. Similarly to the configuration of the physics-based model (Section 4.6.1), activation-dependent forces generated by the MTUs define the nondimensional active torque, which is then converted into physical units before being applied to the corresponding torque actuator in MuJoCo. This conversion is given by

$$T_{\text{phys}} = \hat{T}_{\text{in}} \frac{(L_0^{\text{fl}})^2 \, \beta_{\text{max}}^{\text{fl}}}{\tau} = \hat{T}_{\text{in}} \, S_m \,, \tag{4.18}$$

where $\hat{T}_{\text{in}} = \hat{F}_{\text{fl}} \, \hat{r}_{\text{fl}} + \mu_m (\hat{F}_{\text{ext}} \, \hat{r}_{\text{ext}})$. For details of these derivations, refer to Appendix A.1.3.

In this context, S_m acts as a scaling factor that captures the net gain of the transformation from activation to joint torque. As such, it can be interpreted as a representation of electromechanical coupling at the joint. Importantly, S_m is assigned individually for each joint to account for differences in torque requirements across the leg. This choice follows the proximal-distal organisation observed in animal limbs, where proximal joints are actuated by larger and stronger muscles, while distal joints are driven by muscles that are lighter and more compliant [26, 65]. Accordingly, S_m can also be understood as a scale of muscle mass, with larger values used for proximal joints and smaller values for distal joints. The values of S_m used for each leg joint are given in Table 4.3.

Additionally, we assign stiffness and damping values to each joint to define their passive viscoelastic properties. These values are selected such that the model can support its body

weight passively, without requiring any active muscle torque. This design choice reflects the fact that insect exoskeletons possess substantial intrinsic stiffness that can maintain posture and resist deformation even when the muscles are inactive or experimentally removed [4, 63, 98]. The selection of these passive parameters are directly consistent with our physics-based joint analysis, ensuring continuity and comparability across the models. Refer to Section 7.2.1 for details on the selection of these values.

Ground contact was modelled using the native Couloumb friction contact solver from MuJoCo, with an elliptic friction cone approximation. Contacts between the legs of the model and the ground plane were resolved with a sliding friction coefficient of 0.5, and with torsional and rolling friction values of 0.005 and 0.0001, respectively. Contact constraints were solved using a stiff, near-rigid reference model with three additional no-slip solver iterations applied per timestep to reduce residual tangential drift during stance, following [116]. Contralateral leg-segment pairs were explicitly excluded from mutual collision to avoid unwanted contact forces from overlapping proximal geometry. Finally, as in the physics-based joint model, the whole-body insect model is simulated using the semi-implicit Euler integration method from MuJoCo with a time step of 0.001 s. Simulations are performed using the CGS unit system, with gravity enabled and set to $g = 981\,\mathrm{cm\,s^{-2}}$.

4.8 The Muscle Activation Model

The muscle activation dynamics is modelled as a leaky integrator model that transforms discrete motor neurone spikes into a continuous activation signal driving force generation. This simplified formulation provides a biologically plausible description of the excitation-contraction process while remaining computationally efficient. The model derives conceptually from the leaky integrate-and-fire (LIF) neurone framework [33, 80], where the integration of discrete inputs and gradual leakage emulate the temporal summation and decay of activation observed in muscle fibres [17, 52, 93, 94].

In this formulation, the motor neurone is represented as a spiking unit, where each spike generated by the neural drive corresponds to a discrete event occurring at time t_i. Each of these discrete events produce a continuous excitatory response, which is shaped by an alpha function as follows

$$U(t) = \sum_{t_i<t} \left(\frac{t - t_i}{\tau_s}\right) \exp\left(1 - \frac{t - t_i}{\tau_s}\right), \tag{4.19}$$

where τ_s defines the timescale of the spike response. This kernel captures the key features of excitation-contraction coupling following a spike: a rapid rise in intracellular calcium

concentration due to sarcoplasmic reticulum release, followed by an exponential decay as calcium is re-sequestered [124]. The contributions from successive spikes sum linearly, meaning that closely spaced spikes overlap to create larger, more sustained inputs.

To produce the continuous muscle activation signal, the resulting drive signal $U(t)$ is filtered through a first-order leaky integrator given by

$$\frac{dA_m(t)}{dt} = \frac{1}{C_a}\Big[- g_a\, A_m(t) + g_u\, U(t)\, \big(A_{m,\,\max} - A_m(t)\big)\Big]\,. \tag{4.20}$$

$A_m(t)$ is the unitless activation state of the muscle (ranging from 0 to $A_{m,\,\max}$), C_a is the activation capacity constant, and g_a and g_u are rate constants governing deactivation and neural input strength, respectively. The term g_u represents the neuromuscular transmission gain, scaling the magnitude of the neural input to the activation system. The characteristic time constant of the activation process, $\tilde{\tau}_a = C_a/g_a$, therefore reflects the effective time scale of excitation-contraction coupling rather than the electrical time constant of the muscle membrane. We make this distinction due to the fact that in reality, muscles exhibit delays associated with calcium handling and cross-bridge recruitment, and do not respond immediately to neural inputs.

In the absence of neural input (*i.e.* $U(t) = 0$), the decay of activation remains linear with time constant $\tilde{\tau}_a$, reflecting calcium reuptake and cross-bridge detachment. However, the excitatory drive from the motor neurone is progressively diminished as A_m approaches its upper bound $A_{m,\,\max}$. This mechanism ensures that the activation state asymptotically approaches a physiological maximum, rather than increasing without limit, which reflects the finite number of cross-bridge binding and the saturation of calcium-troponin interactions: when most binding sites are occupied, additional calcium influx has little effect on further recruitment [124]. Mathematically, this formulation embeds the saturating behaviour directly with the dynamics of the muscle activation equation. Equations 4.18 and 4.19 reflect the fact that the muscle activation integrates incoming calcium signals over time with a leakage, *i.e.* decay, when input ceases, much like a resistor-capacitor circuit [119]. Thus, the activation model allow us to capture the transition from discrete motor neurone spikes to smooth muscle activation dynamics: single spikes produce twitch-like responses, repeated spikes summate, and high-frequency input leads to a sustained activation plateau resembling tetanus.

To account for history-dependent effects in muscle activation, we extend the activation dynamics by introducing an adaptive deactivation mechanism that modulates the relaxation time scale based on the recent activation state of the muscle. Experimental studies have shown that muscle relaxation becomes progressively slower following repeated or high-frequency stimulation. Whereas the response to an isolated twitch follows a consistent

activation–relaxation profile, closely spaced pulses lead to a prolonged decay of activation [93, 94]. A fixed deactivation rate is therefore insufficient to reproduce the asymmetric rise–decay profiles observed in multi-spike muscle responses.

In this extended formulation, the deactivation gain g_a is no longer constant, but instead depends on the instantaneous activation level A_m through a sigmoidal relationship,

$$g_a(A_m) = \frac{g_{a,\max}}{1 + e^{S_{g_a}(A_m - A_{m,\text{off}})}} + g_{a,\text{off}}\,, \tag{4.21}$$

where $g_{a,\max}$ defines the maximum contribution of the adaptive component, S_{g_a} controls the steepness of the transition, $A_{m,\text{off}}$ sets the activation level at which the reduction in g_a becomes pronounced, and $g_{a,\text{off}}$ is a constant offset ensuring a non-zero lower bound.

As a consequence, the effective activation time constant becomes dependent on activation,

$$\tilde{\tau}_a(A_m) = \frac{C_a}{g_a(A_m)}\,,$$

such that increased muscle activation leads to a longer relaxation time scale. Importantly, the update of g_a is conditional: the deactivation gain is allowed to evolve only during periods of active excitation, *i.e.* when neural input is present and activation is increasing. During the relaxation phase, when neural input ceases, g_a is held constant at its most recently attained value. As a result, once the muscle has been driven to a high activation state, the deactivation gain remains reduced even as activation decays, leading to a relaxation phase that is slower than the preceding activation phase. The magnitude of this effect depends on both the peak activation reached and the steepness of the sigmoid in equation 4.21.

By embedding activity-dependent slowing directly into the activation dynamics, this adaptive mechanism provides a compact and physiologically motivated means of capturing history-dependent muscle behaviour without introducing additional state variables or explicit calcium dynamics.

Chapter 5

Single Joint with a Single Muscle

5.1 Overview

In this chapter, we consider the findings of Ache and Matheson [3] regarding their locust hind leg experiments as benchmarks to test how simplified joint models can reproduce biological extension-flexion cycles. Following their experiments, Ache and Matheson found that a single extensor motor neurone is sufficient to generate cyclic movements, with active forces generated by the extensor tibiae muscle driving tibial extension, while passive joint forces generating flexion. This finding provides us with an ideal test case for our own modelling model frameworks, which aim to capture the interplay between active, neurone-driven muscle dynamics and the passive viscoelastic properties of the joint. By reproducing the experimental conditions posed by Ache and Matheson, we assess how different model formulations and levels of mechanical abstraction account for the same biological behaviour.

Three modelling approaches are implemented throughout this chapter: i) the single-MTU model presented in Section 4.3; ii) the physics-based joint model described in Section 4.6; and lastly, iii) the physics-based joint model with an incorporated muscle activation model to feed the muscle of the joint. In this chapter, we refer to model iii) as the neuromechanical model for simplicity. All the approaches successfully replicate the overall joint behaviour observed experimentally, showing that a minimal neuromechanical system is sufficient to produce locust-like extension–flexion cycles. However, in the three models, a fixed activation constant was insufficient to account for the full range of joint dynamics. Introducing an adaptive activation improved the correspondence with experimental behaviour, suggesting that insect muscles adjust their effective activation dynamics based on recent activity rather than operating with a single, fixed time constant.

The results presented here demonstrate the sufficiency of active–passive interactions for

generating realistic joint behaviour. This work establishes the baseline neuromechanical framework for reproducing insect limb motion and provides the foundation for the next chapter, where the model is extended to include antagonistic muscles to investigate how muscle asymmetry and joint passive elements interact.

This chapter begins in the background Section 5.2 where we introduce the readers to the anatomy of the locust hind leg (Section 5.2.1), including its musculature and motor neurone organisation. Following this, we summarise the experimental paradigm (Section 5.2.2) and main findings (Section 5.2.3) from the experiments done by Ache and Matheson to investigate the passive joint mechanics in the locust hind leg. Next, Section 5.3 presents our modelling results, detailing the three modelling approaches i) (Section 5.3.1), ii) (Section 5.3.2) and iii) (Section 5.3.3), where we reveal that reproducing both twitch-like and repeated joint responses requires an adaptive time scale in the muscle activation dynamics. Finally, the discussion (Section 5.4) interprets these findings in the broader context of insect limb biomechanics and establishes the foundations for Chapter 6.

5.2 Background

In this section, we give context to the reader by providing a description of the anatomical and functional characteristics of the locust hind leg, particularly the femoral-tibial joint. This joint plays a central role in the motor behaviours under investigation within this chapter. The experimental paradigm we employ in this study builds upon previously published work that examined the neuromuscular control of tibial movements through targeted stimulation of the extensor motor neurone. The following sections outline the relevant anatomical features and summarises key findings from the foundational experiments that informs the protocol used in this chapter.

5.2.1 Anatomy of the Locust Hind Leg

Locusts are insects that exhibit highly adaptable and efficient movement strategies across different environments. They possess much longer hind legs compared to their front and middle pairs. These hind legs display a wide repertoire of complex motor behaviours, including walking [99], kicking [19], postural stabilisation [39], scratching [127], among others. Despite this versatility, the hind legs are highly specialised for jumping [10, 53]. This specialisation is reflected in their unique joint geometry and mechanical adaptations, such as a locking mechanism that enables the leg to remain in a mechanically loaded state. During this phase, elastic energy is stored and subsequently released to enhance the speed and force of the jump. The geometry of the lever arm also varies with the joint angle,

optimising the mechanical advantage of the extensor muscle during powerful extensions [53].

Structurally, the hind leg comprises several segments, among which the femur and tibia are the most prominent. These rigid segments are connected by the femoral-tibial (FeTi) joint, *i.e.* the knee, which facilitates extension and flexion of the tibia. The FeTi joint exhibits a rotational range of motion of approximately 150° [53]. In the absence of muscle activation, the tibia rests at an angle between 80°-100° relative to the femur [3]. Full flexion reduces this angle to approximately 10°, while full extension increases it to around 160°.

The movements of the FeTi joint result from the coordinated contractions of two muscles located in the femur: the extensor tibiae (ETi) and the flexor tibiae (FTi) [19]. These muscles attach to the tibia via the apodemes, which function similarly to tendons. The ETi muscle is significantly larger and more powerful than the FTi, weighing roughly five times more and generating over 20 times the force [3]. This pronounced asymmetry enables the locust to produce rapid and forceful extensions necessary for effective jumping.

Muscle contractions in both the ETi and FTi are driven by excitatory motor neurones (EMNs) [87]. Each muscle contains distinct fibre types, which are selectively activated by specific EMNs. The FTi muscle receives input from nine EMNs, categorised into fast, intermediate, and slow groups based on their firing patterns and the nature of contractions they elicit. In contrast, the ETi muscle is innervated by only two EMNs: the slow extensor tibiae (SETi) and the fast extensor tibiae (FETi) [20]. Each EMN targets a unique subset of muscle fibres, resulting in spatially specific activation patterns.

5.2.2 Experimental Paradigm

To investigate the mechanisms underlying passive tibial movements in the locust hind leg, Ache and Matheson developed a controlled stimulation protocol that isolated FETi motor neurone (MN) activity. Their objective was to determine whether cyclic extension-flexion movements in the locust hind leg could be generated without active flexor muscle contractions.

Ache and Matheson conducted their study on seven locusts with denervated hind legs, in which the nerve supplying the leg was cut to eliminate descending motor commands and sensory feedback. This ensured that all observed movements resulted exclusively from experimentally induced MN activity. They kept the hind leg attached to the animals and mounted in a fixed position. All joints of the hind leg, except the FeTi joint, were immobilised, allowing the tibia to move freely.

They selectively stimulated the FETi motor neurone, which innervates the extensor tibiae muscle as mentioned before. Using a pair of pin electrodes, they stimulated the FETi directly by inserting the electrodes into the 4th to 6th proximal bundles of the ETi muscle. They then applied electrical stimulation using three different protocols: i) a single FETi spike to produce an isolated twitch; ii) five FETi spikes at 7.5 Hz to generate a low-frequency burst; and iii) five FETi spikes at 20 Hz to induce a high-frequency burst.

Finally, they recorded the resulting FeTi joint movements using high-speed video, which allowed them to analyse both joint angle trajectories and passive return dynamics, following extensor activation.

5.2.3 Key Findings from the Ache–Matheson Experiment

Following their experiments, Ache and Matheson demonstrated that cyclic extension-flexion movements in the locust hind leg can occur through extensor MN activity alone, without any contribution from the flexor muscle. Their results showed that passive joint forces are sufficient to flex the tibia and complete the movement cycle.

When they applied a single spike to the FETi (Fig. 5.1A), they observed three distinct outcomes: i) the tibia extended rapidly, reaching a peak velocity 810°/s; ii) the extension remained incomplete, stopping short of the anatomical maximum of approximately 19°; and iii) the tibia returned toward its initial position through passive flexion. With five spikes at 7.5 Hz (Fig. 5.1B), the stimulation produced a series of repeated extensions, each followed by a smaller passive flexion. This pattern resembled natural cyclic movement such as aimed scratching. At a higher stimulation frequency of 20 Hz (Fig. 5.1C), the tibia reached a full extension and maintained that position for approximately 250 ms before passively returning to its starting angle.

In all stimulation regimes, the tibia returned entirely passively to the resting position of the FeTi joint (80°-100°, see Section 5.2.1), without any flexor activity, as the legs were denervated. Ache and Matheson observed highly consistent passive return movements across trials and locusts. Increasing the number and frequency of spikes slightly increased the extension velocity, from 810°/s with a single spike to 860°/s with five spikes at 20 Hz. These findings confirmed that activating the extensor MN can generate complete tibial movements where passive joint mechanics reliably produce the flexion phase. This highlights the essential role of passive forces in insect motor control and thus supports our modelling approach, demonstrating that passive elements are not just supplementary, but fundamental to capturing biologically realistic joint dynamics.

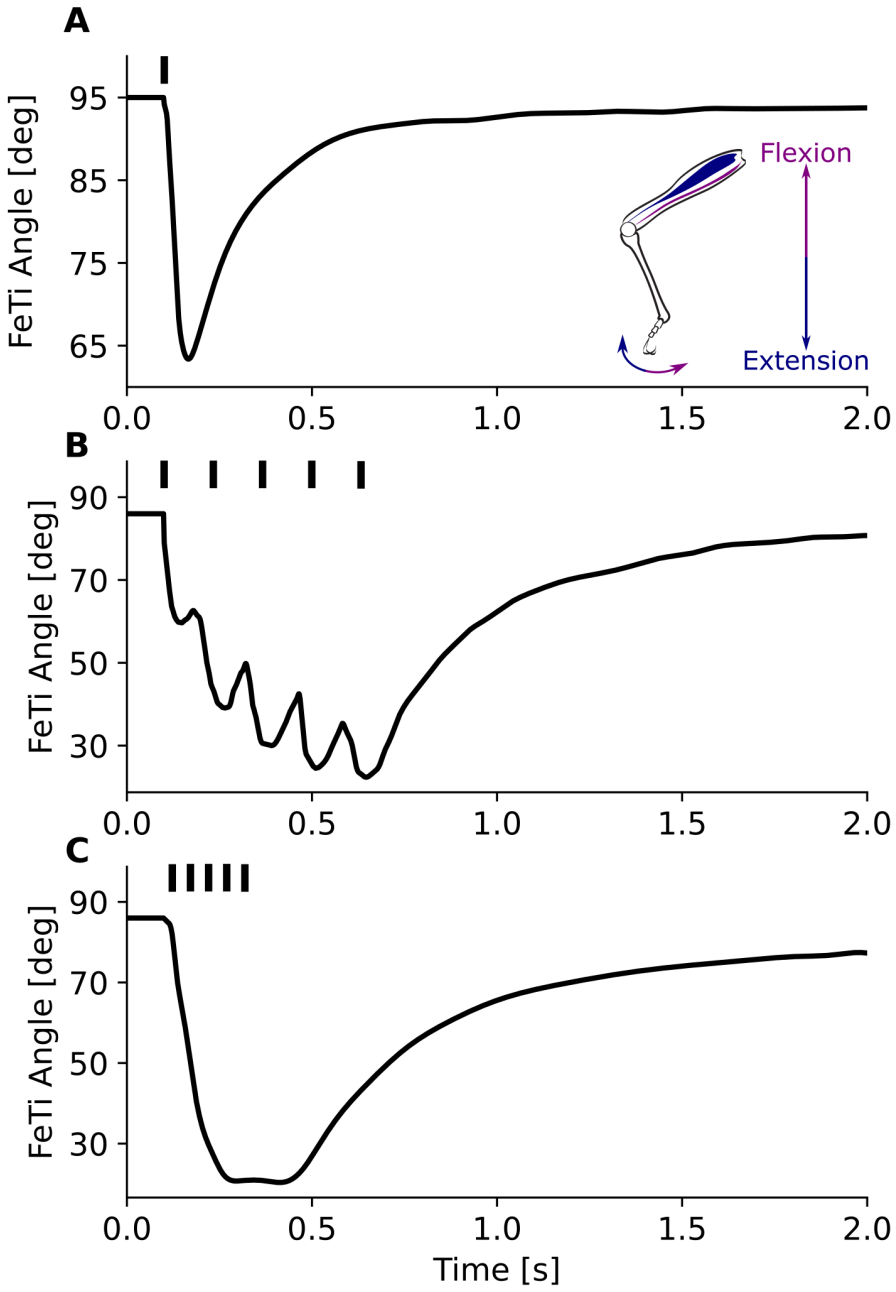

Figure 5.1: Passive flexion movements in the locust FeTi joint. Adapted from [3]. Decrements in joint angles correspond to extension movements. (A) A single spike stimulation of the FETi motor neurone triggers a rapid tibial extension followed by passive flexion. (B) Stimulation with five spikes at 7.5 Hz induces repeated extensions, each followed by a progressively smaller passive flexion. (C) Five spikes at 20 Hz result in a sustained full extension of the tibia, followed by gradual passive flexion returning to equilibrium.

5.3 Results

In this section, we present results from three complementary modelling approaches: i) the single-MTU joint model, ii) the physics-based joint model implemented in MuJoCo, and iii) the neuromechanical model that integrates motor neurone activity with muscle activation dynamics. The goal of these analyses is not only to replicate experimental data from the locust extensor tibiae muscle [3], but also to probe the mechanisms by which joint motion emerges from the interaction of active and passive forces. While Ache and Matheson examined three stimulation protocols (single-spike, 7.5 Hz, and 20 Hz), here we focus our analysis on the single-spike and 20 Hz conditions, which define the lower and upper bounds of the activation frequency range. These two cases are sufficient to evaluate the ability of the modelling approaches i), ii), and iii) to capture both transient and sustained dynamics while keeping the parameter estimation tractable.

Specifically, our results are structured around three central questions: to what extent can joint behaviour be explained by passive mechanics alone; whether adaptive muscle activation dynamics is necessary to account for the differences between brief and sustained stimulation; and how consistent these principles remain across modelling levels, from abstract formulations to physically realistic simulations. These questions provide the framework for interpreting the modelling results, from the limitations of simple passive and active formulations to the resolution achieved by introducing adaptive activation dynamics.

5.3.1 Single-MTU Joint Model

In this section, we examine the response of the joint at the first level of the modelling hierarchy, the single-MTU model. This setup mirrors the mechanical configuration of the locust FeTi joint, where torque production arises from the interaction between active, muscle-generated forces and passive viscoelastic forces. Throughout this analysis, we exclude the flexor MTU from the joint model, in line with Ache and Matheson, who showed that passive flexions primarily arise from the viscoelastic properties of the joint rather than flexor activation. Consequently, it is reasonable to model only the activity of the extensor MTU. This activity is driven by square pulses of certain duration. Furthermore, we assume that the passive viscoelastic properties are integrated within the extensor MTU. Fig. 5.2 shows the modelling approach we use in this section. Under these assumptions, the nondimensional formulation reduces the system dynamics to the extensor MTU's dimensionless parameters (η_a^{ext}, η_p^{ext}, μ_j^{ext}) along with the parameters γ and $\hat{J}$. In addition, we define the characteristic length as $L_0 = 0.02052\,\text{m}$, corresponding to the resting length of the extensor tibiae muscle in the locust hind leg [3, 19], and the time scale as $\tau = 1\,\text{s}$, representing the period of a full tibial extension-flexion cycle.

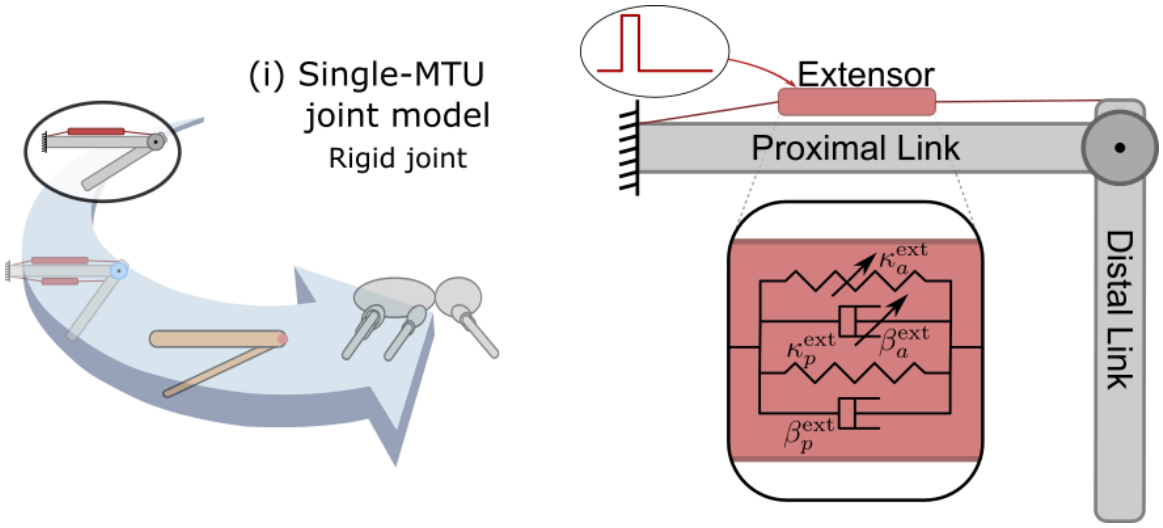

Figure 5.2: In this section, the first level of the modelling hierarchy, the single-MTU joint model, is used. The joint is actuated by a single MTU that includes both the active and passive components, which is activated with square pulses.

Geometrically, the resting length L_0 corresponds to a resting joint angle of $\theta_{\text{rest}} = 90°$, consistent with the experimentally observed resting joint configuration of the locust FeTi joint (see Section 5.2.1). In the locust, the resting joint angle arises from a passive mechanical equilibrium between assistive forces from muscle and joint elastic tissue, and restrictive forces such as joint friction, as well as the structural preferred angle of the joint cuticle [50, 63]. Because passive viscoelastic forces in the FeTi joint are large relative to the gravitational load on the distal link [4], this equilibrium is primarily determined by the intrinsic mechanical properties of the joint rather than by gravitational loading, and the resting joint angle remains largely consistent across leg configurations regardless of whether the limb is acting against or with gravity. The choice of $\theta_{\text{rest}} = 90°$ in the model therefore reflects this experimentally grounded passive equilibrium.

With these definitions established, we simulate the joint response to a single pulse activation profile, replicating the experimental protocol of Ache and Matheson for a single-spike stimulation (Fig. 5.1A). We model a single spike as a brief square pulse of maximum muscle activation ($A_m = 1$) lasting 3 ms, consistent with stimulation durations reported in [124]. To estimate the values for the five dimensionless parameters, we activate the extensor MTU with this single pulse and fit the simulated joint trajectory to the corresponding experimental angle displacement (see Fig. 5.1A). We obtain these fits using the differential evolution algorithm [6, 103], implemented using the `SciPy` library. Search bounds were (35,80) for η_a^{ext}, (0.1, 20) for η_p^{ext} and μ_j^{ext}, (0.01, 5) for γ, and (0.00001, 0.01) for $\hat{J}$. The algorithm used the `best1bin` strategy, a population size of 15 individuals per parameter, mutation constant in the range (0.5, 1), a recombination probability of 0.7, a convergence tolerance of 0.01, and a maximum of 1000 generations. The initial population was generated via

Latin hypercube sampling over the parameter bounds rather than a single fixed starting guess. Following convergence, the best candidate was locally refined using L-BFGS-B polishing step. The objective function for model calibration is defined as the sum of squared residuals between the experimental and simulated joint angles, penalising deviations across the entire trajectory to ensure accurate representation of both the extension amplitude and the timing of the passive return. The objective function was the sum of squared residuals between the simulated and experimental joint angle trajectories. Population evaluation was parallelised across 10 CPU cores. Because differential evolution's search is stochastic and no fixed random seed was set, the optimisation was repeated across an ensemble of independent runs ($n = 50$), each with an independently sampled initial population. The run yielding the lowest objective function is given in Table 5.1.

Dimensionless Parameters	
Parameter	**Value**
η_a^{ext}	66
η_p^{ext}	3
μ_j^{ext}	4
γ	0.4
$\hat{J}$	0.0001

Table 5.1: Dimensionless joint model parameters for single-spike experiment.

The calibrated model closely reproduces the experimental single-spike response, capturing both the rapid extension phase and the subsequent passive return to rest (see black trace in Fig. 5.3A). This close correspondence indicates that the nondimensional single-MTU model successfully encapsulates the dominant mechanical interactions driving the joint motion under single-spike activation. However, when the same parameters are applied to multi-spike activations at 20 Hz, the model underestimated the extension of the joint by 12.1° (see black trace in Fig. 5.3B). The deviation becomes more pronounced with increasing activation frequency, suggesting that the mechanical response cannot be fully represented by a single parameter set across different stimulation regimes.

To investigate this discrepancy, we re-optimise the dimensionless parameters using the same fitting procedure, this time targeting the experimental joint trajectory from the five-spikes stimulation at 20 Hz (see Fig. 5.1C). Notably, the recalibration required adjusting only one parameter: the passive stiffness-to-damping ratio η_p, from $\eta_p = 3$ to $\eta_p = 0.05$. This change enables the model to reproduce both the full extension amplitude and the slower relaxation profile observed experimentally (see blue trace in Fig. 5.3B), confirming that the single-MTU model is sufficiently flexible to describe distinct activation regimes, although not simultaneously with a single parameter set. Despite achieving a quantitatively similar

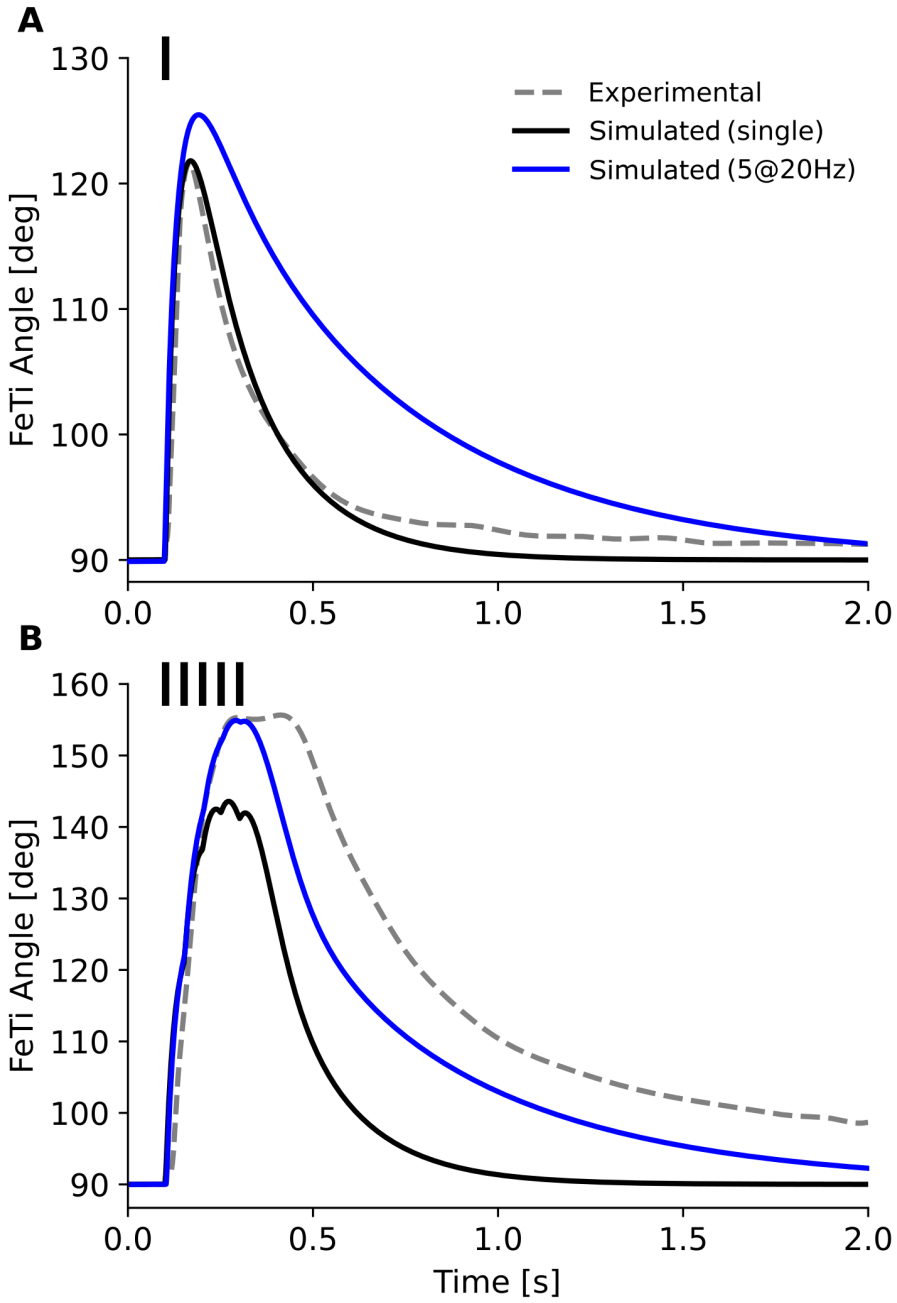

Figure 5.3: Comparison of simulated and experimental joint trajectories under single- and multi-spike activation. (A) The calibrated single-MTU model (black trace) closely matches the experimental single-spike response, capturing rapid extension and passive return. The recalibrated model (blue trace), tuned for multi-spike activation, produces an overly damped and delayed response, failing to reproduce the sharp extension peak. (B) Under five-spike stimulation at 20 Hz, the original model (black trace) underestimates joint extension by 12.1°, while the recalibrated model (blue trace), with $\eta_p = 0.05$, accurately captures both the full extension amplitude and slower relaxation. Nonetheless, it fails to reproduce the sustained extension plateau observed experimentally.

Parameter η_p^{ext} Value	**Single Spike**		**5@20 Hz**	
Metrics	θ_{peak} [°]	τ_{relax} [s]	θ_{peak} [°]	τ_{relax} [s]
Simulated ($\eta_p^{\text{ext}} = 3$)	121.81	0.2064	143.59	0.2274
Experimental	121.62	0.1841	155.66	0.3825
Error	**0.15%**	**12.11%**	7.75%	40.54%
Simulated ($\eta_p^{\text{ext}} = 0.05$)	125.63	0.4898	154.93	0.3614
Experimental	121.62	0.1841	155.66	0.3825
Error	3.3%	166.05%	**0.47%**	**5.5%**

Table 5.2: Comparison of simulated and experimental joint angle metrics under single-spike and five-spikes at 20 Hz stimulation conditions for different values of the dimensionless passive stiffness-to-damping ratio η_p^{ext}. All other dimensionless parameters are held constant. $\eta_p^{\text{ext}} = 3$ yields the smallest error for the single-spike stimulation, while $\eta_p^{\text{ext}} = 0.05$ minimises the error for five-spike at 20 Hz stimulation.

amplitude and relaxation dynamics, the recalibrated model fails to capture the sustained plateau of extension characteristic of the experimental response under repeated and high-frequency activation. In addition, when this recalibrated parameter set is applied back to the single-spike condition, the model produces an overly damped and delayed response (see blue trace in Fig. 5.3A), failing to reproduce the sharp extension peak typical of a single activation.

To quantitatively assess the correspondence between the simulated and experimental joint trajectories, we extract two key metrics: the peak extension amplitude and the relaxation time. The peak extension amplitude θ_{peak} characterises the maximum angular displacement achieved during the extension phase, while the relaxation time τ_{relax} is defined as the time required for the joint angle to decay to $1/e$ of its peak value during passive relaxation. To compare the simulated and experimental results, we use the percent difference as an error metric. This error quantifies the magnitude of deviation of the simulated value from the experimental reference, relative to the experimental value. It is calculated as:

$$\text{Error}\,(\%) = \frac{|X_{\text{mod}} - X_{\text{exp}}|}{X_{\text{exp}}} \times 100\,,$$

where X_{mod} is the values obtained from the simulation and X_{exp} is the corresponding value obtained from the experimental data. These metrics provide a direct comparison of the dynamic behaviour of the model with the experimental data and are summarised in Table 5.2. Together, these results highlight that while the nondimensional single-MTU formulation effectively captures the essential mechanics of joint motion, frequency-dependent variations in the system properties may be necessary to fully account for the observed dynamics across stimulation conditions.

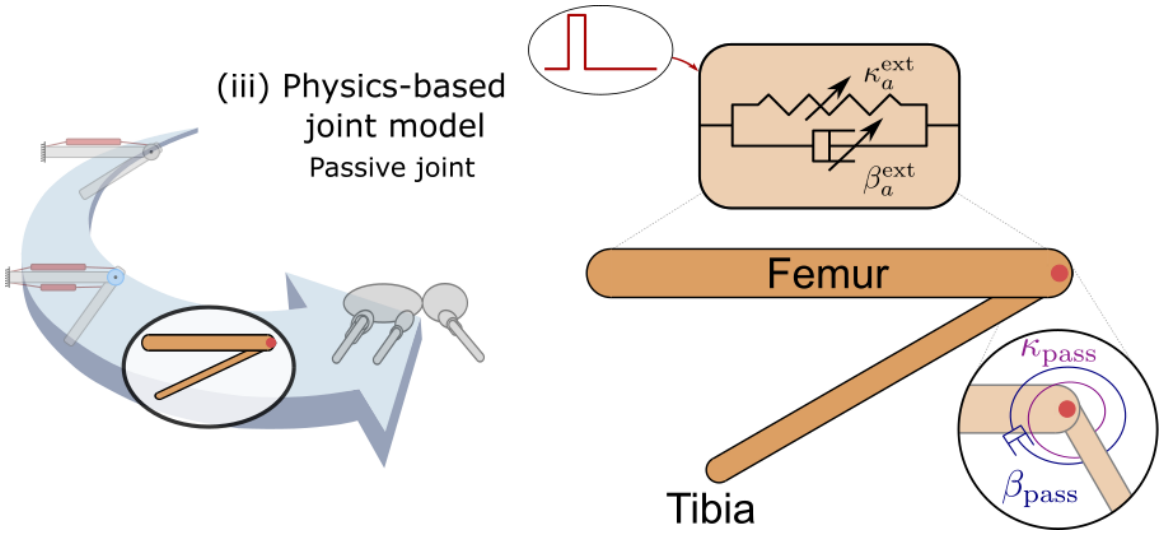

Figure 5.4: In this section, the third level of the modelling hierarchy, the physics-based joint model, is explored to reproduce the Ache and Matheson experiments. The physical joint is actuated only by the extensor MTU and the passive viscoelasticity is located at the joint itself. The extensor is activated with square pulses to drive tibial motion as in Section 5.3.1.

We could address this limitation of the single-MTU model by allowing the relaxation time scale, η_p, to vary dynamically as a function of muscle activation frequency. From a computational perspective, an adaptive η_p would resolve the observed mismatch between model and experiment. Nonetheless, it is unlikely that the viscoelasticity of the joint change substantially with activation frequency. This consideration motivates the next section, where we implement a physically grounded version of the model in a physics-based simulation environment. In this framework, the passive properties are assigned to the joint itself rather to the extensor MTU, following the observations of Ache and Matheson.

5.3.2 Physics-based Joint Model

In this section, we use third level of modelling hierarchy, the physics-based joint model, to reproduce the experimental joint responses described previously (see Fig. 5.4). This model retains the mechanical configuration of the locust FeTi joint but redistributes the passive properties of the muscle-joint system. Specifically, we assign passive stiffness and damping directly to the joint, represented as a rotational spring-damper system. Thus, the extensor MTU includes only the active contractile element. This separation enables a clearer examination of how active muscle forces interact with passive joint properties to shape the overall joint dynamics within a physically grounded simulation environment. For implementation details, please refer to Section 4.6.

To investigate how the redistribution of passive properties to the joint affects its motion, and to evaluate how well the physics-based model reproduces the experimentally observed dynamics, we simulate the single-spike activation protocol using the MuJoCo physics engine. The extensor MTU is activated with a brief 3 ms square pulse at maximum activation ($A_m = 1$), replicating the single-spike condition. We fix the active stiffness-to-damping ratio of the extensor MTU to $\eta_a^{\text{ext}} = 66$, as previously calibrated in the single-MTU model (see Section 5.3.1), to ensure that the contractile behaviour remains consistent across modelling approaches. By keeping the active properties constant, we isolate the contribution of the passive elements to the joint dynamics.

We systematically vary the stiffness and damping values κ_{pass} and β_{pass}, respectively, to examine the effects of the passive joint properties on the simulated tibial trajectory. For each parameter combination, we quantify the mismatch between the simulated and experimental joint angles by computing the root mean square error (RMSE) as follows

$$\text{RMSE} = \sqrt{\frac{1}{N}\sum_{i=1}^{N}\Big(\theta_{\text{exp}}(t_i) - \theta_{\text{sim}}(t_i)\Big)^2}, \tag{5.1}$$

where θ_{exp} and θ_{sim} are the experimental and simulated joint angles and N is the number of time steps of the simulation. The RMSE provides a direct measure of the average deviation between both trajectories over time.

To illustrate our analysis, Fig. 5.5 shows the RMSE contour plot as a function of κ_{pass} and β_{pass}, alongside representative simulated trajectories corresponding to the parameter sets marked by the red and blue crosses in Fig. 5.5A. The black dotted line indicates the combination of κ_{pass} and β_{pass} that yield the same peak angular amplitude as the experimental trajectory. The RMSE landscape highlights a well-defined region of low error within the parameter space, surrounded by zones where the error increases sharply. High κ_{pass} combined with low β_{pass} results in large RMSE values due to rapid joint angular fluctuations that decayed over time. In contrast, low κ_{pass} and low β_{pass} produce slow oscillations with limited attenuation, also leading to elevated RMSE. Increasing β_{pass}, regardless of κ_{pass}, progressively suppressed movement, leading to trajectories with minimal or no extension, and again yielding high RMSE.

We observe that RMSE values converge to zero when β_{pass} is between 0.1 and 1, independent of κ_{pass}. Not surprisingly, this region coincides with the black dotted line that represents the parameters that produce the same peak angular amplitude as the experimental trajectory. Within the range $10^{-4} - 10^{1}$, variations in κ_{pass} have little effect on the motion amplitude. In this regime, damping primarily governed the joint dynamics, controlling both amplitude and relaxation. Beyond $\kappa_{\text{pass}} \approx 10$, we observe a transition to

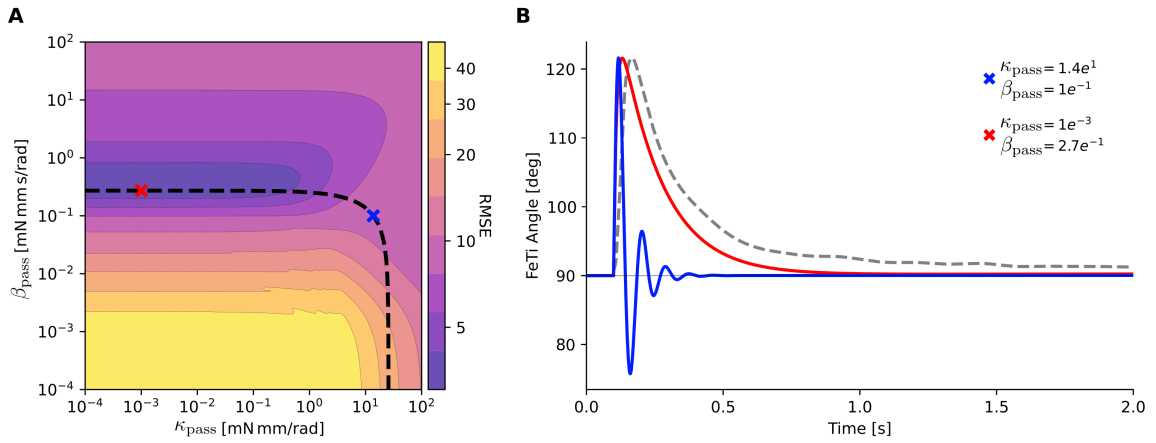

Figure 5.5: RMSE contour plot and representative joint trajectories for selected stiffness and damping parameter sets for physcis-based joint model. (A) RMSE as a function of joint stiffness κ_{pass} and damping β_{pass}, with selected parameter sets marked by red and blue crosses. The black dotted line indicates all combinations of κ_{pass} and β_{pass} yielding the same peak angular amplitude as the experimental trajectory. (B) Simulated joint trajectories corresponding to the red and blue parameter sets, illustrating differences in temporal dynamics despite matching peak amplitude.

stiffness-dominated behaviour where changes in damping no longer influenced the outcome. This transition describes two distinct mechanical regimes: one where viscous resistance shapes the motion and another where elastic forces constrain it.

Fig. 5.5B shows two representative trajectories corresponding to parameter sets, marked with red and blue crosses, located along the black dotted line in the RMSE contour plot. Both trajectories reach the same peak angular amplitude as the experimental data, confirming that the selected combinations of joint stiffness and damping reproduce the correct amplitude. However, their temporal profiles differ noticeably. The trajectory shown in blue exhibits a rapid extension followed by an oscillatory return, indicating an underdamped response. The trajectory shown in red, shows a slower, more critically damped motion, following a more similar motion than the experimental joint trajectory. Despite these differences, both simulated trajectories extend more abruptly than the experimental data. They lack the smooth, gradual rise that characterises biological responses.

To better illustrate the abrupt extension phase in the MuJoCo joint model trajectories, Fig. 5.6A presents the joint trajectory generated with the parameter set marked by the red cross, which better reproduces the smooth passive relaxation observed experimentally. An inset highlights the initial extension phase, emphasising that although the adjusted parameters yield a more gradual relaxation, the onset of motion remains faster than in the biological data. This refined parametrisation therefore improves the qualitative agreement during flexion but does not fully capture the smoothness of the extension phase. Fig. 5.6B

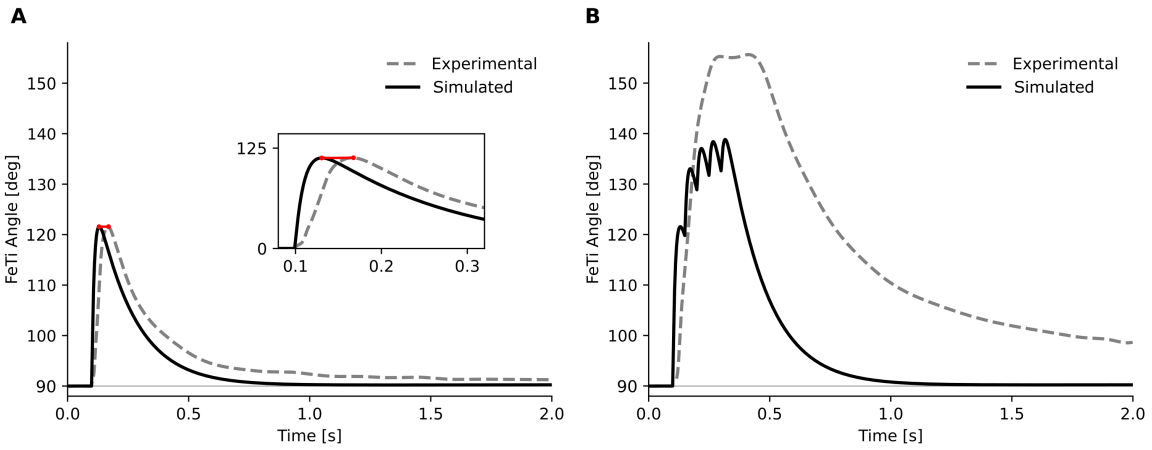

Figure 5.6: Joint trajectories from the physics-based joint model model under single- and multi-spike stimulation. (A) Simulated trajectory using the red-cross parameter set. The inset highlights the abrupt extension phase, the simulated trajectory reaches peak angle faster than the experimental data. (B) Model response to five-spike stimulation at 20 Hz using single-spike calibrated parameters. The model fails to accurately reproduced the experimentally observed joint response.

shows the simulation of the five-spike stimulation at 20 Hz. When the single-spike calibrated parameters are applied to this condition, the model fails to reproduce both regimes accurately. The amplitude and timing of the multi-spike response deviate substantially from the experimental trajectory.

This pattern mirrors what we observed in the nondimensional single-MTU formulation (see Section 5.3.1) and strengthens the hypothesis that an adaptive time scale underlies the response dynamics of the joint. Our interpretation is that the observed changes in relaxation dynamics between single- and multi-spike activation likely arise from adaptations in the muscle activation process itself, where calcium kinetics, cross-bridge dynamics, and excitation-contraction coupling modulate the effective activation time scale. In the current implementation, the abrupt square activation pulse generates a rapid force onset, producing a steep torque rise and an unrealistic sharp extension phase. This contrasts with the gradual and smoother force production characteristic of biological systems [124]. This limitation motivates the introduction of a muscle activation dynamics model incorporating an adaptive time scale, enabling us to test the hypothesis that frequency-dependant adaptations underlie the ability of the joint to reproduce both single- and multi-spike regimes.

5.3.3 Neuromechanical Joint Model

In the previous sections, the single-MTU and physics-based joint models revealed that a fixed time scale in the muscle response could not reproduce both the single- and multi-

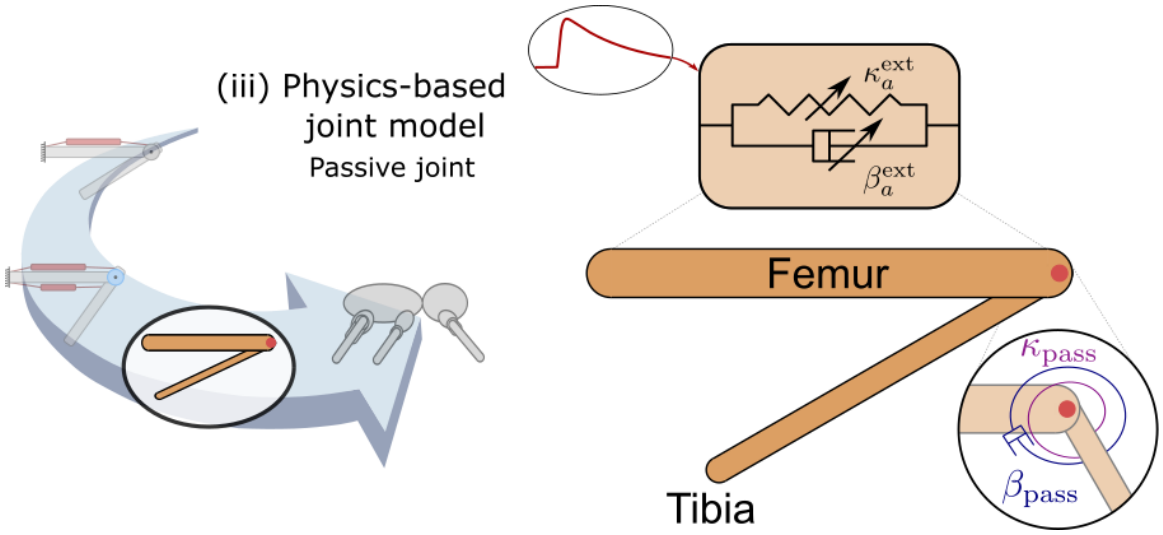

Figure 5.7: The physics-based joint introduced in Section 5.3.2 is complemented with a muscle activation model. This model produces a smoother activation profile to activate the extensor muscle.

spike experiments simultaneously. While the passive joint properties shape the overall motion profile, they alone cannot account for the differences between single- and multi-spike responses. We hypothesised that this discrepancy arises from an adaptive mechanism in the muscle activation dynamics, modulating the relaxation time with stimulation frequency, rather than from variations in the passive mechanical properties of the joint. To test this hypothesis, we extend our previous physics-based joint model into a neuromechanical model that links motor neuron activity to muscle activation, force-torque generation, and joint motion. Fig. 5.7 illustrates the change in the activation dynamics to activate the extensor muscle of the joint, which changes from a square pulse to a smoother rise and decay profile.

In this approach, we model the pathway from the fast extensor tibia (FETi) motor neurone (MN) to the extensor muscle and its resulting torque on the joint. Each electrical spike generated by the FETi MN triggers a transient activation response in the muscle, represented by the activation variable A_m. To describe this process, we choose to model the activation dynamics as the leaky integrator model previously presented in Section 4.8. This formulation captures the temporal filtering of the neural input and the finite time required for excitation–contraction coupling within the muscle fibres. The model is particularly suited to the FETi MN, which has been characterised as a fast, spiking motoneuron responsible for producing rapid, high-amplitude contractions in the locust hind leg [20].

To identify the activation dynamics that best reproduce the experimentally observed single-spike joint response, we perform a parametric sweep between across the parameters τ_s and g_u for a range of values of the activation capacity constant C_a, while keeping the deactivation gain fixed at $g_a = 1$. We constrain C_a to the range $175 - 250$ which yields

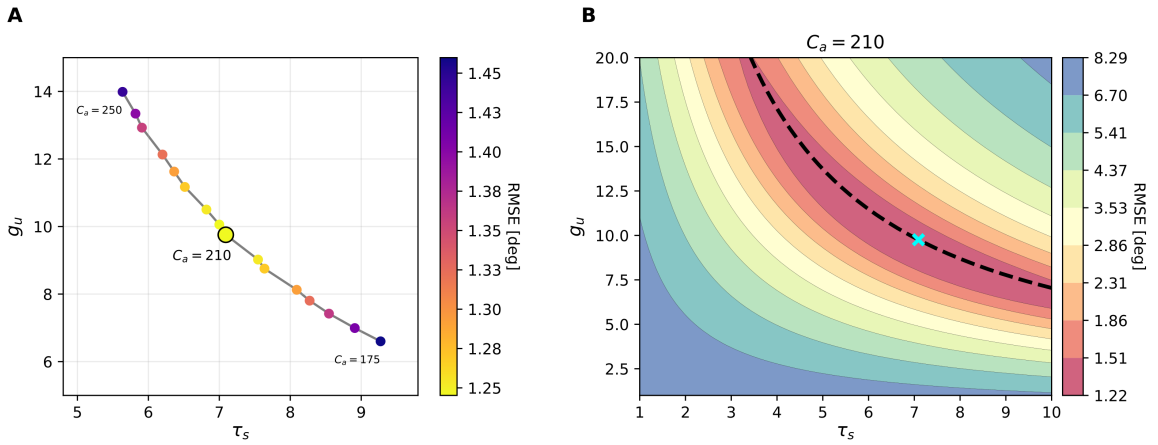

Figure 5.8: RMSE for activation parameter sweeps across different activation capacity values. (A) RMSE as a function of activation time constant τ_s and neural input gain g_u for a range of C_a values. (B) RMSE contour plot for $C_a = 210$, with cyan cross indicating the optimal parameter set that best matches the experimental single-spike joint response.

to twitch relaxation times of $175 - 250\,\text{ms}$, following measurements of half-decay times for the isometric twitch contractions of fast extensor tibiae fibres ($\sim 120\,\text{ms}$) [22]. For each combination of parameters, we compute the RMSE between the experimental and simulated joint angles, using equation 5.1, to quantify the deviation between simulated and observed motion trajectories. This procedure yielded fifteen parameter spaces, each corresponding to a specific C_a value. Fig. 5.8A illustrates the RMSE distribution as a function of τ_s and g_u across the selected C_a values. For each C_a, we identify the combination of τ_s and g_u that minimises the RMSE and then compare these optimal points across all C_a values.

We find the optimal parameter set at $C_a = 210$, $g_a = 1$, $g_u = 9.8$, and $\tau_s = 7.1$. This combination minimised the RMSE to approximately 1.25°, indicating a close agreement between the simulated and experimental joint angles. Fig. 5.8B presents the corresponding RMSE landscape for $C_a = 210$, with the cyan cross marking the optimal parameter combination. The well-defined minimum in this region suggests that the response of the model is sensitive to the balance between the neural input gain and the activation time constant.

Once we identify the optimal parameter values for the muscle activation model, we use them to drive the extensor MTU and systematically vary the passive stiffness and damping of the joint, κ_{pass} and β_{pass}, respectively. For each parameter combination, we quantify the mismatch between the simulated and experimental joint angles by computing the RMSE. Fig. 5.9 presents the RMSE landscape, together with representative joint trajectories corresponding to the parameter sets marked by the red and green crosses in Fig. 5.9A. As before, the black dotted line indicates the combination of κ_{pass} and β_{pass} that yield the same peak angular amplitude as the experimental trajectory. In contrast to the previous

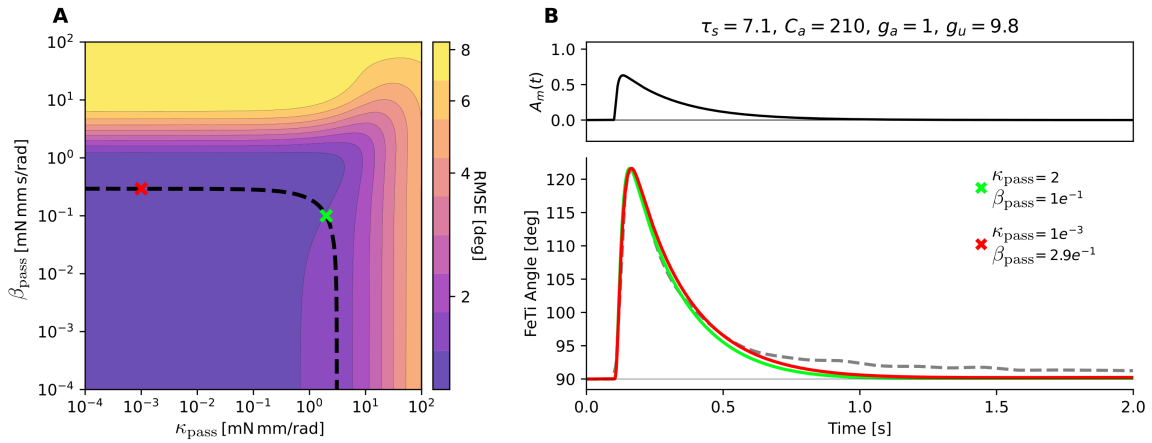

Figure 5.9: RMSE and representative joint trajectories under muscle activation dynamics. (A) RMSE across joint stiffness κ_{pass} and damping β_{pass}, with red and green crosses marking selected parameter sets. (B) Simulated joint trajectories corresponding to the marked parameter sets, illustrating improved agreement with experimental motion under the single-spike activation profile.

analysis, where we activate the MTU with a square pulse, the RMSE values here decrease substantially, indicating that a more physiologically realistic activation profile provides a better match to the experimental joint motion.

Activating the extensor MTU with this smoother activation profile eliminates the abrupt extension phase observed in Fig 5.6A. The gradual rise in activation results in a correspondingly smoother extension, more consistent with the experimental data. Similar to before, high κ_{pass} values, regardless β_{pass}, lead to high RMSE values due to reduced peak angular amplitude of the joint angles. As β_{pass} increases, the response becomes progressively damped, eventually resulting in negligible extension. On the other hand, the lowest RMSE values occur when both κ_{pass} and β_{pass} are below 1. Within this region, the joint exhibits larger extensions and smooth relaxation phases that closely resemble the experimental data, suggesting that multiple combinations of joint passive stiffness and damping can generate similarly realistic joint responses.

We find that the passive stiffness-damping combinations producing the same peak amplitude (represented as the black dotted line in Fig. 5.9A) follow a similar pattern to that discussed in Section 5.3.2. The same dynamic regimes emerge across the parameter space: within the range of $10^{-4} \leq \kappa_{\text{pass}} \leq 10^{0}$, the joint motion amplitude remains largely unaffected by changes in stiffness, and thus, damping dominates the dynamics. Beyond $\kappa_{\text{pass}} \approx 1$, the behaviour becomes primarily stiffness-driven, and further increases in damping have little influence on the resulting motion. Interestingly, this transition occurs at a lower stiffness value in the current neuromechanical model compared with the previous one. As reported before, the transition occurs beyond $\kappa_{\text{pass}} \approx 10$ while here, it occurs

Neuromechanical Joint Model Parameters	
Parameter	**Value**
η_a^{ext}	66
κ_{pass}	0.001
β_{pass}	0.29
τ_s	7.1
C_a	210
g_a	1
g_u	9.8

Table 5.3: Neuromechanical joint model parameters for single-spike experiment.

around $\kappa_{\text{pass}} \approx 1$. This earlier transition likely results from the smoother activation profile introduced by the activation dynamics, which reduces the abrupt force onset observed with the square pulse. Consequently, the system reaches the stiffness-dominated regime at lower passive stiffness values, as the overall torque-angle relationship becomes more sensitive to changes in κ_{pass}.

Fig. 5.9B shows two representative trajectories corresponding to parameter sets marked with red and green crosses in Fig. 5.9A. Both parameter combinations produce the peak amplitudes consistent with the experimental data and display qualitatively similar trajectories. However, the motion generated with values of $\kappa_{\text{pass}} = 2.0$, $\beta_{\text{pass}} = 0.1$ (green cross) exhibit slightly faster extension and flexion phases than the trajectory with $\kappa_{\text{pass}} = 0.001$, $\beta_{\text{pass}} = 0.29$ (red cross). This behaviour arises from the increased joint stiffness in the former case, which enables faster energy storage and release, while the lower damping allows quicker decay. In contrast, higher damping in the red-cross configuration dissipate energy more rapidly, resulting in a slower return to the resting position. Nonetheless, both trajectories fall within the variability of the experimental data [3], suggesting that biological systems can achieve similar joint kinematics through different combinations of passive stiffness and damping. For subsequent analysis in this section, we adopt $\kappa_{\text{pass}} = 0.001$, $\beta_{\text{pass}} = 0.29$, as this parameter set yields the lowest RMSE. We summarise the models parameters in the Table 5.3.

The resulting stiffness and damping coefficients κ_{pass} and β_{pass} represent physically interpretable quantities, corresponding to the joint's rotational spring and viscous resistance. We use the estimated stiffness and damping coefficients to calculate the dimensionless parameters η_{pass}, μ_j, γ, and $\hat{J}$. The corresponding values are summarised in Table 5.4.

Each of these dimensionless values compresses a ratio of physical effects into a single scalar and therefore directly indicates the relative magnitude of competing contributions

Dimensionless Parameters		
Parameter	**Definition**	**Value**
η_{pass}	$\frac{\kappa_{\text{pass}}}{\beta_{\text{pass}}}\,\tau$	0.003
μ_j	$\frac{\beta^{\text{ext}}_{\text{max}}(L^{\text{ext}}_0)^2}{\beta_{\text{pass}}}$	29
γ	$\frac{mgl}{2\beta_{\text{pass}}}\,\tau$	6
$\hat{J}$	$\frac{J}{\beta_{\text{pass}}\,\tau}$	0.01

Table 5.4: Dimensionless parameters estimated from the passive joint stiffness κ_{pass} and damping β_{pass} obtained from the physics-based joint model.

to joint torque. The small value of the stiffness-to–damping ratio η_{pass} indicates that, on the chosen timescale $\tau = 1\,\text{s}$, elastic restoring forces are negligible compared with viscous dissipation. In other words, the passive return of the joint will be dominated by viscous damping rather than elastic recoil, thus an underdamped oscillatory response is not expected in this parameter regime.

The parameter μ_j measures the relative influence of the muscle-generated torque on the overall net torque balance. A value of $\mu_j \gg 1$ indicates that the torque generated by the extensor MTU is mechanically amplified, such that the MTU exerts a dominant influence on the joint rotational dynamics during activation. In this regime, small variations in muscle activation produce comparatively large changes in joint torque, while the passive joint torques act primarily to counterbalance and stabilise the motion.

The computed value of γ is of order unity and therefore indicates that gravity is not negligible on the timescale τ. Although the absolute gravitational torque is small in base units terms, when evaluated on the scale of viscous torques, its contribution to the net torque balance is non-negligible and, hence, influences the tibia's post-relaxation equilibrium angle. Importantly, this does not imply gravity drives rapid motion; rather, as viscous dissipation slows dynamics, even a small persistent gravitational bias shifts the long-time equilibrium and must be included to predict the rest angle correctly.

Finally, the small value of the dimensionless inertia $\hat{J}$ indicates an overdamped regime in which inertial terms are negligible on the timescale τ. Practically, this means that the angular acceleration of the joint contributes little to the observed relaxation profile; motion is dominated by viscous decay rather than inertial dynamics. This supports the use of viscous-dominated approximations when analysing the relaxation phase and explains

why adding explicit inertia to the single-MTU model is unlikely to change the qualitative relaxation behaviour.

The dimensionless values provide a compact quantitative characterisation of the simulated joint. The system is strongly viscous-dominated, with a non-negligible gravitational bias and greater dissipative capacity in the muscle–tendon complex than in the joint tissues. Because each nondimensional number arises directly from measured or fitted mechanical parameters, these values also provide a consistent basis for comparing parameter regimes across animals or for scaling to bio-inspired mechanical designs.

Building upon the analysis of the dynamics of the muscle activation and the joint response under the single-spike condition, we extend our analysis to the multi-spike condition. To do this, we introduce an adaptive deactivation dynamics in the muscle activation model to reproduce the slower relaxation observed experimentally after repeated stimulation. In this formulation, the deactivation gain g_a evolves as a sigmoid function of the instantaneous muscle activation level A_m (see Section 4.8 for details). Thus, the deactivation constant becomes dependant on the muscle activity, $\tau_a(A_m)$. The parameter g_a is updated only during the rising phase of activation, while the muscle is being excited by neural input, and remains constant during relaxation. This conditional update produces a hysteresis-like behaviour: once the muscle reaches a high activation state, g_a remains at a reduced value even as activation decays. Consequently, the relaxation phase becomes slower than the initial activation phase, generating an asymmetric temporal response that aligns with experimental recordings of multi-spike muscle twitches. The magnitude of this adaptive decay depends on both the peak activation reached and the steepness of the sigmoid function controlling $g_a(A_m)$ (see equation 4.21).

We implement the activation-dependant time constant, $\tau_a(A_m)$, to capture the slowing of muscle passive relaxation observed under repeated stimulation at high frequencies. Fig. 5.10 illustrates this mechanism for the single-spike and five spikes at 20 Hz conditions. Fig. 5.10A shows the muscle activation A_m as a function of the deactivation gain g_a. Under the single-spike condition, the deactivation gain $g_a(A_m)$ remains close to its initial value of 1 (see red dot in the left panel) and yields a deactivation constant of $\tau_a = C_a/1$. For the multi-spike condition, on the other hand, $g_a(A_m)$ decreases to approximately 0.3 (see the blue dot in the right panel), effectively extending the deactivation time constant to $\tau_a = C_a/0.3$. This reduction in g_a produces a slower passive relaxation of the tibial, enabling the model to better reproduce the experimentally observed relaxation phase.

Fig. 5.10B shows the corresponding muscle activation profiles driving the extensor MTU for both simulation regimes, highlighting the slower decay and sustained activation that follows repeated input. Finally, we compare the simulated and experimental joint angles in Fig. 5.10C. The inclusion of the adaptive time constant produces a qualitatively match

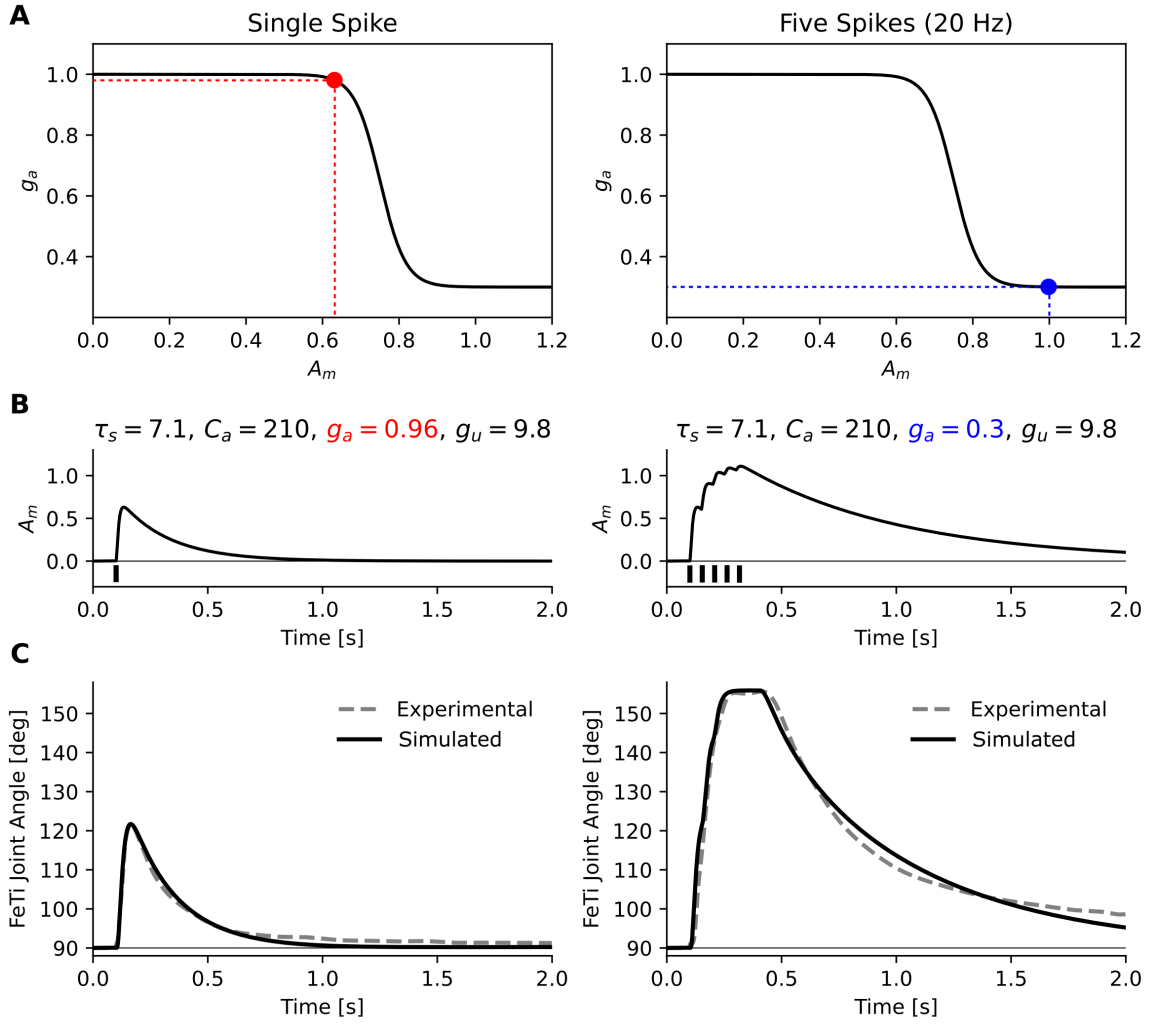

Figure 5.10: Effect of adaptive time constant on muscle activation and joint dynamics under single- and multi-spike stimulation. (A) Deactivation gain $g_a(A_m)$ as a function of muscle activation A_m, shown for single-spike (left) and five-spike at 20 Hz (right) conditions. Red and blue dots indicate the resulting g_a values, which modulate the deactivation time constant τ_a. (B) Muscle activation profiles driving the extensor MTU under both stimulation regimes, highlighting the slower decay and sustained activation following repeated input. (C) Comparison of simulated and experimental joint angles, showing that the inclusion of the adaptive time constant enables the model to reproduce the sustained extension plateau observed experimentally under high-frequency stimulation.

to the experimental traces. Particularly, the model is able to reproduce the sustained plateau that characterises the five-spikes at 20 Hz condition after the cessation of electrical stimulation. To better compare the simulated and experimental joint angles, we present in Table 5.5 the same evaluation metrics applied in Section 5.3.1. This provides a consistent basis for assessing the improvement achieved with the neuromechanical model and the adaptive time constant.

	Single Spike		5@20 Hz	
Metrics	$\theta_{\mathbf{peak}}$ [°]	τ_{relax} [s]	$\theta_{\mathbf{peak}}$ [°]	τ_{relax} [s]
Simulated	121.71	0.2190	155.9	0.4980
Experimental	121.62	0.1841	155.66	0.3825
Error	0.074%	18.95%	0.15%	30.19%

Table 5.5: Comparison of simulated and experimental joint angle metrics under single-spike and five-spikes at 20 Hz stimulation conditions for neuromechanical joint model with adaptive time scale.

From these metrics, we observe a decrease in the error of the joint peak angle reached under both the single-spike and five-spike (20 Hz) conditions compared with the values obtained from the neuromechanical model in Section 5.3.1 (see Table 5.2). This decrement indicates that the physics-based joint model, which includes the adaptive muscle activation dynamics, more accurately reproduces the angular displacement during the extension phase. However, we find a corresponding increase in the error for the relaxation time constant, τ_{relax}. The higher error in this model does not reflect a poorer biological fit, but a mismatch between the metric and the model. As mentioned in Section 5.3.1, the metric τ_{relax} is defined as the time to decay $1/e$ of the peak angle. This measure is suited to the single-MTU model because that model produces a simple exponential relaxation governed by a single stiffness-to-damping ratio. In the neuromechanical model, however, the relaxation phase emerges from the interaction of joint inertia, gravitational modelling, and joint compliance from MuJoCo, as well as the added activation dynamics. Therefore, this relaxation phase does not follow a simple exponential and applying a single-exponential metric to this signal inflates the apparent error without indicating worse representation of the biology. We interpret the higher τ_{relax} error as a metric artefact arising from the increased physiological detail of the neuromechanical model, not as evidence against the adaptive activation hypothesis. The interpretation is supported by the improved peak angle accuracy (see Table 5.5) and by the qualitatively agreement of the simulated trajectory with the experimental sustained plateau, neither of which is captured by the τ_{relax} metric alone.

Overall, these results demonstrate that both the single-MTU and physics-based formulations are capable of reproducing the characteristic extension–flexion cycles of the locust hind leg. The inclusion of adaptive activation dynamics allows the model to replicate joint trajectories across stimulation frequencies within a unified neuromechanical framework. Importantly, the differences observed between models in the relaxation metrics arise not from inconsistencies but from their level of mechanical realism. In the MuJoCo framework, the relaxation phase emerges from the interaction of multiple physical processes rather than a single exponential decay. These findings therefore provide a coherent foundation for interpreting how active and passive mechanisms cooperate to shape joint motion, and will be

discussed in the following chapter.

5.4 Discussion

In this chapter, we examined how active muscle forces and passive joint mechanics interact to generate the characteristic extension–flexion cycles of the locust hind leg. Using three complementary modelling approaches, the single-MTU model, the physics-based model, and the neuromechanical model linking neural input to muscle activation, we tested whether a simplified system could reproduce the dynamics reported experimentally by Ache and Matheson. All modelling frameworks were able to generate realistic joint trajectories. However, neither model with fixed activation dynamics could simultaneously reproduce the single- and multi-spike responses, revealing the need for an adaptive time scale in the muscle activation process. Introducing this adaptive mechanism allowed the neuromechanical model to capture both the rapid, transient response to a single stimulus and the sustained plateau and slower relaxation decay following repeated stimulation.

Our model frameworks demonstrated that complete extension-flexion cycles can emerge from the interplay between active muscle forces and passive viscoelastic elements. Specifically, active extensor MTU contraction drives the extension phase, while passive viscoelastic forces alone are sufficient to return the joint to its resting position during the flexion phase, even in the absence of any active flexor muscle activity. These passive properties, represented by the dimensionless ratios η_p^{ext} and η_{pass}, independently determine the temporal structure of joint motion. The joint exhibits faster passive movements when its passive elements are stiffer than viscous ($\eta_p^{\text{ext}} > 1$ and $\eta_{\text{pass}} > 1$). In contrast, it shows slower passive motion when the elements are more viscous than stiff ($\eta_p^{\text{ext}} < 1$ and $\eta_{\text{pass}} < 1$). We observed this behaviour consistently across both the single-MTU and physics-based joint models. However, our findings indicate that these passive joint properties alone cannot fully account for joint behaviour under varying stimulation conditions. Passive components establish the baseline mechanical resistance and return trajectory, while active muscle dynamics shape how energy is stored and released throughout activation cycles. This interplay between active and passive contributions maintains mechanical stability and enables graded, context-dependent motion. In biological systems, such coupling allows joints to remain both responsive and stable across a broad range of activation frequencies, consistent with the efficient control observed in insect limb movements.

To reproduce the experimentally observed joint behaviour under single and multiple stimulation, we incorporated a muscle activation model with an adaptive time constant $\tau_a(A_m)$, into our joint framework. While the response to a single spike remains approximated linear, multiple pulse summation introduces non-linear effects [124]. Therefore, a

fixed time constant cannot account for this behaviour, necessitating an adaptive mechanism. During repeated stimulation, calcium ions accumulate in the sarcoplasm due to incomplete reuptake, prolonging cross-bridge binding and slowing muscle tension decay. This effect increases the activation time constant. In addition, multi-spike responses exhibit a transient plateau that maintains tibial extension before passive return. Biologically, this reflects calcium binding to troponin, which is a saturable process limited by available binding sites [124]. Similarly, viscoelastic adaptations in the muscle–tendon unit, such as changes in muscle stiffness or apodeme tension, may further contribute to mechanical delays.

Thus, the inclusion of an adaptive time scale into our model should not be viewed as arising from a single mechanism but rather as an emergent property of coupled biochemical and mechanical processes. Our model captures a key physiological principle: insect muscles modulate response dynamics based on recent activity [27, 52], enabling a single motor neuron to generate both twitch-like and sustained movements without altering neural input.

Comparing the single-MTU and physics-based frameworks reveals complementary insights into joint mechanics. The single-MTU model simplifies the system by condensing multiple physical effects into a few dimensionless ratios, making it effective for identifying dominant forces and scaling relationships across conditions. In contrast, the physics-based model explicitly incorporates physical geometry, inertia, and contact forces, allowing direct interpretation of stiffness and damping in physiological units. By transitioning to this physics-based implementation, we reassigned the passive elements from the extensor MTU to the joint itself. This change reflects both biological reasoning (since passive resistance and elasticity are largely associated with joint structures) and practical modelling considerations, as it allows clearer separation between active muscle dynamics and joint-level passive mechanics.

A further consideration concerns the suitability of the τ_{relax} metric for comparing models at different levels of detail. As indicated in Section 5.3.3, this metric is well-suited to systems that produce a simple exponential relaxation, but becomes an incomplete descriptor when relaxation emerges from multiple interacting processes. A more appropriate evaluation of the relaxation phase of the neuromechanical model would involve either fitting a multi-exponential decay to the simulated trajectory, or computing the RMSE over the full relaxation phase rather than extracting a single constant. Either approach would better capture the neuromechanical model's temporal structure of the relaxation phase and provide a more informative basis for model comparison.

While the single-MTU model prioritises conceptual clarity and analytical tractability, the physics-based framework captures emergent behaviours, such as interactions among gravity, inertia, and passive viscoelasticity, that are difficult to express in nondimensional terms. Despite methodological differences, both models converge on the same qualitative

conclusion: joint motion arises from the coupling of active and passive processes, and adaptive activation dynamics are essential to reproduce the full spectrum of observed behaviours. Together, these approaches demonstrate that integrating reduced-order and physics-based models offers a powerful strategy for understanding how complex motor behaviours emerge from simple neuromechanical principles.

Our findings show insights into how insects achieve stable and efficient limb control. The ability of a single MN to generate both rapid and sustained joint movements suggests that control complexity resides primarily in the muscle–joint mechanics rather than in neural commands. The adaptive activation dynamics identified in our models provide an intrinsic mechanism for context-dependent modulation: at low activation levels, the system behaves as a fast, responsive actuator, while sustained activity produces slower, smoother motion. This mechanical adaptability allows simple spike timing to generate a diverse repertoire of joint behaviours. Self-regulating muscle–joint systems exemplify how neuromechanical coupling enhances energy efficiency and robustness, particularly at the small scales and high-frequency regimes typical of insect locomotion.

Beyond biological relevance, these principles have direct applications in bio-inspired robotics and neuromechanical modelling. Our simplified joint system shows that realistic limb kinematics can emerge from simple active and passive components. Embedding activation-dependent damping or passive stiffness in robotic joints could enable regulated transitions between fast, efficient movements and slow, stable postural control. Furthermore, estimating physically interpretable stiffness and damping parameters from MuJoCo simulations facilitates the transfer of biologically grounded properties into mechanical systems. The combined use of nondimensional and physics-based models establishes a scalable framework: nondimensional models reveal governing relationships and control regimes, while physics-based simulations translate these principles into realistic mechanical implementations. Both frameworks offer a pathway toward adaptive robotic systems that exploit the intrinsic dynamics of their materials and structures.

In the next chapter, we extend the modelling framework to include a pair of antagonistic muscles and explore the role of muscle asymmetry when combined with passive elements in the joint.

Chapter 6

Single Joint with a Pair of Antagonistic Muscles

6.1 Overview

In the previous chapter, we showed that realistic insect joint dynamics can emerge from the coupling between muscle dynamics and passive joint viscoelasticity, and that adaptive activation time scales are essential to reproduce both twitch-like and sustained responses under different stimulation conditions. To demonstrate this, we employed the first level of the modelling hierarchy: a nondimensional joint model driven by a single muscle–tendon unit (MTU), which effectively represented the net action of an antagonistic muscle pair acting on a rigid joint (see Section 4.3 for details). This level of the hierarchy was also evaluated within a physics-based simulation environment to account for more realistic mechanical effects.

Building on these results, we extend the nondimensional joint framework to the second level of the modelling hierarchy, in which two explicit antagonistic MTUs actuate a viscoelastic joint (refer to Section 4.4 for details). This extension allows us to examine how active and passive mechanisms interact within two key anatomical features of biological joints. First, the nearly universal use of antagonistic muscle pairs for joint control; and second, the inherent asymmetry between these muscles, particularly in their force production capabilities. We use this model as a controlled testbed to validate the generality of the nondimensional formulation and to systematically explore how key dimensionless parameters govern joint behaviour. Specifically, we investigate how passive joint mechanics shape force balance, stability, and movement regimes in antagonistically actuated systems, thereby clarifying the role of passive elements in organising joint-level dynamics beyond the

single-MTU case.

In biological systems, the coordinated action of antagonistic muscle pairs is central to joint control. Their properties are highly optimised to achieve the desired joint control behaviour. However, as discussed in previous chapters, joint output is not determined by muscle action alone. Passive elements of the joint such as tendons, ligaments, connective tissues, and other viscoelastic elements significantly modulate the joint output. Interactions between antagonistic muscles and passive elements influence force transmission, enable the storage and release of elastic energy, and ultimately shape the net torque produced at the joint. In addition, antagonistic muscle pairs often posses unequal strength. The agonist muscle is typically larger and more powerful, enabling it to generate the substantial forces required for load-bearing or gravity-resisting tasks. In contrast, the antagonist often provides fine control and joint stabilisation [120]. This functional asymmetry is seen as an evolved strategy for achieving efficient and versatile joint control across diverse behavioural contexts.

In this chapter, we aim to understand how muscle asymmetry and integrated passive joint structures act together to shape joint dynamics, and to identify the benefits and limitations these anatomical and mechanical strategies for the design of bioinspired joints. To this end, the chapter is organised as follows. Section 6.2.1 establishes a baseline of the nondimensional antagonistic-MTU joint model by characterising passive joint dynamics in the absence of active muscle actuation. Section 6.2.2 then explores the interaction between symmetric active muscle input and passive joint properties, focusing on the dynamic range and frequency response of the joint. Section 6.2.3 investigates how asymmetry in antagonistic muscle strength alters joint behaviour, and explores the role of passive elements under asymmetric actuation. Finally, Section 6.3 discusses the results obtained here. Fig. 6.1 illustrates the level of modelling hierarchy used in this chapter.

6.2 Results

6.2.1 Passive Dynamics

This section characterises the passive dynamics of the nondimensional antagonistic-MTU joint model in the absence of muscle activation. This establishes a baseline against which the effects of antagonistic MTU input can later be evaluated. By isolating the passive joint response, we ask how joint viscoelasticity alone governs the form and time scale of passive joint motion.

To this end, the distal link of the joint, *i.e.* the tibia, is initially deviated to an extended

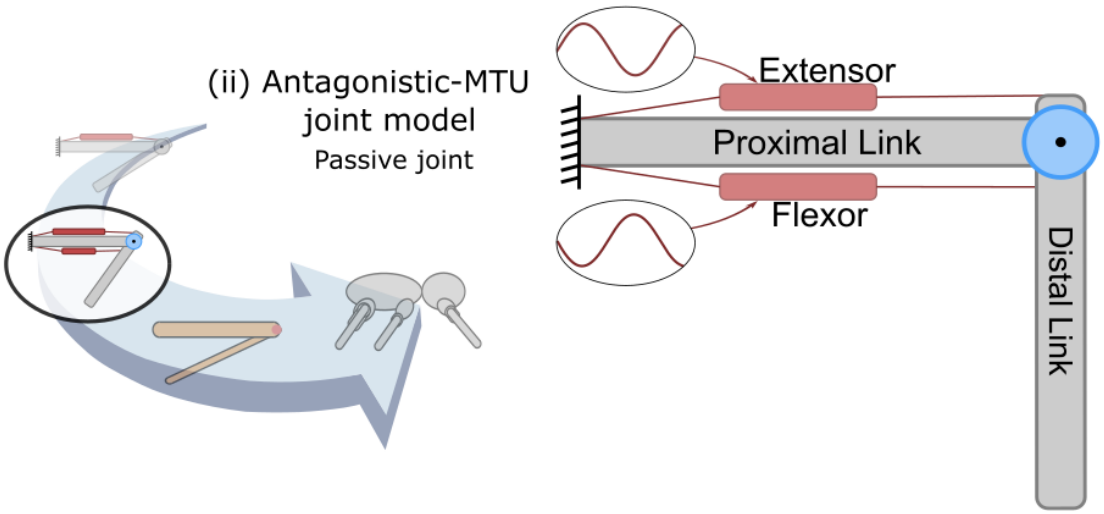

Figure 6.1: Throughout this chapter, we adopt the second level of the modelling hierarchy, the antagonistic-MTU joint model. This model includes a pair of antagonistic MTUs, the extensor and flexor, to drive tibial (distal link) motion. The two muscles are driven by sinusoidal activations in anti-phase. In contrast to the single-MTU model (section 4.3, passive viscoelasticity is assigned to the joint itself in this formulation.

angle $\theta_{\text{dev}} = 140°$, and subsequently released to allow the joint to flex entirely passively towards its resting state $\theta_{\text{rest}} = 90°$. To characterise the relaxation dynamics, we define the relaxation time τ_{relax} as the time needed for the joint angle to decay to $1/e$ of its initial deviation. We adopt this decay criterion as it provides a consistent, amplitude-independent measure of the dominant time scale in both overdamped and underdamped viscoelastic systems. This is appropriate in these simulations because the distal link behaves effectively as a damped pendulum, and therefore can exhibit either response regime depending on parameter values.

Fig. 6.2 illustrates the results of these simulations. It shows a parameter sweep of the passive joint dynamics within the nondimensional framework. The results are presented as contour plots of the relaxation time τ_{relax} evaluated across combinations of the passive joint stiffness-to-damping ratio η_j and the nondimensional moment of inertia $\hat{J}$. Fig. 6.2C-D correspond to different values of the gravitational-to-viscous force ratio γ. Additionally, Fig. 6.2A illustrates a representative overdamped relaxation of the joint angle θ, with the orange marker indicating the time at which the angular deviation has decayed to θ_{dev}/e of its initial magnitude.

These contour plots reveal different behavioural regimes. When both η_j and $\hat{J}$ are low, the joint returns to equilibrium slowly and monotonically, with overdamped responses and relaxation dominated by damping effects (bottom-left corner in Fig 6.2B). In contrast, large values of η_j and $\hat{J}$ lead to underdamped dynamics and oscillatory settling (top-right corner

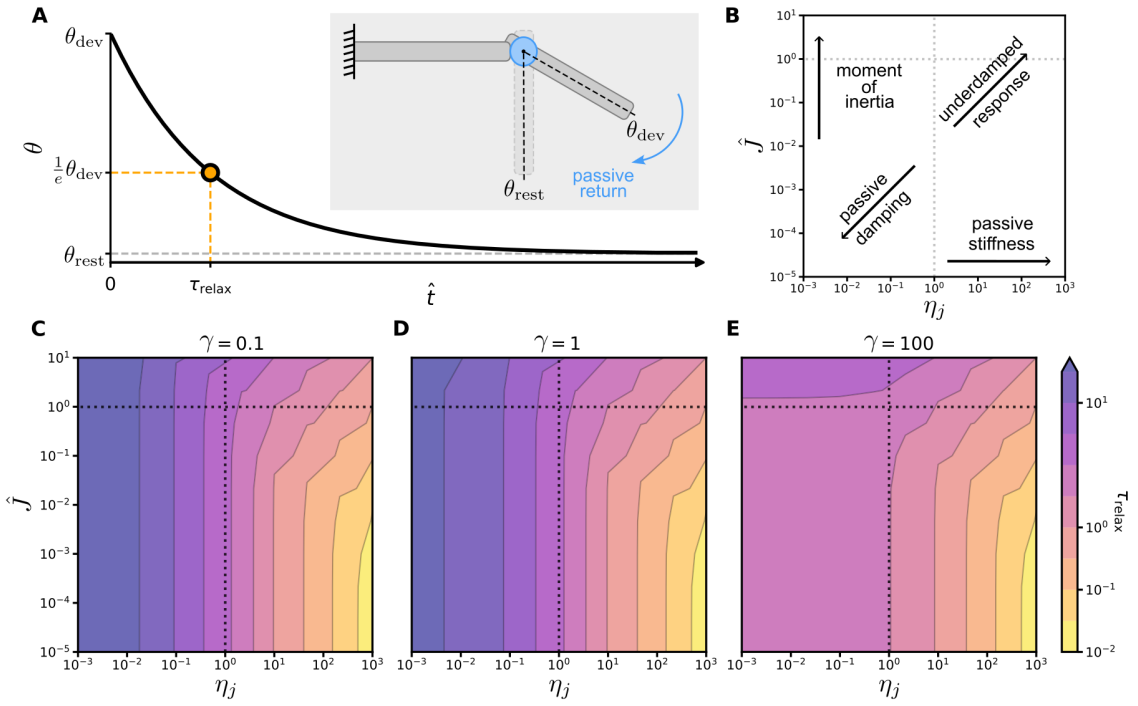

Figure 6.2: Passive joint dynamics. (A) An overdamped relaxation trajectory of the joint angle $\theta(\hat{t}\,)$. Orange marker denotes the time point at which the joint angle has decayed to θ_{dev}/e of its initial deviation. The inset indicates the distal link returning passively from the deviation angle θ_{dev} to the resting position θ_{rest}. (B) Schematic of the parameter space spanned by the passive stiffness-to-damping ratio η_j and the dimensionless moment of inertia $\hat{J}$. The upward arrow indicates increasing inertia, while the horizontal arrow denotes increasing passive stiffness. The lower-left region is dominated by passive damping, whereas the upper-right corner reflects an underdamped response. (C-E) Dimensionless relaxation time τ_{relax} as a function of the variables η_j and $\hat{J}$ for $\gamma = 0.1$, $\gamma = 1$, and $\gamma = 100$, respectively. Blue-tone colours indicate longer relaxation times (*i.e.*, slower returns), while yellow-tone colours denote faster convergence to the resting state. Dashed lines indicate where $\eta_j = 1$, and $\hat{J} = 1$.

in Fig 6.2B). In this regime, increased stiffness and inertia produce faster transient responses, but at the cost of reduced stability and greater control demands. Overall, increasing η_j, corresponding to stiffer behaviours relative to viscous dissipation, generally reduces the relaxation time τ_{relax} and accelerates the passive return to equilibrium. Consequently, when $\hat{J}$ is small the effect of inertia is negligible, and the relaxation time is nearly entirely governed by passive viscoelastic properties of the system.

Interpreting the contour plots further reveals how the nondimensional parameters interact to shape passive joint dynamics. Variations in the gravitational-to-viscous force ratio γ shift these contours across the parameter space. Larger values of γ strengthen the gravitational restoring torque, thus accelerating passive returns over much of the plane and,

in regions of substantial inertia, further amplifying transient oscillations by increasing the mechanical energy available for overshoot. These results highlight a trade-off in the nondimensional design space: passive tuning can favour either stability or speed. Achieving rapid yet well-damped passive responses therefore requires increasing η_j while maintaining $\hat{J}$ and γ within ranges that avoid excessive inertial overshoot.

Although these simulations focus on passive flexion following an initial extension, identical behaviour arise when the direction of the perturbation is reversed. Fig. 6.3 presents the corresponding contour plots for passive extension, in which the tibia is initially displaced to a flexed configuration $\theta_{\text{dev}} = 40°$, and then released, allowing the joint to extend passively toward its resting position $\theta_{\text{rest}} = 90°$. The close agreement between the flexion and extension cases confirms that the passive joint response is directionally symmetric and governed by the same nondimensional viscoelastic parameters.

Having established how passive viscoelastic properties alone shape joint relaxation dynamics, we turn to the role of active muscle actuation and examine how it interacts with passive joint mechanics during rhythmic movement in a symmetric actuation configuration.

6.2.2 Symmetric Antagonistic Actuation

A central question of this chapter is how active muscle dynamics interacts with joint passive properties to determine its dynamic range and frequency response. While a range of performance metrics could be considered, such as energy efficiency, force control precision, and robustness to external disturbances, we focus here on the peak-to-peak joint excursion θ_{p2p}. This measure provides a basic observable and functionally relevant characterisation of joint performance under periodic actuation.

Joint behaviour is examined under a symmetric antagonistic muscle configuration, $\mu_m = 1$, which serves as a reference case for assessing the influence of passive joint properties under balanced flexor–extensor actuation. Fig. 6.4 illustrates the results of this symmetric condition. Here, the distal link is driven by alternating sinusoidal activations A_m^{fl} and A_m^{ext} of the flexor and extensor MTUs, respectively. These activations produce periodic oscillations about the resting joint angle θ_{rest}. The resulting joint motion is analysed as a function of the active stiffness-to-damping ratio η_a, the passive stiffness-to-damping ratio η_j, and the activation frequency $\hat{f} \equiv 1/\hat{t}$. To facilitate visualisation and interpretation of the results in two-dimensional parameter sweeps, we fix the gravitational and inertial parameters to $\gamma = 1$ and $\hat{J} = 0.1$ throughout this Section. These values are chosen as representative reference points, placing the system in a regime where neither gravitational loading nor inertia dominates the joint dynamics, rather than as estimates specific to a particular joint (such as those shown in Table 5.4, corresponding to the locust FeTi joint).

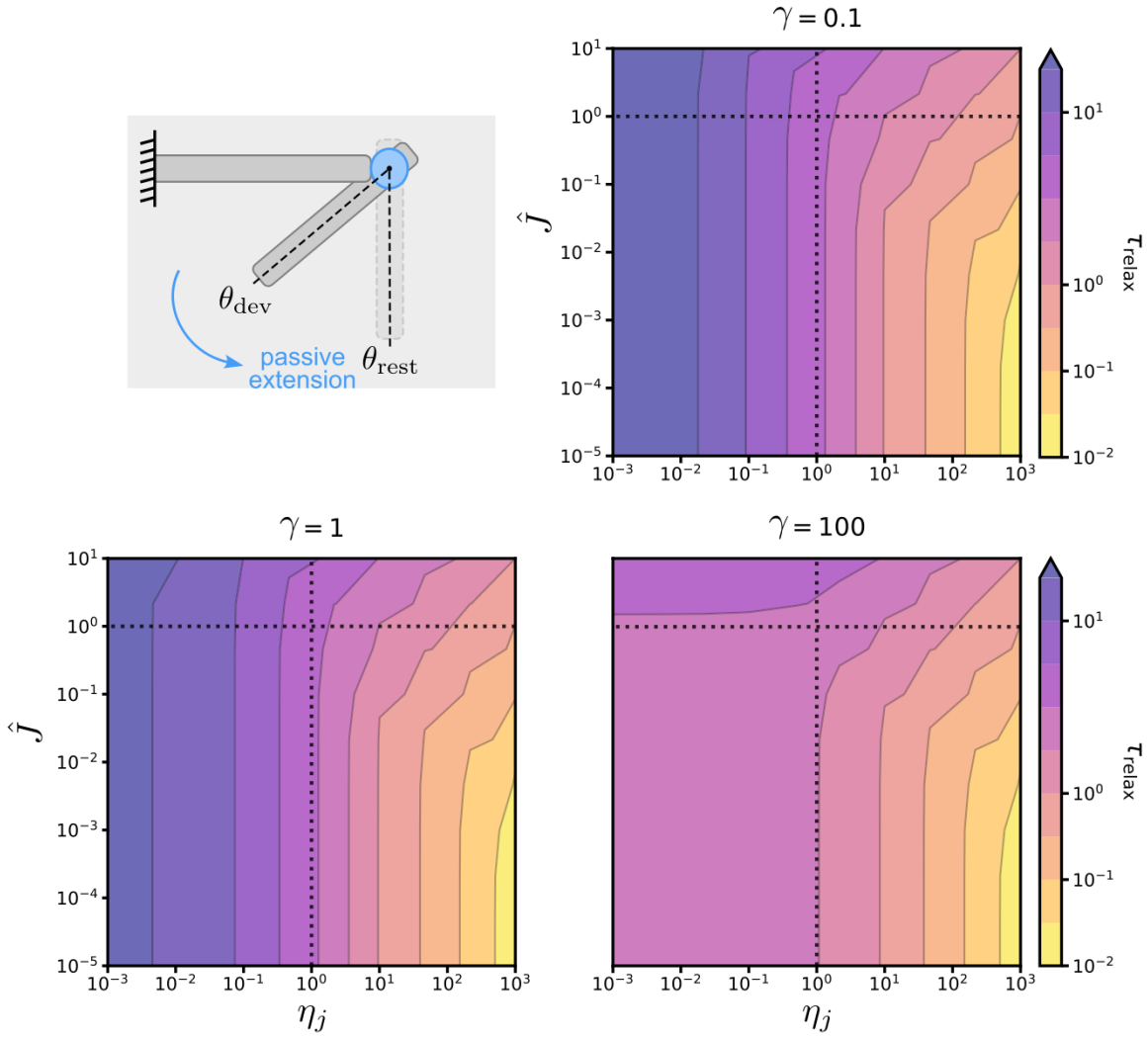

Figure 6.3: Passive extension dynamics. Contour plots are identical to those shown in Fig. 6.2 and are reproduced here for completeness. The joint schematic illustrates the passive extension configuration, with the tibia initially displaced to a flexed angle and released to extend passively toward the resting position, highlighting the reversed direction of joint motion relative to the passive flexion case. Dashed lines indicate where $\eta_j = 1$, and $\hat{J} = 1$.

On the one hand, Fig. 6.4B illustrates how the interplay between active muscle properties, quantified by η_a, and passive joint mechanics, quantified by η_j, shapes the dynamic range of the joint. On the other hand, Fig. 6.4C presents an analogous interplay between η_a and the dimensionless activation frequency $\hat{f}$. Notably, in both parameter spaces, the joint dynamics organise into three qualitatively distinct dynamic regimes.

In regime I, the dynamic range depends almost entirely on η_a. This regime arises either when the passive stiffness is insufficient (Fig. 6.4B), or when activation frequency is suffi-

ciently low (Fig. 6.4C), such that passive resistance does not significantly constrain motion. In other words, the peak-to-peak amplitude θ_{p2p} is dominated by the active properties of the MTUs, indicating that muscle activation directly sets the joint movement.

Regime II reflects a balanced interaction between active and passive elements. In this regime, joint motion is governed by a trade-off between η_a and η_j (Fig. 6.4B), or between η_a and $\hat{f}$ (Fig. 6.4C), giving rise to diagonally oriented contour lines (see the solid black diagonal lines marking Regime II in Fig. 6.4B-C). This structure indicates that maintaining a given joint amplitude requires proportional increases in active muscle stiffness as either passive stiffness or activation frequency increases. Note that in the limiting case of high active stiffness combined with low passive damping, joint behaviour approaches that of an ideal rigid joint (see dotted square on Fig. 6.4B), consistent with an approximate behaviour captured by the first level of the modelling hierarchy (the single-MTU joint model).

In regime III, passive resistance dominates joint behaviour. When passive stiffness or activation frequency becomes sufficiently large, joint motion is strongly attenuated and the dynamics range collapses. Here, the joint exhibits minimal oscillatory motion and behaves effectively as a quasi-static system, despite ongoing muscle activation.

Additionally, the interaction between the passive properties of the joint η_j and the activation frequency $\hat{f}$ is illustrated in Fig. 6.4D. This interaction reveals two distinct response regimes (delineated by a solid black line). Below this boundary, joint behaviour is dominated by passive stiffness. As η_j increases, passive resistance increasingly limits the ability of the MTUs to bend the joint. Hence, the range of motion of the joint diminishes. Above the boundary, the limiting factor translates to the activation dynamics, such that increasing activation frequency becomes less effective at generating large joint excursions, again leading to reduced amplitudes.

In regions where both η_j and $\hat{f}$ remain below one, the joint amplitude is only weakly affected by variations in these parameters, and is instead determined primarily by the active properties of the MTUs. Conversely, when η_j and $\hat{f}$ exceed one, maintaining a given amplitude requires a coordinated balance between passive stiffness and activation frequency. Therefore, this regime indicates how passive joint mechanics and neural activation timing jointly constrain the achievable dynamic range of motion.

It is important to mention that the contour plots in Fig. 6.4 are obtained with a fixed value of the dimensionless active-to-passive ratio $\mu_c = 1$, which implies that the active MTU torques and passive joint torques contribute comparably to the net joint dynamics (see Eq. 4.14 for details). Varying μ_c reveals how the relative weighting between active and passive contributions reshapes the dynamic range of the joint. Fig. 6.5 shows contour plots of the peak-to-peak amplitude for values of $\mu_c = 0.5$ (Fig. 6.5B), $\mu_c = 5$ (Fig. 6.5A), and

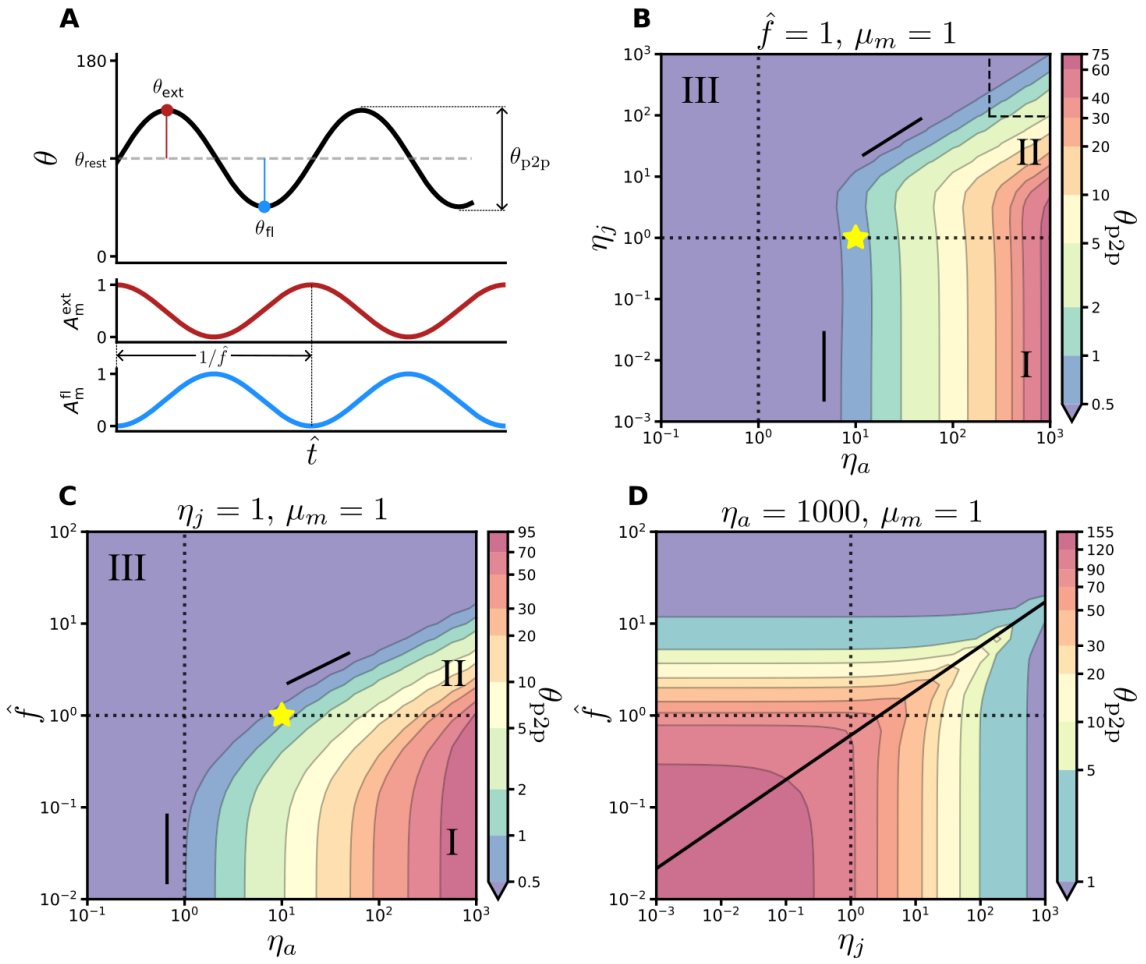

Figure 6.4: Joint angle dynamics with symmetric muscle actuation. (A) Top: Joint angle $\theta(\hat{t})$. Bottom: Muscle activation $A_m^{(\mathrm{ext,\,fl})}(\hat{t})$. Peak extension θ_{ext} (red) and flexion θ_{fl} (blue) are equal, showing symmetrical oscillations. The contour plots of the peak-to-peak joint angle amplitude θ_{p2p} as a function of dimensional variables including (B) η_a and η_p. Dashed box: high active stiffness and low passive damping parameter region approximating a rigid joint. (C) η_a and $\hat{f}$, and (D) η_j and $\hat{f}$. Panels B and C reveal similar dynamic regimes, numbered as I, II, and III. The point $\eta_a = 1000$, $\eta_p = 1$, and $\hat{f} = 1$ is represented with a yellow star. Warmer colours indicate larger amplitudes. Dashed lines indicate where $\eta_a = 1$, $\eta_j = 1$, and $\hat{f} = 1$. The remaining dimensionless variables are $\eta_a = \eta_a^{\mathrm{fl}} = \eta_a^{\mathrm{ext}}$, $\mu_j = 1$, $\gamma = 1$, and $\hat{J} = 0.1$.

$\mu_c = 50$ (Fig. 6.5C), where it is observed a systematic shift of the response surfaces in parameter space. As μ_c increases, active muscle input becomes progressively more effective at overcoming passive resistance, such that comparable joint excursions are achieved at lower values of η_a. Consequently, the boundary between the dynamical regimes I and III is displaced, expanding the region in which active dynamics dominate and therefore, compressing the regime where passive mechanics limit motion. The balance between active

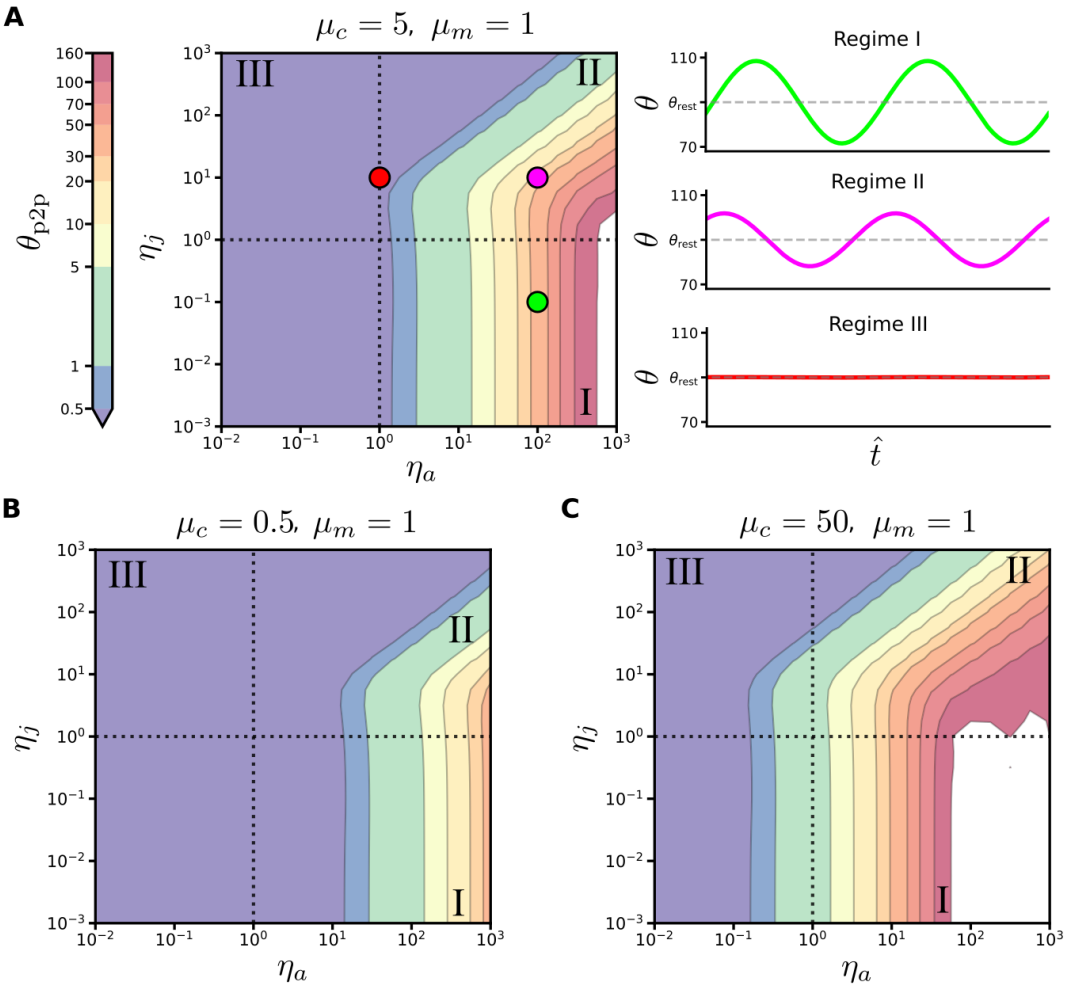

Figure 6.5: Effect of the dimensionless active–to–passive ratio μ_c on joint dynamic range under symmetric antagonistic actuation. Contour plots show the peak-to-peak amplitude θ_{p2p} as a function of η_a and η_j for fixed values of (A) $\mu_c = 5$, (B) $\mu_c = 0.5$, and (C) $\mu_c = 50$. In (A), coloured circles indicate parameter combinations corresponding to representative joint angle time traces, which illustrate the characteristic behaviour of dynamical regimes I – III. Blank regions appearing for $\mu_c > 1$ indicate parameter combinations in which MTU-generated torque becomes sufficiently large to produce unbounded joint excursions or torque saturation, preventing stable periodic motion. The shared colour bar for all three plots is shown in (A).

and passive damping, rather than their absolute values, plays a key role in determining joint dynamic range, and explains how changes in the relative contribution of MTU torque can tune joint behaviour without modifying passive joint properties.

Note that in Fig. 6.5A and C, blank regions emerge in the contour plots. These regions indicate parameter combinations for which MTU-generated torque becomes sufficiently large to drive extreme joint excursions. In these regions, the joint response exceeds the range of

stable periodic motion, leading either to numerical torque saturation or to loss of oscillatory behaviour. As a result, the joint no longer exhibits well-defined rhythmic dynamics and effectively operates outside the valid regime of the model. Additionally, to illustrate the differences between the identified dynamical regimes, Fig. 6.5A includes three representative joint angle time traces, each selected from a distinct region of the parameter space. A strongly active-driven response characteristic of regime I is illustrated for $\eta_a = 100$ and $\eta_a = 0.1$ (see green circle). illustrates strongly active-driven response. Regime II, corresponding to balanced active–passive dynamics, is represented by $\eta_a = 100$ and $\eta_a = 10$ (see magenta circle). Finally, a heavily attenuated response characteristic of regime III is shown for $\eta_a = 1$ and $\eta_a = 10$ (see red circle). These examples illustrate the progressive attenuation of joint dynamic range as the system transitions across the dynamical regimes.

Building on the symmetric antagonistic case, we introduce asymmetry and quantify its impact on the joint's dynamic range and frequency-dependent behaviour.

6.2.3 Asymmetric Antagonistic Actuation

In order to understand how muscle asymmetry influences joint dynamic range, we asked how the variations in the dimensionless muscle asymmetry ratio, μ_m, influence the peak-to-peak amplitude of joint motion, and how this interplay interacts with the activation frequency $\hat{f}$, and the passive components of the joint η_j (see Fig. 6.6). To isolate the effects of asymmetry from changes in overall actuation strength, we impose a fixed total capacity of $\eta_a^{\text{eff}} = 1000$, where η_a^{eff} is defines as

$$\eta_a^{\text{eff}} = \frac{\eta_a(1+\mu_m)}{2}\,.$$

This constraint ensures that the overall active contribution remains constant regardless the values of μ_m. Consequently, while $\mu_m = 1$ yields equal contributions from the extensor and flexor MTUs, deviations from symmetry redistribute this constant capacity between the two actuators, directly influencing the dynamic response of the joint.

As expected, introducing muscle asymmetry systematically biases the joint's dynamic range toward either extension ($\mu_m > 1$) or flexion ($\mu_m < 1$), as illustrated schematically in Fig. 6.6E. As the degree of asymmetry increases, this directional bias becomes more pronounced. However, the greater the asymmetry and resultant bias, the more limited the range of motion. The peak-to-peak amplitude, $\theta_{\mathbf{p2p}}$, decreases as the system moves away from the symmetric case, as seen in Fig. 6.6A-B. Higher amplitudes, represented by warmer colours, are concentrated near $\mu_m = 1$ and gradually diminish with increasing asymmetry. This trend is further confirmed by the extracted line plots in Fig. 6.6C, which show the reduction of θ_{p2p} as μ_m departs from unity across several values of $\hat{f}$.

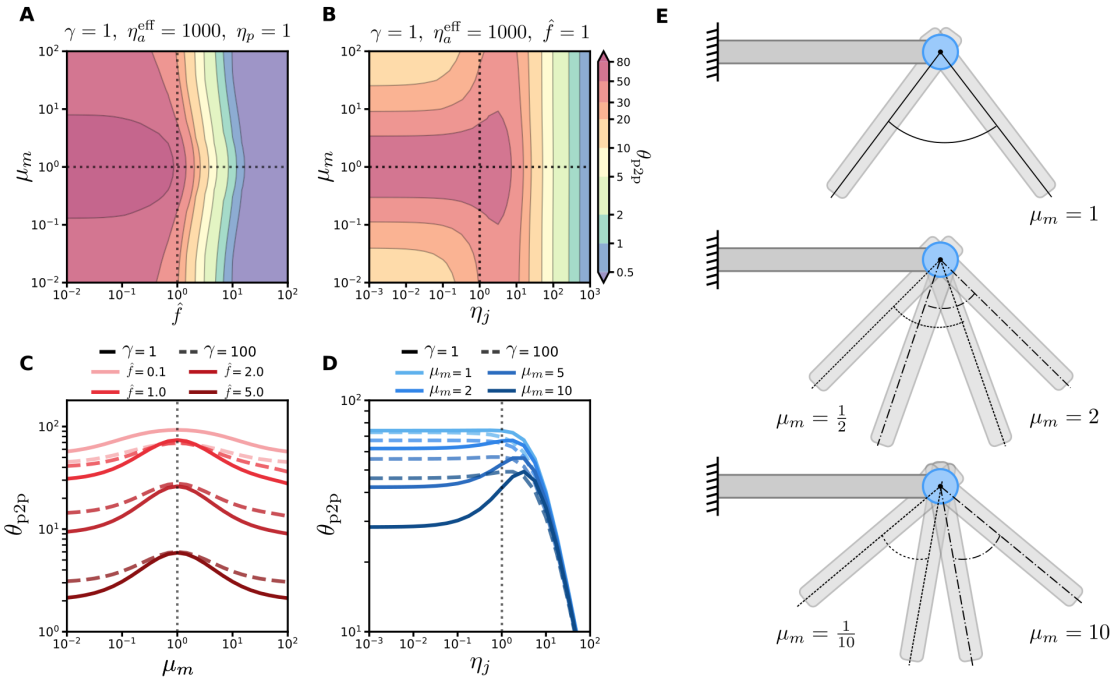

Figure 6.6: Joint angle dynamics with asymmetric muscle actuation. Peak-to-peak amplitude θ_{p2p} as a function of muscle asymmetry μ_m and (A) the activation frequency $\hat{f}$, and (B) the passive stiffness-to-damping ratio η_j, for a fixed $\gamma = 1$. Extracted line plots from panel B show θ_{p2p} as a function of (C) η_m for fixed values of $\hat{f}$, and (D) η_j for fixed values of μ_m. Solid and dashed lines correspond to $\gamma = 1$ and $\gamma = 100$, respectively. (E) Schematic representation of the joint's θ_{p2p} amplitude. From top to bottom: symmetric case ($\mu_m = 1$), with oscillation amplitudes evenly distributed about the rest angle. Two asymmetric configurations ($\mu_m = 2$, $\mu_m = 10$ and their respective inverse $1/\mu_m$), showing a biased dynamic range due to actuator imbalance.

Moreover, as established in Section 6.2.2, the joint range in Regime I is dominated primarily by active muscle contributions (see Fig.6.5), indicating that modulating the activation frequency alone is insufficient to fully restore the dynamic range imposed by muscle asymmetry. This is showed in Fig. 6.6A, where columns at fixed $\hat{f}$ show similarly reduced amplitudes across the asymmetric range. Hence, naively, muscle asymmetry imposes a significant limitation to the joint functionality. Nonetheless, the interaction between muscle asymmetry and passive joint mechanics reveals a more nuanced picture. While a low stiffness-to-damping ratio, η_j, appears preferable in the symmetric case, increasing passive joint stiffness in the presence of muscle asymmetry can partially mitigate the loss of dynamic range (see Fig 6.6D).

In particular, joints with intermediate passive stiffness ($1 < \eta_j < 10$) maintain the directional bias imposed by asymmetric actuation whilst recovering nearly the full dynamic range. Furthermore, reduced frequencies in this condition result in similarly increased peak-to-peak amplitudes to the symmetrical configuration. Therefore, a mechanical configuration

where passive stiffness is arranged in parallel to the actuators, like in our antagonistic-MTU joint model, stores and routes the energy within the system and thus provides robustness in the face of asymmetrical actuation. By shaping how active torques are transmitted into motion, passive joint mechanics enhance robustness to muscle asymmetry, allowing directional control to be maintained without substantially compromising joint mobility.

This effect is further modulated by joint loading. At high load conditions ($\gamma = 100$, see dashed lines in Fig. 6.6C-D), moderate passive stiffness enhances symmetry breaking and supports a robust dynamic range across a consistent η_j range, even in the presence of actuator asymmetry. Conversely, under low loads ($\gamma = 1$, see solid lines in Fig. 6.6C-D), the parameter space supporting stable joint motion becomes more restricted, and maintaining joint excursions requires staying within the optimal range of passive stiffness ($1 < \eta_j < 10$). Outside this range, joint motion is either excessively damped or dominated by asymmetric active torques, leading to a marked reduction in dynamic range. These results demonstrate that the interaction between passive joint mechanics and external loading critically shapes how asymmetrically actuated joints generate and sustain movement, while highlighting the need to optimise passive properties in asymmetrically actuated joints to reduce performance trade-offs.

In conclusion, passive joint properties do not merely stabilise motion but actively structure how asymmetries in muscle actuation and external load are expressed at the joint level. This provides a basis for understanding how biological joints maintain functional versatility despite inherent asymmetries and variable loading, a theme that is explored in the following discussion.

6.3 Discussion

In this chapter, we evaluated two main anatomical configurations of biological joints: actuation with a pair of antagonistic muscle-tendon units that are either symmetrical or asymmetrical in their strength. By using our nondimensional antagonistic-MTU joint model, we characterise the passive viscoelastic dynamics of the joint to establish a baseline description of how stiffness, damping, inertia, and loading shape joint relaxation. Building on this foundation, we examined how rhythmic muscle activation interacts with passive joint mechanics under symmetric actuation, identifying distinct dynamical regimes that govern joint amplitude and frequency response. We extended this framework to asymmetric actuation, where total active capacity was conserved, to investigate how imbalances in muscle strength bias joint motion and how passive joint properties and external loading modulate this effect.

As discussed in Chapter 5, joint motion in the absence of muscle activation is governed

by the balance between elastic and viscous elements [7, 8, 97]. This effect is particularly pronounced in insects and low mass animals, where low inertia and minimal gravitational forces enhance the contribution of passive elements [3, 12, 44, 63]. Stiffer joints produce faster passive returns, whereas viscous-dominated joints exhibit slower, monotonic relaxation. The contour maps of relaxation time presented here reproduce the same qualitative dependence on stiffness, damping, inertia, and loading that emerged from the experimentally grounded single-MTU joint model (see Section 5.3.2), including the transition between overdamped and underdamped regimes.

Importantly, whereas the previous chapter demonstrated that realistic joint kinematics can arise from passive viscoelasticity alone, the present results clarify why this is the case. The dimensionless parameters explicitly show how passive joint mechanics set the intrinsic time scale and stability landscape within which muscle activation operates. In this sense, the passive properties identified in the single-MTU joint model do not simply reproduce observed motion, but place the joint within a mechanically sensitive region of parameter space that supports stable joint motion while allowing muscle activation to effectively shape movement.

To characterise the joint dynamical regimes and their associated time scales under symmetrical and asymmetrical conditions, we considered responses under fixed load, either low or high, and sinusoidal input. Across these conditions, the response of the joint can be interpreted using a filter analogy. When muscle stiffness dominates, under low or moderate load and with limited passive contribution, the joint behaves as a pass-through filter (regime I). In this regime, motion amplitude is largely preserved, damping is minimal, and phase delay is governed by the elastic time scale of the actuator. As passive stiffness increases beyond a critical threshold, motion becomes progressively attenuated. Here, the joint response resembles that of a low-pass filter (regime II). Finally, when passive stiffness dominates over active stiffness, oscillatory motion is strongly damped out, consistent with a stop-band filter (regime III), in which active inputs are largely filtered out by passive resistance.

The filter analogy provides intuition about the characteristic time scale of the system, for which the joint achieves maximum amplitude. Due to the fact that this analysis is grounded in a general nondimensional framework, these regimes and transitions are not specific to a particular joint size or loading conditions. Instead, they reflect general principles of active-passive mechanical systems. In fact, the filter analogy has been applied in other biological contexts. A similar interpretation has been observed in undulatory motion in invertebrate swimmers [30], demonstrating the broader relevance of dimensionless analysis for understanding how structure and actuation jointly shape dynamics.

Although symmetric antagonistic actuation yield optimal joint performance by aligning

with regime I and maximising range of motion, introducing asymmetry can be beneficial in specific contexts. These include load-bearing tasks or scenarios where the design of bioinspired joints is constrained by actuator power, mass, spatial footprint, or even monetary cost. In biological systems, asymmetry may also reflect optimisation with respect to resting metabolic expenditure rather than peak kinematic performance alone. One clear mechanical consequence of actuator imbalance is its effect on dynamic range, shifting it toward either extension or flexion, and suppressing it. Across the explored parameter space, symmetric configurations consistently outperform asymmetric ones, independent of activation frequency. Thus, while asymmetry can support directional bias or task-specific requirements, it introduces inherent trade-offs in joint mobility that must be compensated by other elements of the system, such as passive joint mechanics or loading conditions.

We show that in tasks with directional bias (*i.e.*, unidirectional movement), passive joint compliance can mitigate against the imbalance and reduced dynamic range that occur due to muscle asymmetry. Under low-load conditions, when the passive stiffness-to-damping ratio exceeds unity, typically between one and ten, the joint reaches peak amplitude, indicating an optimal range that minimises attenuation. While in symmetric configurations any degree of passive stiffness attenuates the dynamic range, the joint performance improves significantly in asymmetric cases when passive properties are tuned within this optimal range. Even under high loads, effective joint motion can be maintained if passive stiffness remains close to its optimal value.

It is worth noting that in the antagonistic-MTU joint model, passive stiffness acts in parallel with the MTUs at the joint level, representing the combined elastic contribution of periarticular structures, such as joint capsule and connective tissue, that generate restoring moments as the joint is displaced from its position [47]. This arrangement is distinct from series compliance, which arises primarily from tendon or apodeme elasticity within the MTU itself. In biological joints, both arrangements coexist. However, as noted in Section 3.6, the present model merges muscle and tendon elasticity into a single active element, thereby capturing only the parallel contribution and omitting the series compliance associated with tendon-like structures. As a consequence, elastic energy storage and release through series elements are not represented in the current framework. This is a recognised simplification, and incorporating series compliance into the model would be a natural extension, particularly in the context of multi-joint locomotion where tendon elasticity plays a more significant energetic role.

Importantly, this analysis consider joint motion under a fixed configuration relative to the external load. In contrast, both animals and robotic systems can actively change posture or reorient their limbs to exploit the stronger actuator. Such reconfiguration provides an additional control dimension through which actuator asymmetry can be exploited rather

than compensated for. When combined with appropriately tuned passive joint properties, higher-dimensional control strategies offer a means to reconcile strength and dexterity in asymmetrically actuated systems. Notably, this highlights that the functional consequences of muscle asymmetry cannot be fully understood at the single-joint level alone, but depend on how joints are embedded and coordinated within larger musculoskeletal or robotic structures.

These results contribute to a broader understanding of joint mechanics across scales, with potential to inform the design of bioinspired robotic systems. Furthermore, the findings presented illustrate the usefulness of computational modelling for active-passive systems. Further extensions of the model framework presented here can be used to develop more sophisticated biomechanical and robotic systems that effectively balance structural constraints with functional demands.

Chapter 7

Multi-Joint Insect Model

7.1 Overview

In Chapters 3 and 4, we introduced the three hierarchical levels of the single joint model and presented their mathematical formulation. Here, we take the third modelling level, the physics-based joint, and use it as the foundational component for constructing a full leg and, ultimately, a whole-body insect model. The single joint model acts as a modular unit to assemble a three-joint leg by chaining these units together. The principle remains identical to the physics-based formulation: a viscoelastic hinge joint actuated by a pair of antagonistic muscle–tendon units (MTUs) connecting two rigid segments. Fig. 7.1 illustrates the modelling approach adopted here.

The leg consists of three segments connected in series by three joints: the thorax–coxa joint (ThC), which attaches the leg to the body; the coxa–femur joint (CFe), which lifts and lowers the leg; and the femur–tibia joint(FeTi), which drives tibial extension and flexion. This kinematic arrangement, as well as the overall body structure, takes inspiration from insect morphology. In particular, the geometry, proportions, and segmental organisation follow the dung beetle body plan, which provides a biologically grounded template for studying multi-joint coordination and whole-body dynamics. The complete model consists of six legs and two rigid body segments representing the thorax and abdomen. For a detailed description of the whole-body structure and implementation, see Section 4.7.

With this model, we extend our analysis of how active and passive properties of the joint interact to produce stable and robust motion from the level of a single joint to that of the whole body. Studying a single joint in isolation was necessary to characterise how muscle-like actuators and passive viscoelastic elements shape local dynamics. However, animals move through the coordinated action of multiple such joints, coupled mechanically

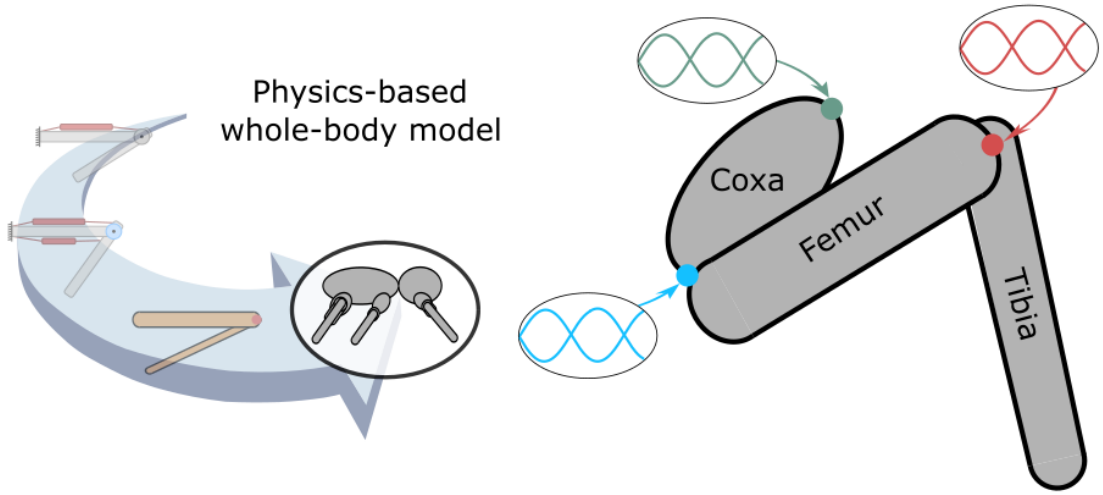

Figure 7.1: In this chapter, we adopt the third level of modelling hierarchy, the physics-based joint model, and use it as a building block to form multi-joint limb and, ultimately, a whole-body model. The multi-joint limb possess three degrees of freedom, each actuated by a pair of antagonistic MTUs driven by anti-phased activation signals.

through the body and driven by distributed muscle activation. Building on the physics-based joint model, we therefore construct a full-body insect model to investigate how these active–passive interactions scale to multi-joint limbs and whole-body locomotion.

The multi-joint insect model aims to determine whether our physics-based joint formulation (viscoelastic joints actuated by antagonistic muscle-like actuators) can reliably scale from isolated single joint dynamics to coordinated, multi-joint leg motion and to whole-body locomotion. Specifically, we test whether a limb composed of our joint modules reproduces the dynamical signatures observed in earlier single joint analyses, and whether a body composed of these same modules can produce stable tripod-like walking under simple feedback control. In the longer term, this framework is intended as a foundation for a whole-body model capable of performing multiple tasks within a single mechanical architecture, in which passively viscoelastic, muscle-driven limbs can be re-used and re-coordinated across behaviours rather than redesigned for each individual task. Dung beetles are a particularly relevant inspiration here, as their morphology supports a wide repertoire of behaviours, including walking [108], galloping [102], and ball-rolling [76, 81], using the same underlying limb architecture. This makes them well suited as a reference for testing how far a single mechanical design can be pushed toward different locomotor demands.

This chapter presents the results obtained from the multi-joint insect model. We begin in Section 7.2.1 by establishing the passive stiffness and damping values selected for the leg joints. Section 7.2.2 then examines whether the model can reproduce realistic joint trajectories when the MTUs are driven by activation profiles optimised from dung beetle walking

data under fixed-body conditions. This section also explores how variations in passive and active properties shape the resulting joint dynamics. Section 7.2.3 presents the transition to whole-body locomotion, introducing the feedback control scheme, demonstrating tripod-like walking, and characterising the limits of locomotor performance through systematic variations in target-trajectory frequency and applied external load. Finally, Section 7.3 provides a broader interpretation of the findings.

7.2 Results

In Section 4.7, the structure and implementation of the insect model were presented. It was described that each leg joint is actuated by a pair of antagonistic MTUs and possesses intrinsic passive stiffness and damping properties. These passive parameters are selected with two objectives in mind. Firstly, to enable the model to maintain stable body support in the absence of active actuation; and secondly, to ensure realistic passive limb behaviour. The following section explains the reasoning and process for selecting these joint properties.

7.2.1 Passive Joint Viscoelasticity

Insects joints are structurally capable of generating passive forces that can drive limb movements independently of muscle activity [3, 4, 63]. In the context of our insect model, reproducing such passive dynamics is key to guaranteeing that the simulated limb behaviour reflects the interaction between passive mechanical characteristics and active muscle-driven movements.

The selection of passive stiffness and damping values for the multi-joint model builds on the single joint analysis presented in Section 5.3.3. There, a simplified MuJoCo model of the locust hind leg FeTi joint was used to identify stiffness and damping combinations that reproduced experimentally measured passive flexion dynamics. These results offer both a methodological framework for identifying biologically plausible viscoelastic parameters and a biomechanical benchmark for insect-scale limb joints. Although the insect model represents a dung beetle rather than a locust, the locust-derived parameters provide an empirically grounded starting point. Both animals are small arthropods whose limb mechanics is governed primarily by viscoelastic principles rather than absolute size [63, 105]. Additionally, in the single-joint analysis, the locust FeTi parameters are constrained by experimental joint trajectories, defining a functionally feasible zone of stiffness–damping space. This zone guides the parameter selection for the dung beetle model and anchors the model in experimentally validated dynamics.

Furthermore, the locust values are used not as exact species-specific estimates, but as order-of-magnitude references that inform subsequent tuning under the dung beetle specific constraints, such as body mass distribution and required weight support. In this model, the passive parameters are adjusted away from the locust values where necessary to ensure passive stability and posture [98], but they remain within a regime that has already been shown to reproduce insect-like passive dynamics in the single joint scenario. On this basis, the hind legs are assigned slightly higher stiffness and damping compared to the front and middle legs, reflecting the greater size and mass of the hind leg. The corresponding joints in contralateral legs were set at identical values to maintain the bilateral symmetry of the legs.

The final set of passive stiffness and damping values for each joint is summarized in Table 7.1. These values are used in subsequent simulations in which active muscle actuation interacts with the passive properties of the limbs.

Joint Viscoelastic Parameters			
Leg	**Joint**	κ_{pass} **(mN·mm/rad)**	β_{pass} **(mN·mm·s/rad)**
Front	ThC	5.1	0.51
	CFe	5.0	0.45
	FeTi	1.0	0.25
Middle	ThC	6.4	0.64
	CFe	5.0	0.45
	FeTi	1.0	0.25
Hind	ThC	7.9	0.79
	CFe	7.0	0.65
	FeTi	1.5	0.30

Table 7.1: Passive stiffness κ_{pass} and damping β_{pass} parameters for the thorax-coxa (ThC), coxa-femur (CFe), and femur-tibia (FeTi) joints of each front, middle and hind legs in the multi-joint insect model.

7.2.2 Fixed Body

This section examines the capacity of the multi-joint model to reproduce biologically realistic joint motion. In Section 5.3.3, it was shown that a single MuJoCo passive joint actuated by one MTU successfully reproduced characteristic features of locust joint dynamics. Here, this approach is extended to a more complex configuration in which each passive joint is actuated by a pair of antagonistic MTUs. This increased complexity introduces inter-joint coupling and requires coordinated muscle activation across multiple DoFs, providing a more

demanding test of the ability of the model to generate realistic kinematics.

To isolate the intrinsic joint-muscle dynamics, the body of the model is fixed in space. By doing so, the influence of ground reaction forces, body pitching, and whole-body inertia coupling is removed. As a result, the joint motion is governed only by the corresponding muscles and passive-joint torques, without feedback from movement of the body. This setup provides a controlled environment for exploring the performance of the antagonistic MTU-driven actuation and passive viscoelasticity without whole-body effects. In addition, the thorax-coxa (ThC) joint is locked, limiting the movement to the coxa-femur (CFe) and femur-tibia (FeTi) joint (see Fig. 7.2A for details). Focusing on these two DoFs is sufficient to assess whether the multi-joint limb can reproduce the timing, amplitude, and rhythmic structure of biological leg motion.

To evaluate the model under these conditions, the limb is driven using joint trajectories derived from a previously published dung beetle walking model [77, 108]. This study, however, does not provide numerical trajectories; hence the joint profiles were reconstructed by digitising the published kinematic traces [121]. The resulting data is then interpolated and low-pass filtered to obtain smooth profiles that preserved the characteristic timing and amplitude of the walking motion. These reconstructed trajectories serve as target references for the CFe and FeTi joints in the fixed-body experiments.

Reproducing the reconstructed joint trajectories depend on finding the appropriate muscle activation signals. This is achieved through an optimisation procedure. Standard gradient-based methods are avoided because the MuJoCo simulator is not fully differentiable; it includes discontinuities, contact interactions, and non-linear muscle-joint dynamics, which can make gradient estimates unreliable. As a result, each candidate activation pattern is evaluated via a forward simulation, and the resulting joint motion is compared with the reference trajectories. This optimisation is carried out using the *nevergrad* library [86], specifically the `OnePlusOne` algorithm, which is well suited to problems with noisy objective functions. The optimiser adjusted the activation profiles on the antagonistic muscle pairs over the stride cycle, aiming to minimise the tracking error of both joints simultaneously.

The optimisation consistently converged on activation patterns that reproduce the reconstructed joint trajectories from the walking gait. Fig. 7.2B-D illustrates the optimised muscle activation profiles on the first and third panels of the CFe and FeTi joints for the front, middle and hind legs of right side. These profiles display periods of co-activation between the antagonistic MTUs. This reflects the mechanics of a MTU-joint system, where co-activation increases joint stiffness and enhances impedance regulation, allowing the optimiser to fine-tune the trajectory despite the nonlinearities inherent in the MTU model. Indeed, similar patterns of co-activation have been documented in insect locomotion [53,

127], where modulating joint stiffness is essential for stabilising limb trajectories and controlling interaction with the substrate [54].

Once the optimisation activation signals are obtained, they are applied to the MTU models to generate the torques acting on the joints. Under these signals, the simulated CFe and FeTi trajectories closely follow the reference profiles, reproducing both the timing and amplitude of the movements. The second and fourth panels of Fig. 7.2B-D show the CFe and FeTi joint trajectories for all six legs. Note that the right and left joint trajectories are out of phase with each other, such that they produce asynchronous movements that correspond to the typical tripod gait seen in insects [24, 25, 95, 123].

These results demonstrate that the multi-joint limb, actuated by antagonistic MTUs and tested under fixed-body conditions, can produce realistic insect-like joint kinematics. This naturally raises two questions: how do the joint trajectories change when the passive properties of the joint are varied?, and can the optimised muscle activation signals drive walking when the body is free to move? To initially address the first question, we modify the passive viscoelasticity of the model joints to investigate whether the same dynamical regimes first observed in Section 6.2.2 also emerge in the insect model.

In Section 6.2.2, we examined how the active muscle (η_a) and passive joint (η_j) components of the joint system shape the dynamic range of the joint. This analysis revealed three different dynamical regimes: Regime I, where the range is dominated by the active properties; Regime II, where maintaining the range requires a balance between active and passive components; and Regime III, where insufficient active stiffness suppresses the range almost entirely. Fig. 7.3A recalls the contour plot (adapted from Fig. 6.4) that define these regimes under sine wave activation and symmetric actuation using the nondimensional antagonistic-MTU joint model.

Following this baseline characterisation, we examine how the regime structure changes when the nondimensional antagonistic-MTU joint is driven by the previously optimised activation signals used to generate the dung beetle joint trajectories rather than the prescribed sine wave inputs. Fig. 7.3B shows the resulting contour plot of the peak-to-peak amplitude θ_{p2p} across the same (η_a, η_j) parameter space. Compared to the sine wave case, three distinct regions corresponding to Regimes I-III remain clearly identifiable. However, there are changes in the structure of the regime boundaries. Under sinusoidal activation, the transition from Regime I to Regime II occurred at an approximately constant passive stiffness-to-damping ratio ($\eta_j \approx 10$), resulting in an almost horizontal transition boundary (see dark blue dotted line in Fig. 7.3A). In contrast, the dung beetle activation profiles produced a diagonally oriented transition boundary (see dark blue dotted line in Fig. 7.3B), such that increasing η_a shifted the transition from Regime I to Regime II toward lower values of η_j.

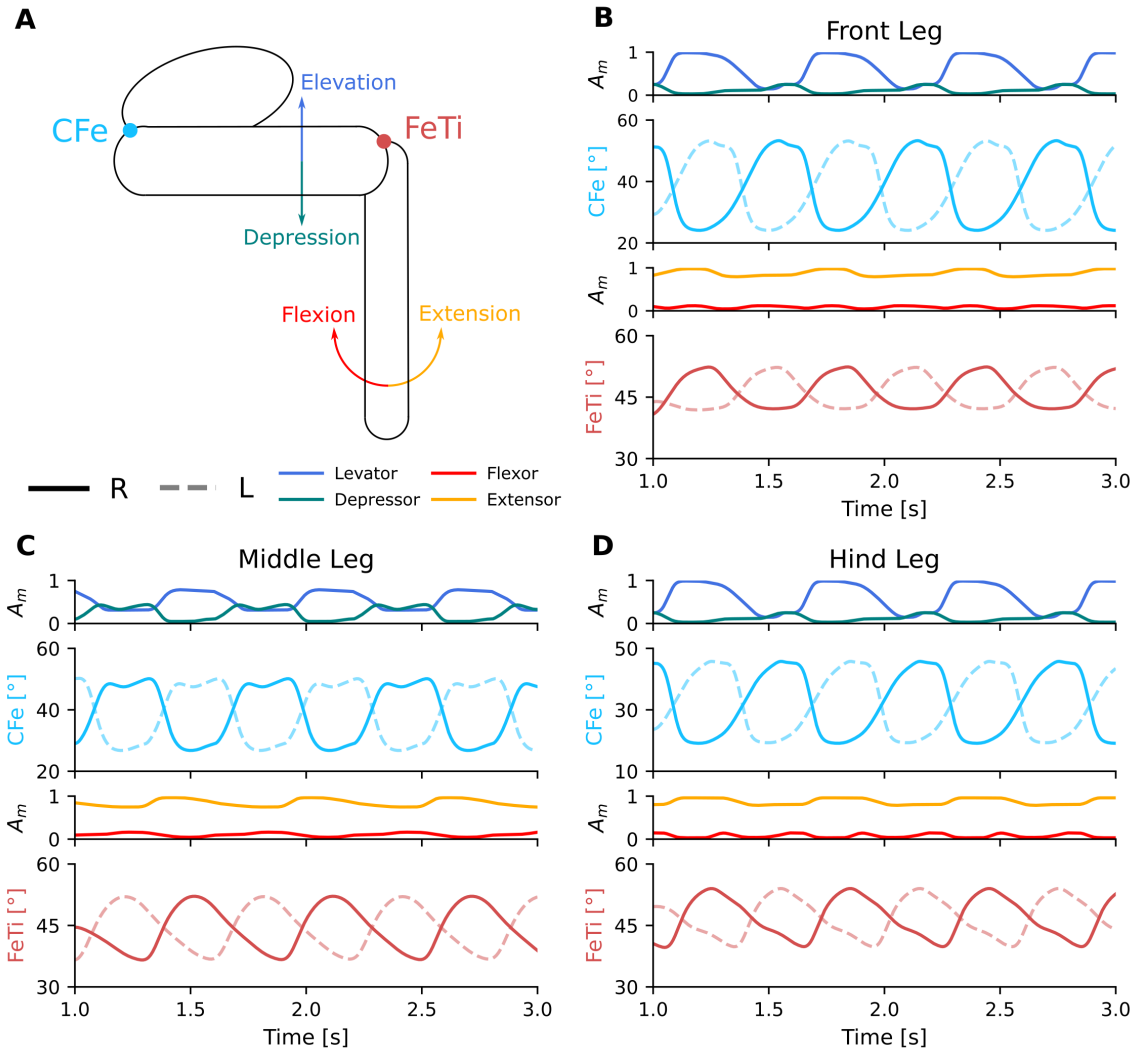

Figure 7.2: Muscle activation profiles and joint angles with fixed body. (A) Schematic of a representative leg showing the coxa-femur (CFe) and femur-tibia (FeTi) joints. Increasing CFe angles correspond to femur elevation (lifting), while decreasing angles indicate depression. Increasing FeTi angles extend the tibia, whereas decreasing angles flex it. Muscle activation signals and joint angles reproducing walking behaviour with the body fixed for (B) the front leg, (C) the middle leg, and (D) the hind leg. From top to bottom: activation of the levator and depressor muscles; CFe joint angles (light blue); activation of the flexor and extensor muscles; and FeTi joint angles (dark red). Note that, for each joint, the two muscles actuating it display activation patterns that are in anti-phase. Right-side angles are shown as solid lines and left-side angles as dotted lines.

This diagonally oriented transition boundary is also observed, and is even more pronounced, in Fig. 7.3C. When the same optimised dung beetle activation is applied to the physics-based multi-joint limb (with the ThC and CFe joints fixed and only the FeTi joint actuated), the transition between Regime I and Regime II exhibits a stronger diagonal tilt across the (η_a, η_j) space. Furthermore, the entire parameter space is shifted by approxi-

mately one order of magnitude toward lower values of η_a. Thus, comparable peak-to-peak FeTi joint amplitudes are achieved at smaller active stiffness-to-damping ratios than in the nondimensional framework.

To assess whether the dynamical regimes identified at the isolated FeTi joint persist when inter-joint interactions are introduced, we repeat the parameter sweep with the CFe joint also activated and free to move, thereby allowing mechanical coupling between adjacent joints. Although the full leg comprises three joints, activating the CFe and FeTi joints alone is sufficient to capture the relevant coupled dynamics for this analysis. Fig. 7.3D shows the resulting contour plot. Overall, the regime structure and transition boundaries remain largely unchanged compared to the single joint condition (Fig. 7.3C). However, in this case, higher peak-to-peak amplitudes are observed at low values of η_a, reflecting additional tibial motion induced by femur recoil when both active and passive stiffness at the FeTi joint are low, and highlighting the influence of inter-joint mechanical coupling.

In Fig. 7.3B–D, we overlay a white dotted contour line corresponding to a peak-to-peak FeTi joint amplitude of 17°, approximately matching the joint excursion reported in [108]. In addition, a cross marker indicates the default parameter set (η_a, η_j) used in each model. Notably, the default parameter set lies close to the transition boundary between Regime I and Regime II, and slightly within Regime II across both the nondimensional and physics-based simulations, despite differences in model formulation and absolute joint amplitudes.

The corresponding default active parameters differ between frameworks. For the nondimensional model driven by optimised dung beetle activation profiles (Fig. 7.3B), the default values are $\eta_a = 500$, $\eta_j = 5$, whereas for the physics-based framework (Fig. 7.3C-D) the default values are $\eta_a = 100$, $\eta_j = 5$. Importantly, this difference in η_a does not reflect a change in the relative balance between active and passive joint contributions, but instead arises from differences in the scaling of active torque generation between the two modelling frameworks. In the nondimensional model, this scaling is governed by the dimensionless parameter μ_c, which can be adjusted to shift the parameter space (as discussed in Section 6.2.2) and align it with the physics-based framework, thereby enabling calibration between the two models. Finally, for all panels (A–D), the joint trajectories generated at the corresponding reference parameter sets are shown over a two-second interval.

These results demonstrate that the multi-joint limbs reproduce the three dynamical regimes identified in the contour analysis. Importantly, these regimes persist under gait-derived activation profiles and across both nondimensional and physics-based modelling frameworks. Therefore, these regimes represent inherent characteristics of the joint dynamics, independent of any particular actuation scheme or model formulation. Together, these findings address the first question posed; varying the balance of active and passive

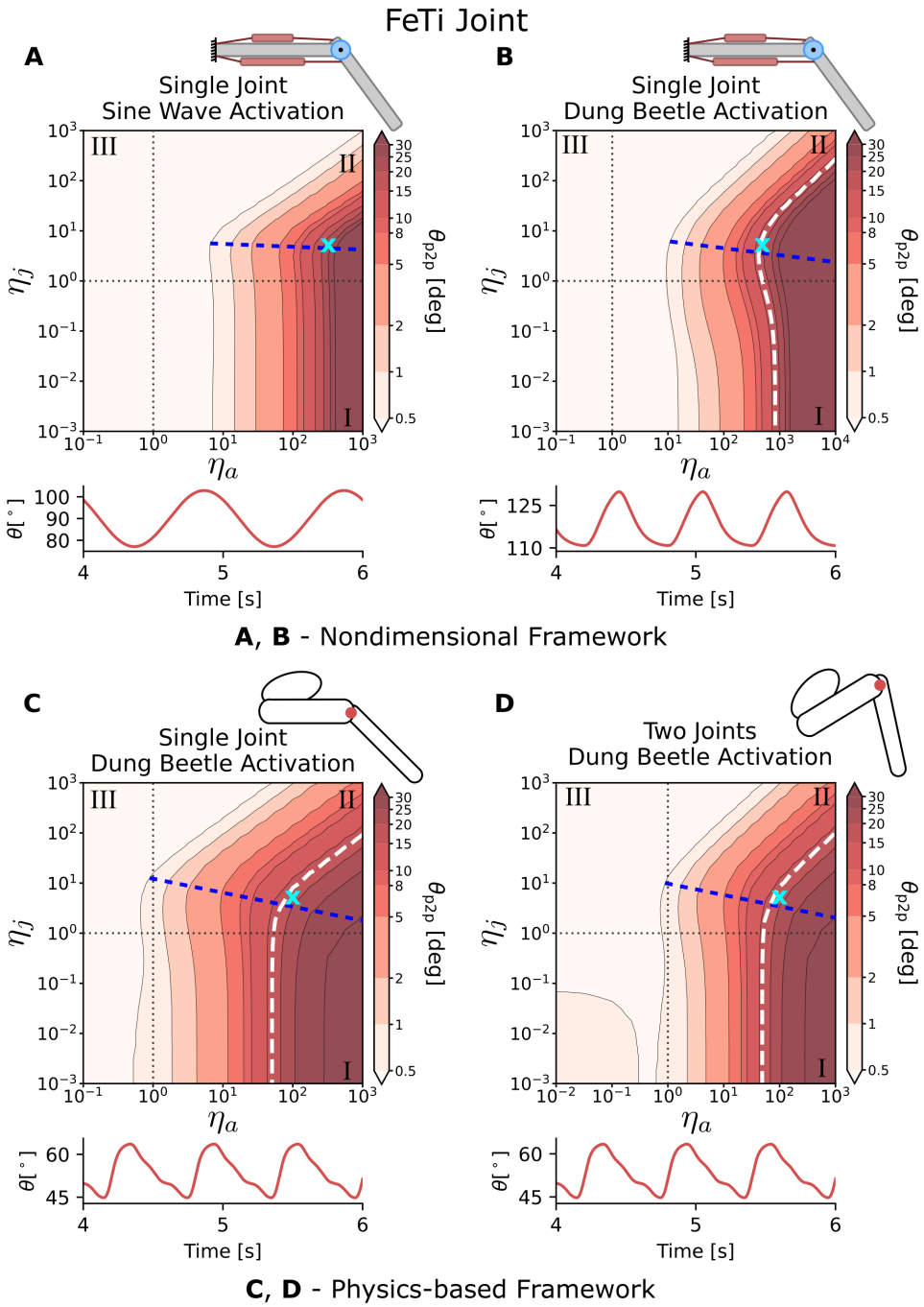

Figure 7.3: Dynamical regimes of FeTi joint motion across modelling frameworks and activation conditions. Contour plots of peak-to-peak FeTi joint amplitude θ_{p2p} as a function of the active stiffness-to-damping ratio η_a and the joint passive stiffness-to-damping ratio η_{j}. (A) Nondimensional antagonistic-MTU joint under sinusoidal activation, showing the three identified Regimes I, II and III (adopted from Fig. 6.4.) (B) Same model driven by optimised dung beetle activation profiles, revealing a diagonally oriented transition between Regimes I and II. (C) Physics-based limb model with only the FeTi joint actuated, showing a similar regime structure shifted toward lower η_a. (D) Physics-based limb model with both CFe and FeTi joints free, illustrating the persistence of regime structure under inter-joint mechanical coupling. White dotted contour denotes a peak-to-peak FeTi amplitude of 17°, and the cross marks the default parameter set used in each framework. Corresponding joint trajectories at these reference points are shown for all panels. Dashed lines indicate where $\eta_a = \eta_j = 1$.

properties robustly change the amplitude of joint motion. Thus, the activation signals must interact with these properties to shape realistic limb motion. We now turn to the second question: can these optimised signals drive coordinated walking when the body is free to move?

7.2.3 Unfixed Body

This section releases the body from space and examines the motion of the insect model including full body–leg dynamics. Unfixing the body introduces additional degrees of freedom, such as whole-body translations, rotations, and interactions with the ground via reaction forces. This creates a more realistic but mechanically complex scenario, where limb motion is no longer isolated and MTU-generated torques must overcome both body inertia and environmental constraints. Here, we assess whether the optimised activation signals obtained under fixed-body conditions can still produce coordinated leg movements and walking-like kinematics when the limbs operate within a freely moving body.

When tested under this unfixed-body condition, the model shows that the optimised activation signals obtained in Section 7.2.2 are not appropriate to generate walking. At the start of the simulation, the model remains in a standing position due to the passive mechanical properties of the limb. However, once the legs begin to move under the optimised activation patterns, the body quickly collapses onto the ground. This immediate loss of support indicates that the torques produced by the MTUs do not compensate for the additional mass, inertial and gravitational forces, and dynamic instabilities introduced when the body is free to translate and rotate.

Two main factors appear to underlie this failure. First, the activation profiles were optimised without accounting the mechanical demands of supporting a freely moving structure. Consequently, the torques produced by the MTUs are insufficient to maintain body height or generate stable stance phases. Second, the shape and ranges of motion of the trajectories pose difficulties; the legs adopt excessively open configurations that limit their ability to resist loading and apply thrust forces. This limitation is worsen by the fact that the coxa remains fixed, removing a degree of freedom that is likely essential in our insect model kinematic configuration for redirecting leg forces and generating forward propulsion. Therefore, the trajectories optimised in isolation do not generalise to whole-body locomotion and successful walking requires coordination patterns tailored to the dynamics of the unfixed body.

To overcome these limitations, the coxa segment for all legs is unfixed, including the ThC degree of freedom to allow the limbs to generate the rotational forces necessary for propulsion. In addition, we decided to use new activation patterns to produce coordinated

and stable whole-body locomotion. This time, instead of relying on activation signals optimised under now unfixed-body conditions, we implemented a proportional-derivative (PD) controller at each joint to regulate muscle activation in real time and control joint position. The objective of this controller is to reproduce joint trajectories consistent with the walking patterns commonly observed in insects, particularly the tripod gait, and to ensure that these trajectories provide sufficient support and propulsive force to maintain the body height and drive forward motion.

The PD controller regulates muscle activation at each joint by comparing the instantaneous joint angle with a target trajectory and adjusting MTU activation accordingly. As illustrated in Fig. 7.4A, the controller computes an error term ϵ based on the difference between the desired and actual joint angles and a derivative term proportional to joint angular velocity. These terms are weighted proportional, K_p, and derivative, K_d, gains to produce a corrective activation signal. The controller output increases the activation of one MTU while decreasing the activation of its antagonist, thereby producing an anti-phase activation pattern and the torque required to drive the joint towards its target. The changes in the activation profiles are filtered to prevent abrupt changes. In this way, the controller continuously modulates MTUs activation throughout the gait cycle.

Besides its computational simplicity, the decision to use a PD controller can be justified by making two correspondences to elements of insect motor control. Insects have proprioceptive sensors that provide continuous feedback about joint position and velocity, enabling corrections during stance and swing [5, 57, 91]. On the one hand, the proportional term captures this position-dependent feedback as it reflects how deviations from a desired joint configuration trigger compensatory muscle activation, analogous to reflexes driven by position-sensitive proprioceptors. On the other hand, the derivative term represents velocity-dependent feedback, similar to the proprioceptors that respond strongly to changes in joint speed and contribute to damping and stability during rapid movements. Therefore, a PD controller provides a suitable and mechanically appropriate approximation of proprioceptive feedback acting on antagonistic muscle pairs during locomotion.

To validate the PD controller, we examined its tracking performance by driving the ThC, CFe and FeTi joints through a series of ramped joint trajectories covering the range of motion for all leg joints. Fig. 7.4B-D illustrate the results for each joint of the right hind leg (highlighted in the model schematic in Fig. 7.4A). The K_p and K_d gains were tuned to produce smooth responses approaching critically damped behaviour, ensuring that the joints reached their targets without excessive overshoot or oscillation. For each joint, the error signal (ϵ) is shown in the top panels of Fig. 7.4B-D. Note that the error consistently converges to zero once the commanded position is reached, which indicates accurate and stable tracking. The middle panels present the activation patterns of the antagonistic MTUs,

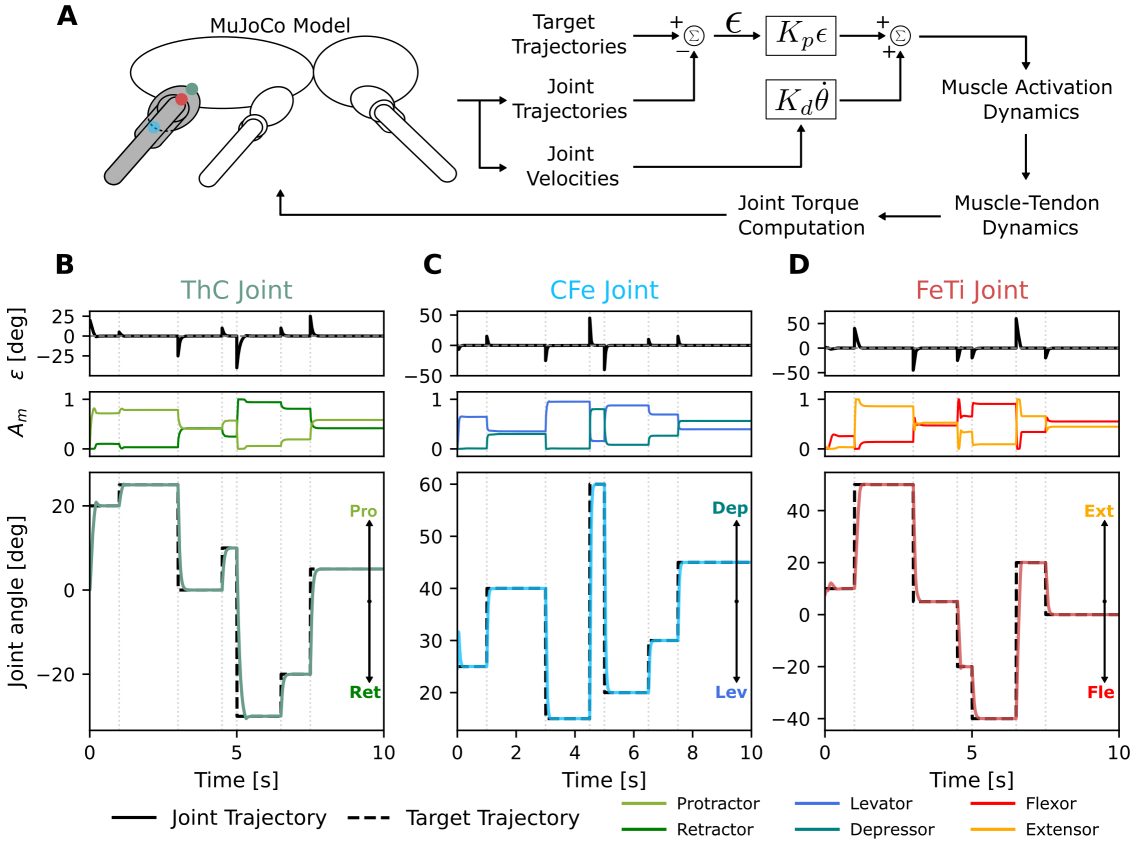

Figure 7.4: Implementation of the joint-level PD control. (A) Schematic of the whole-body model with the right hind leg highlighted, indicating the leg for which joint trajectories are shown. The thorax-coxa (ThC), in green, coxa-femur (CFe), in blue, and (FeTi), in red are marked with coloured circles. In addition, a diagram of the joint-level PD controller is included to illustrate how target joint angles are converted into motor commands. Controller signals, muscle activations, and joint trajectories of the right hind leg are shown for (B) ThC, (C) CFe, and (D) FeTi joints. Panels (B-D) contain, from top to bottom, the controller error signal ϵ, the anti-phase activation signals A_m for both muscles actuating the joint, and the joint trajectory (solid line) overlaid with the corresponding target trajectory (dotted line). Black arrows illustrate the respective movement of the joint: protraction (Pro) and retraction (Ret) for ThC, depression (Dep) and elevation (Lev) for CFe, and extension (Ext), and flexion (Fle) for FeTi. The PD control scheme achieves accurate tracking of the desired joint behaviour.

where it can be seen the expected anti-phase modulation and their profile adaptations as the target position changes. The bottom panels display the simulated joint position (solid lines) alongside their respective target position (dotted lines), demonstrating that the PD controller achieves good reference tracking. Black arrows indicate the direction of movement (protraction-retraction, depression-elevation, and extension-flexion) for each joint.

After having validated the PD controller, we now focus on generating walking in the model. Rather than using the digitised walking trajectories from [77, 108] that were pre-

viously used to optimise the activation signals in Section 7.2.2, we constructed new target trajectories for the joints using sinusoidal waveforms shaped by a hyperbolic tangent function. This was done to smooth oscillations in which the joints spend more time near their maximum and minimum positions. The joint trajectories are coordinated according to the phase relationships observed in the published dung beetle model data [108], to ensure that the timing between legs reflects a biologically inspired gait pattern. In doing so, we prioritise inter-limb coordination while sacrificing some of the fine temporal structure present in the original experimental signals. Here, the focus is to maintain proper phase relationships between the legs as this is essential for generating a stable tripod gait and supporting the body during locomotion.

Additionally, the amplitudes of the target trajectories are adjusted to keep the joints within a range of motion that allows the model to preserve a nearly upright posture during walking. These amplitudes are iteratively tuned until the model exhibits a stable stance and balanced limb configuration. Importantly, the target joint trajectories are driven at 1.2 Hz, a frequency selected to lie within a plausible walking range of an insect [18, 31, 72], as well as avoiding unnecessarily fast or slow movements that could introduce instability into the gait. Furthermore, the tibias are held in a static, extended position through the gait cycle to be consistent with [77]. By using this approach, the whole-body model successfully reproduced a stable tripod gait. The resulting walking patterns are presented in Fig. 7.5.

Fig. 7.5A shows the MuJoCo insect model walking in the virtual environment during a ten-second simulation. The red arrow indicates the forward (x-axis) direction of motion. The path taken by the model is presented in Fig. 7.5B, where the top panel shows an XY view. While the model moves forward, a slight tilt to the right is observed, likely resulting from the abrupt initiation of the walking gait from an initial passive standing posture. The bottom panel shows the XZ view, clearly illustrating forward movement. A gait diagram (Fig. 7.5C) confirms that the model reproduces a tripod gait, with three legs in stance phase (ground contact, marked with a gray bar) while the remaining three legs are lifted in swing phase.

Fig. 7.5D displays the ThC, CFe, and FeTi muscle activation signals along with the joint trajectories for the three legs on the right side of the model. The MTU activation signals exhibit the expected anti-phase pattern dictated by the PD controller, with one MTU activated while its antagonist is deactivated. Joint trajectories are shown alongside their respective target trajectories to demonstrate accurate tracking. The tibias exhibit small oscillations in their trajectories due to perturbations from ground reaction forces and movements of the other joints. Note that these oscillations are reduced when the legs are in swing phase (low CFe angles), as the tibias are not in contact with the ground and are therefore less affected by external forces, allowing them to more closely follow the target

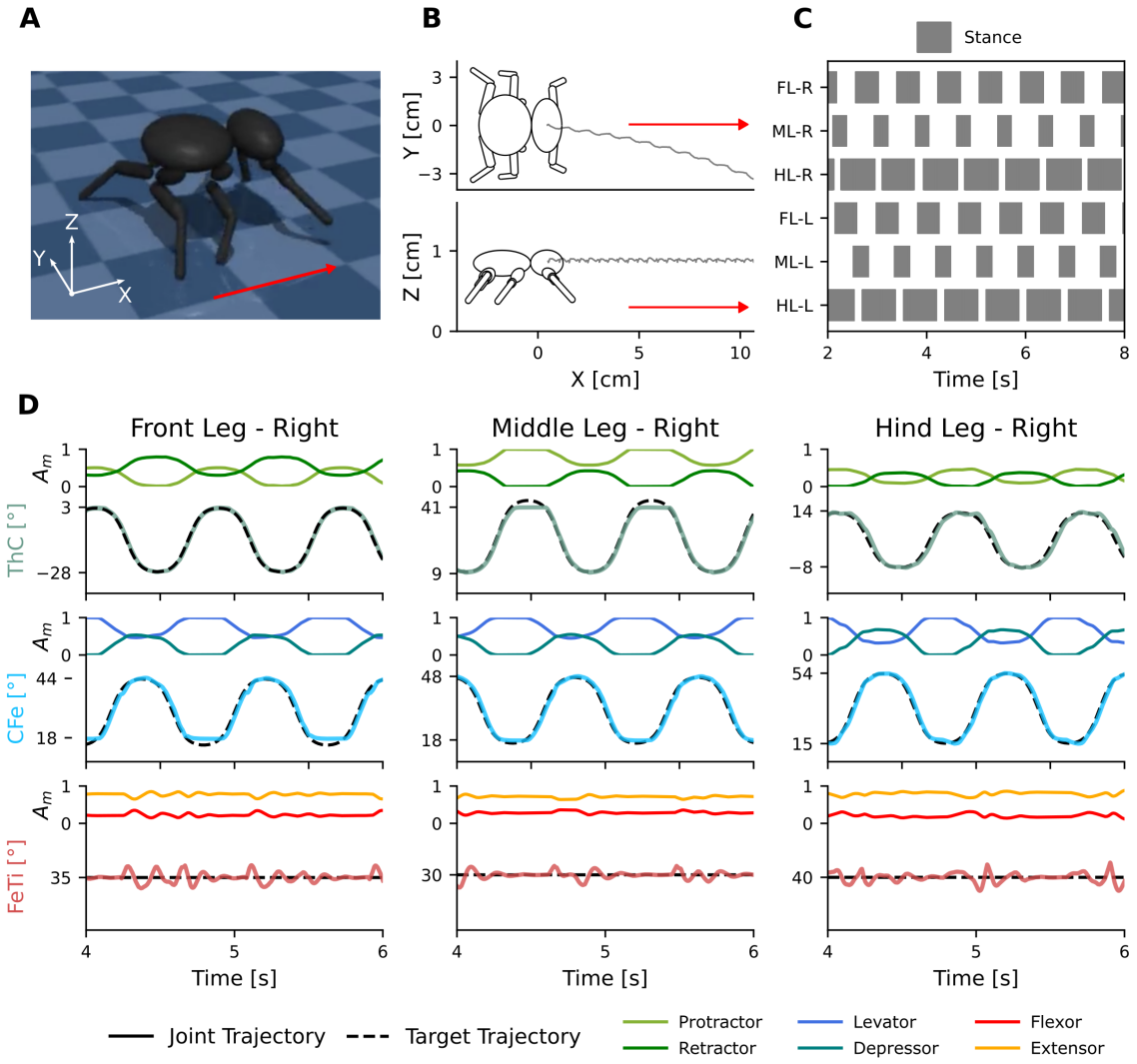

Figure 7.5: Walking gait reproduction. (A) Insect model in MuJoCo replicating a tripod walking gait. The red arrow indicates the direction of movement. (B) XY (top) and XZ (bottom) views of the forward walking path of the model. The model tilts slightly to the right while walking. Red arrows indicate the direction of movement. (C) Walking gait diagram over six seconds of simulation for the front (FL), middle (ML), and hind (HL) legs on both right (-R) and left (-L) sides. Grey bars indicate the stance phase, *i.e.* when the leg is on the ground. The leg trajectories produce a stable tripod gait. (D) Anti-phase muscle activation signals, A_m, and joint trajectories for the right ThC, CFe, and FeTi joints over two seconds of steady-state walking. Solid lines show simulated joint trajectories, while dotted lines indicate the target trajectories. Joint motions closely follow their targets, with the largest deviations observed at the FeTi joints, where the controller attempts to maintain a near-static leg position.

trajectory. These results correspond to steady-state locomotion; therefore, the first few seconds of the simulation were omitted from the plots.

Overall, the PD controller, combined with target trajectories and unfixed coxa joints, enables the model to reproduce a stable tripod gait while maintaining accurate joint tracking and body stability. The limb kinematics, inter-leg phasing, and MTU activation patterns show that the controller can compensate for ground reaction forces and body dynamics, producing coordinated and robust locomotion over the simulated gait cycles. Having established that the model can walk under standard conditions, we ask how variations in the oscillation frequency of the target trajectories and in added load influence the ability of the model to sustain stable walking, and what the limits of locomotor performance are under these control and mechanical constrains. To address these, we systematically vary the target joint frequencies (f) and scaled the body weight ($S_{\text{mass}} \times m_{\text{body}}$) to determine the conditions under which stable walking is maintained and to identify the boundaries at which the locomotor system fails.

To illustrate how the joint tracking error varies across different values of f and S_{mass}, Fig. 7.6 displays a contour plot of the root mean square error (RMSE) ϵ of the CFe joint of the right hind leg. For clarity, we focus on this joint because it plays a central role in body support and propulsion, and its behaviour is representative of the broader locomotor performance. The error metric corresponds to the RMSE between the commanded and simulated CFe trajectories, evaluated during steady-state locomotion. This metric is defined as

$$\text{RMSE}(\epsilon) = \sqrt{\langle \epsilon(t)^2 \rangle}.$$

Overall, the RMSE(ϵ) converges to zero at the lowest tested frequency 0.1 Hz. Across low mass scales, *i.e.* loads that are equal to and very close to the nominal body mass m_{body}, the RMSE(ϵ) remains small for target frequencies between 0.5 and 2 Hz, consistent with the accurate tracking observed at $f = 1.2$ Hz in Fig. 7.5. At frequencies above 3 Hz, the error increases as the system is unable to generate the rapid torque changes required for faster oscillations. Increasing S_{mass} similarly leads to larger errors even in the $1 - 3$ Hz range. This, due to the greater gravitational and inertial demands placed on the legs. To highlight the transition between accurate and degraded tracking, a contour line at RMSE(ϵ) = 3° is included (white dashed line). Deviations below this threshold have minimal effect on gait stability, whereas errors above it consistently lead to noticeable distortions in joint motion.

At frequencies and mass scales that produce high RMSE(ϵ) values, we expect substantial changes in the shape of the simulated joint trajectories. To illustrate this, Fig. 7.6B shows the ratio between the simulated and target peak-to-peak amplitudes of the CFe joint, $P2P/P2P_{\text{target}}$. When this ratio is close to one, the simulated joint closely matches the amplitude of the target trajectory; large deviations from one indicate substantial differences. Similarly to Fig. 7.6A, $P2P/P2P_{\text{target}}$ converges to one at low frequencies in the range of $0.1 - 1$ Hz. Interestingly, at low mass scales and high frequencies, the amplitude ratio

remains close to one, indicating that the joint can still achieve excursions close to the target. However, in this region, the RMSE(ϵ) reaches values between $15° - 20°$. Thus, the deviation arises primarily from phase lag rather than from a reduction in amplitude. In other words, the joint is able to reach the target extremes, but does so with a delay relative to the target trajectory. This likely occurs because the rapid changes in the target joint phase at higher frequencies require high torques to maintain amplitude. While the MTUs can generate sufficient torque to achieve the peak positions, they cannot respond quickly enough to perfectly follow the temporal structure of the trajectory, which results in a phase shift.

Conversely, $P2P/P2P_{\text{target}}$ drops near zero at high values of S_{mass} (10−20) and high frequencies ($f = 5 - 10$ Hz). This is not surprising, as the scaled body load exceeds the torque-generating capacity of the CFe joint (and the leg as a whole). This prevents the joint from supporting the body and reaching the target range of motion.

In this contour plot, we include a black dashed line at $P2P/P2P_{\text{target}} = 1$ to indicate full reproduction of the target amplitude. Because the amplitude ratio reaches values close to one at both low and high frequencies for low mass scales, in subsequent analyses we focus on the parameter region where the amplitude ratio remains close to one and the error is below 3°. This region of interest occurs at the intersection roughly between $f = 0.8$–2 Hz and $S_{\text{mass}} = 1$−10 (indicated by cyan dashed lines in Fig. 7.6C and D). It defines the operational space in which the CFe joint maintains near-target amplitudes while tracking the trajectory with minimal error, providing the most reliable conditions for stable tripod locomotion.

The RMSE(ϵ) and $P2P/P2P_{\text{target}}$ plots characterise joint-level performance; however, they do not directly indicate how well the model actually walks. To relate these control and mechanical conditions to locomotor output, Fig. 7.6C shows the walking speed, $\bar{v}$, of the model across the frequency and mass scale space. The speed is computed as the mean magnitude of the centre of mass of the velocity of the abdomen in the horizontal plane to indicate a direct forward progression independent of joint-level behaviour.

Across low to moderate mass scales, $\bar{v}$ increases with f and exhibits an approximately linear trend between $f \approx 0.1$–4 Hz. This linear regime reflects the fact that, when joint tracking is reliable, increasing f increases the stepping frequency proportionally, leading to a near-proportional increase in forward speed. Beyond $f \approx 4$ Hz, this relationship breaks down. Although walking speed continues to rise and reaches its highest values at $f \approx 8$–10 Hz, these conditions correspond to large tracking errors and distorted joint trajectories. Therefore, the increased speed at high frequencies does not reflect improved gait performance but rather arises from unstable coordinated leg motions that no longer resemble tripod walking.

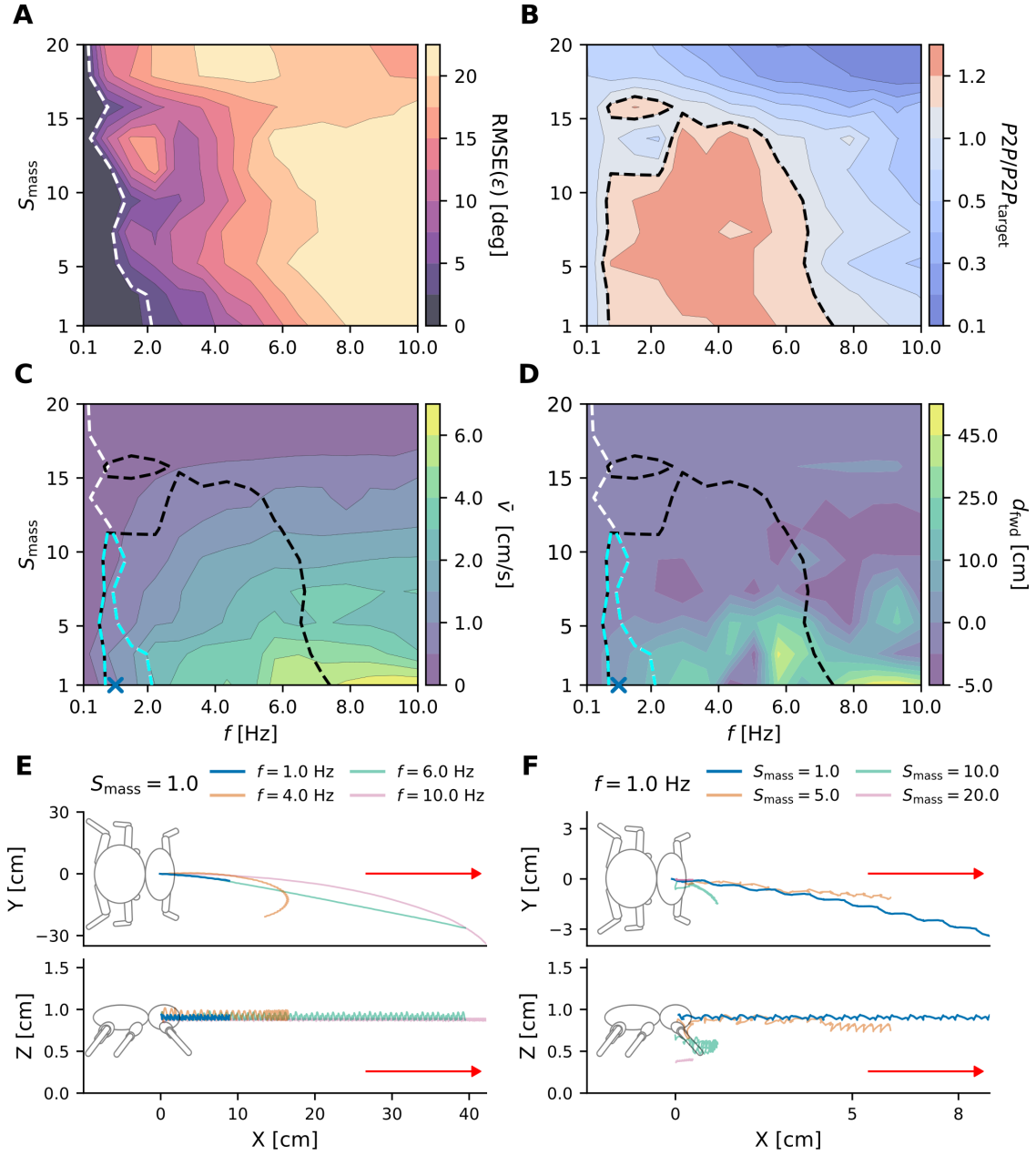

Figure 7.6: Parameter sweeps of the walking gait for different trajectory frequencies and mass scales. Contour plots show (A) the controller error signal ϵ; (B) the ratio of joint angle amplitudes $P2P/P2P_{\text{target}}$, where $P2P_{\text{target}}$ is the peak-to-peak amplitude of the target joint trajectory; (C) the walking speed $\bar{v}$; and (D) the forward (x-axis) distance d_{fxd}, as a function of trajectory frequency f, and mass scale S_{mass} (multiples of the insect body weight). White and black dashed lines denote contour levels at $\epsilon = 3°$ and $P2P/P2P_{\text{target}} = 1$, respectively, while cyan dotted lines highlight the region of interest where these contours intersect. Panels (A) and (B) show only the right hind leg for illustrative purposes. XY (top) and XZ (bottom) views of the forward path followed by the model are shown in (E) for four simulations at fixed $S_{\text{mass}} = 1$ with $f = [1, 4, 6, 8]$ Hz, and in (F) for four simulations at fixed $f = 1$ Hz with $S_{\text{mass}} = [1, 5, 10, 20]$. A blue cross in panels (C) and (D) marks the simulation run located within the region of interest.

Importantly, the most meaningful locomotor performance should be evaluated within the identified region of interest. Within this region, the highest speeds occur at $S_{\text{mass}} = 1$, reflecting the nominal loading of the model. As S_{mass} increases, $\bar{v}$ declines because the additional load slows the system, eventually preventing forward motion once the legs can no longer generate sufficient torque to support and propel the body. Overall, stable locomotion and reliable speed outputs emerge only under combinations of frequency and load that preserve accurate joint trajectories, reinforcing the tracking error and amplitude limits identified in Fig. 7.6A and B.

A complementary measure of locomotor performance is the total forward distance d_{fwd}, computed as the net displacement along the x-axis over the duration of the simulation. Fig. 7.6D shows this distance as a function of f and S_{mass}. This measure reflects whether the model sustains propulsion or eventually stalls. For $S_{\text{mass}} \approx 1 - 10$, the forward distance increases with frequency. Notably, around $f \approx 4 - 5$ Hz, d_{fwd} becomes negative, indicating that the model ends the simulation behind its initial position. This does not imply backward walking; instead, the model follows a curved trajectory due to the rightward tilt observed earlier in Fig. 7.5B (top panel), and its final position lies behind the starting point. Thus, negative distances reflect lateral drift and curved motion rather than backward stepping. As S_{mass} increased beyond ~ 5, added load suppresses forward progression almost entirely, consistent with an inability of the legs to generate sufficient propulsive torque, an effect already evident in Fig. 7.5C.

Importantly, although the greatest forward distances are achieved at high frequencies, these conditions fall outside the region of interest because they correspond to large tracking errors and distorted joint amplitudes. Therefore, they do not represent meaningful or stable locomotion. Within the region of interest, the model achieves forward distances that are smaller in magnitude but dynamically coherent. Fig. 7.6E-F illustrate this contrast. Simulations outside the region of interest show increasingly erratic and curved trajectories as frequency rises or load increases, whereas the simulation marked by the blue cross ($f = 1$ Hz and $S_{\text{mass}} = 1$) exhibits a stable locomotor path. Thus, effective walking arises only under frequency–load combinations that preserve accurate joint-level dynamics.

Having established the baseline values for the active (MTU) and passive (joint) viscoelastic parameters, and demonstrated that these produce stable walking on flat terrain, we evaluate the whole-body model under more challenging conditions, *i.e.* uneven terrain, where interactions between the body and the environment require greater mechanical adaptability and stability. In the MuJoCo simulation environment, we generate a surface comprising a 15×15 grid of blocks with randomized heights, ranging from 0.01 cm and 0.35 cm. These values correspond to 1.2% and 43.75%, respectively, of the torso's centre of mass height in the insect model. The model is tasked with traversing this terrain using the

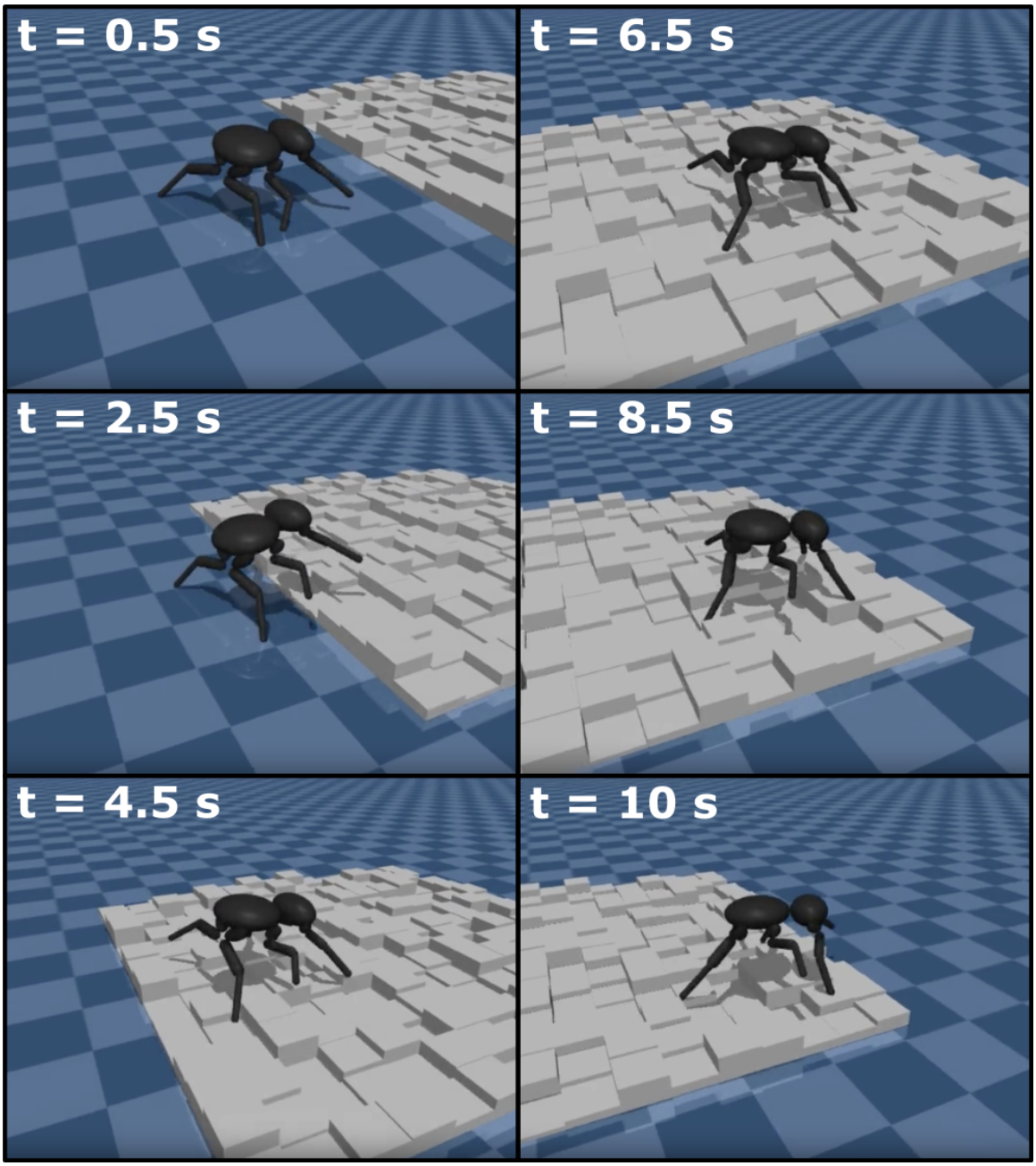

Figure 7.7: Whole-body insect model under uneven terrain. Frames extracted from a simulation of the insect model traversing uneven terrain. The frame times are given in the corner. Without any retuning of the controller, the model is able to produce stable walking gait, overcoming the introduced disturbances in the simulated terrain.

same control scheme and passive properties as in flat-level walking, and we assess whether successful traversal is achieved. Remarkably, the model is able to successfully walk under this uneven terrain despite the added environmental disturbances (see Fig. 7.7. Thus, a retuning of the controller is not required for this task. By using the unchanged controller and joint passive properties, the model reliably overcome induced disturbances in the terrain

and maintain a stable walking gait. Notably, this aligns with observations in real insects, where simple feedforward control can effectively traverse uneven terrain when paired with passively stabilising mechanics [71].

Additionally to this experiment, the model is tasked with traversing the simulated uneven terrain using three complementary parameter sweeps performed to isolate the contribution of the principal components governing joint behaviour. In each experiment, one parameter is varied while the remaining parameters are maintained at their baseline values, allowing the influence of each component to be evaluated independently. Fig. 7.8 shows the results from these experiments.

First, Fig. 7.8A analyses the contribution of passive joint mechanics by varying the passive stiffness-to-damping ratio, η_j, while maintaining the baseline active muscle properties and feedback. We modify the values of η_j for every joint by scaling the baseline values by 0.2 and 5 to examine how changes in passive joint mechanics influence locomotion in uneven terrain. Under the stiff condition ($\eta_j = 5\times$), the model barely moves, as the actuators lack sufficient power to overcome the increased passive resistance of the joints and drive the target joint trajectories needed to produce a stable gait. Consequently, the model fails to traverse the uneven terrain. Under the compliant condition ($\eta_j = 0.2\times$), the actuators retain sufficient power to produce a stable gait, but the reduced passive stiffness makes the joints more unstable, causing the model to progressively tilt away from the forward direction as it walks. Despite this lateral tilting, the compliant model is able to successfully traverse the uneven terrain, unlike the stiff condition. In both cases, the tripod-like coordination pattern is somewhat preserved.

Fig. 7.8B explores the influence of active muscle viscoelasticity by varying the active stiffness-to-damping ratio, η_a, while, similarly to the previous experiment, keeping both the passive joint mechanics and feedback controller fixed at their baseline values. As before, the parameter η_a is scaled by 0.2 and 5 to analyse the contribution of the active mechanical properties of the MTUs to locomotor behaviour. Under the compliant condition ($\eta_a = 0.2\times$), the MTUs generate insufficient power to drive the joints through their target trajectories, such that the joint motion is only partially executed. As a consequence, the model fails to properly perform the tripod gait and is unable to traverse the uneven terrain. Under the stiff condition ($\eta_a = 5\times$), the MTUs instead generate sufficient power to drive the joints, but this increased actuator dominance causes the joints to lose their flexibility and behave in a rigid manner. Despite this rigidity, the model in this condition is able to successfully traverse the uneven terrain, although not in a straight forward direction. Unlike excessive passive joint stiffness, excessive active muscle stiffness does not prevent successful locomotion, whereas insufficient active power does.

Finally, Fig. 7.8C examines the role of feedback control by uniformly scaling the pro-

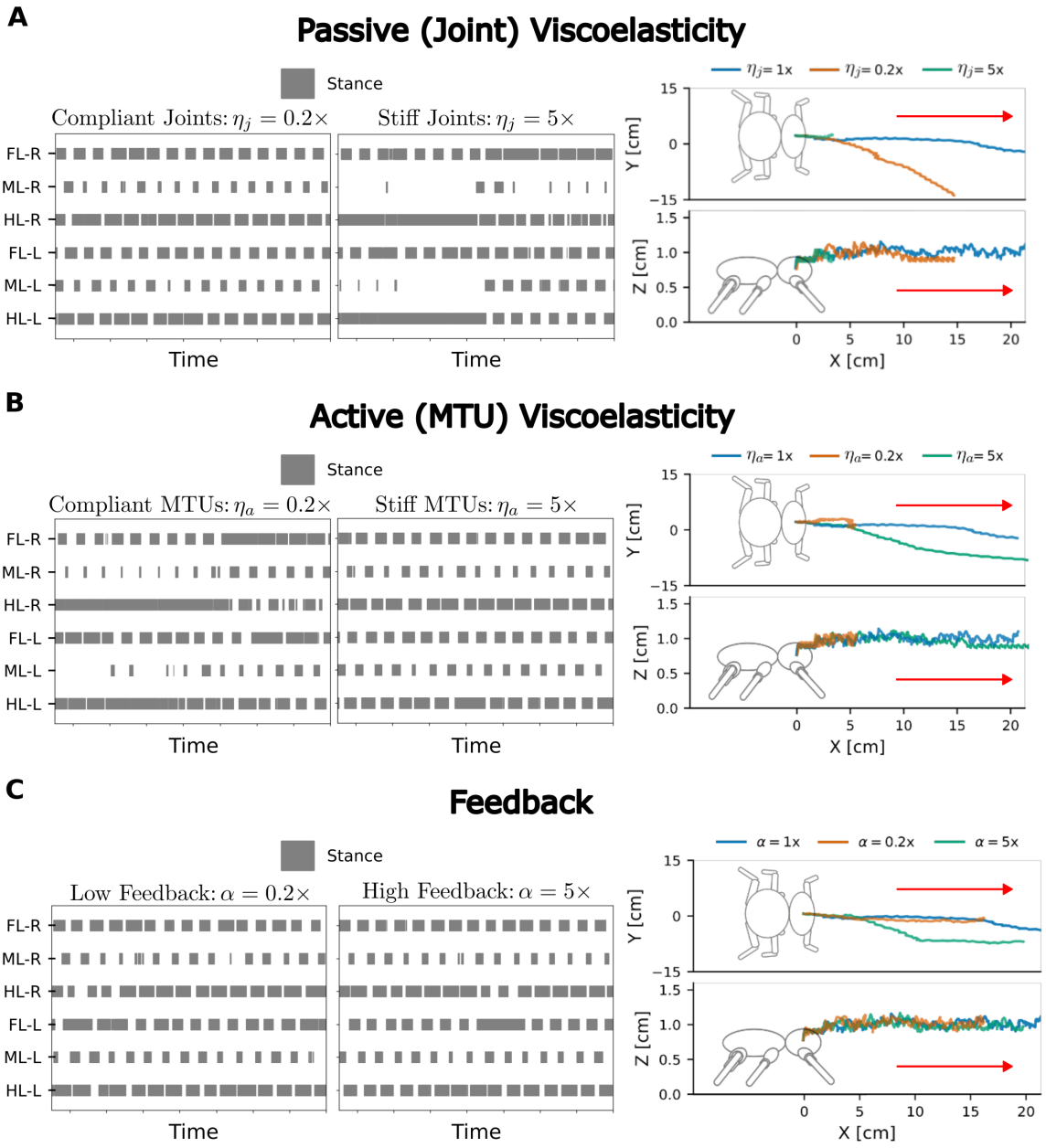

Figure 7.8: Sensitivity of uneven-terrain locomotion to passive joint viscoelasticity, active muscle viscoelasticity, and feedback gain. Each panel varies one principal component of joint behaviour while holding the others at baseline. Gait diagrams (left) show stance phases (grey) for all six legs at the two values tested; XY (top right) and XZ (bottom right) trajectories compare baseline (1×, blue) against reduced (0.2×, orange) and increased (5×, green) values. (A) Passive stiffness-to-damping ratio η_j scaled at every joint. (B) Active stiffness-to-damping ratio η_a scaled at every joint. (C) Feedback gain scaled uniformly across all joints via α, jointly modulating K_p and K_d.

portional, K_p, and derivative, K_d, gains of the joint controllers through the parameter α. Rather than modifying individual joints independently, the feedback gains of all joints are

scaled by the same factor relative to the baseline controller (see Fig. 7.4). Values of $\alpha = 0.2$ and $\alpha = 5$ are considered, corresponding to weaker and stronger feedback control. Of the three sweeps, this one produces the smallest effect on gait structure, with stance patterns remaining highly similar between the low- and high-feedback conditions. The low-feedback condition closely tracks the baseline trajectory, whereas the high-feedback condition produces a moderate but consistent lateral drift, smaller in magnitude than the drift observed under increased active stiffness in Fig. 7.8A-B.

These three sweeps indicate that successful traversal of uneven terrain depends primarily on whether the actuators retain sufficient power to drive the joints against the passive resistance, rather than on the qualitative structure of the gait itself. Failure to traverse the terrain occurs specifically when this power balance is disrupted in a way that prevents the joints from executing their target trajectories, as observed under excessively stiff passive joints (Fig. 7.8A) and under excessively compliant MTUs (Fig. 7.8B). By contrast, when the actuators retain adequate power to drive the joints, the model is able to traverse the terrain even when this is accompanied by secondary mechanical side effects, such as lateral tilting under compliant joints or increased joint rigidity under stiff MTUs. Notably, in all conditions tested, including the failure cases, the model preserves a broadly tripod-like coordination pattern, suggesting that the underlying gait timing is largely decoupled from the passive and active viscoelastic properties of the joints, and that locomotor failure instead arises from a mechanical inability to physically realise the intended joint trajectories. Feedback gain, in comparison, has the mildest effect of the three parameters on both gait structure and heading stability, consistent with its role in fine-tuning trajectory tracking rather than governing the fundamental power balance between active and passive joint properties.

While this provides initial evidence that joint passive viscoelasticity contributes to locomotor robustness, a comprehensive evaluation of such robustness is necessary, including different task conditions, and quantitative performance metrics. These experiments are thought to be done in future work.

7.3 Discussion

This chapter evaluated the performance of a whole-body model whose limbs are built from the third level of modelling hierarchy (physics-based joint model). We began by examining a three-joint leg, in isolation, with the rest of the body fixed in space. Each joint had a degree of freedom, and was actuated by a pair of antagonistic MTUs, in contrast to our model analysed in Chapter 5 where only one MTU was present. The purpose of this analysis was to determine if the multi-joint leg could reproduce realistic insect-like trajectories, and as to

test whether the dynamical regimes arising from the interaction between active and passive properties of the system (first identified in Section 6.2.2), were preserved. We showed that the multi-joint limb successfully reproduced realistic trajectories when the MTU activation profiles are coordinated and optimised for that purpose. Moreover, the dynamical regimes observed in the single joint analysis re-emerged in the multi-joint setting.

To ground the insect model in biological realism, we used published data from dung beetle models for its mechanical configuration [11], as well as walking gait trajectories, as reference [77, 108]. We identified MTU activation profiles for our multi-joint limb that closely reproduced these experimental trajectories. The ability of the limb to achieve such trajectories demonstrates that the physics-based single joint framework scales effectively to a full limb and can serve as a reusable building block. This scalability is significant because it shows that the same limb mechanics can support different tasks by appropriately modifying muscle activation patterns. Thus, showing the generality and versatility of the framework.

Building on this, we revisited the three dynamical regimes identified in chapter 6, where the interplay between MTU active forces and joint passive forces shaped the behaviour of a single joint within our nondimensional framework. A key question was whether these regimes would also manifest in the physics-based framework, both in single and multi-joint configurations, when driven by activation profiles more complex than idealised sine waves. From our simulations, we observed that these regimes indeed reappear in a more mechanically detailed setting, indicating that they arise robustly from the intrinsic viscoelastic properties and muscle-tendon mechanics, rather than from the particular temporal structure of the activation signal. This strengthens the validity of the nondimensional framework and points out that passive and geometric properties largely determine the operating regime of the limb, with muscle activation acting primarily to modulate its behaviour.

Crucially, we find that experimentally derived passive FeTi joint parameters place the system close to the transition between Regime I and Regime II across both nondimensional and physics-based models. This transition represents a balance point at which passive stiffness is sufficient to stabilise joint motion, yet not so dominant to suppress the influence of active muscle input. From a functional perspective, this suggests that insect joints are mechanically tuned to operate close to a region where passive viscoelastic forces stabilise joint motion without dominating it. In this region, changes in muscle activation remain effective in shaping joint dynamics, and therefore, there is a close coupling between passive joint mechanics and active control. Taken together, these results support the view that animals likely coordinate activation timing and amplitude to work with the mechanical biases of their joints, achieving efficient and stable movement by exploiting, rather than compensating for, the structure of the passive dynamics.

Having established that the multi-joint limb could reproduce realistic joint trajectories in isolation, and that its behaviour followed the same regimes identified earlier, it was natural to ask whether these capabilities would extend to whole-body locomotion. We therefore tested the model in an unfixed-body configuration, where limb and body dynamics interact bidirectionally. However, under these conditions the model failed to produce stable walking. Therefore, control strategies optimised in a fixed-body context do not readily generalise to whole-body locomotion; instead, effective control appears to be highly context-dependent. This indicates that muscle–joint control cannot be fully understood in isolation. Instead, it must be analysed within the complete neuromechanical context in which joint, body, and environmental dynamics interact.

To enable walking in our insect model, we generated joint-level target trajectories that were temporally coordinated to produce a tripod-like gait, as well as implemented a simple PD controller at each joint to track these targets. These two elements allowed the insect model to achieve stable walking gait, provided two conditions are met: the passive properties of the joints are appropriately tuned, and the target trajectories exhibit feasible inter-joint coordination. Thus, the substantial contribution of the mechanical structure of the body to locomotion becomes evident from this result. Even with minimal control, the viscoelastic properties of the joints and the geometric arrangement of the limb support key locomotor functions. The joints naturally sustain body weight during stance, and store and release elastic energy to assist swing to smooth motion and stabilise gait. In this context, the mechanical properties thus reduce the burden on neural control as previously described in [89].

If body mechanics can accomplish so much of the locomotor task, under what conditions does more complex neural control become necessary? Most probable scenarios include perturbations such as uneven terrain, increased load, or rapid adjustments in gait direction and speed, where passive mechanics alone cannot compensate for sudden changes. In these cases, neural circuits would need to intervene to generate corrective torques, adjust inter-joint timing, or modulate activation amplitudes to maintain stability and forward progression. Although our simulations do not yet include these perturbations, it remains an interesting question to what extent a simple control scheme can support stable locomotion under such conditions. For now, the insect model demonstrates that the intrinsic mechanics of the body, combined with minimal feedback, are sufficient to carry out the core locomotor functions under ideal conditions.

A notable observation is that locomotor stability is constrained by the combined limits of joint mechanics and the PD controller. Our simulations revealed an operational regime where the insect model walks most reliably at target frequencies of approximately $f = 1{-}2\,\mathrm{Hz}$ and scaled body loads of $S_{\mathrm{mass}} = 1{-}10$. In this regime, the PD controller

can track the joint trajectories with minimal error and phase lag is small enough to maintain coordinated motion. In addition, the torque demands remain within the mechanical capacity of the legs, allowing the passive joint mechanics to support body weight while enabling effective propulsion. Outside this operational window, high frequencies produce phase delays that the controller cannot fully compensate and high loads exceed the torque-generating capacity of the joints. In contrast, at low frequencies, the reduced contribution of dynamic forces limits forward progression. Interestingly, the frequency–load range that produces stable tripod gait in the model aligns closely with stepping frequencies observed in walking insects [18, 31, 72]. These insects may naturally exploit a mechanically favourable operational regime. This regime arises from the interplay between passive mechanics and minimal feedback, which defines an optimal window in which the intrinsic properties of the limb can accomplish locomotor tasks with little neural intervention. Such interplay implies that evolution may have tuned passive joint properties not only to reduce energetic cost but also to expand the conditions under which simple, low-level feedback is sufficient for robust and coordinated locomotion.

Beyond generating a single stable gait, our insect model establishes a platform to explore how the same set of compliant antagonistic joints could be repurposed for multiple locomotor behaviours. This approach underscores the potential for modularity and mechanical generality. Because passive joint properties shape limb dynamics in predictable ways, it is reasonable to hypothesise that the same mechanical structure could support different movement patterns with minimal changes to the controller. For example, future studies could investigate how varying target trajectories, oscillation frequencies, or loading conditions might allow the system to perform additional tasks, such as jumping, climbing, or manipulating objects while moving, without redesigning the joints. Our model showed preliminary evidence of versatility by producing stable walking under uneven terrain. However, the flexibility of the model needs to be further investigated. Such flexibility reflects the multi-tasking principle in animal locomotion, where organisms routinely use the same musculoskeletal components across different behaviours to achieve multifunctionality. Our framework thus provides a concrete tool to examine how passive mechanics and simple joint-level feedback may facilitate this versatility, and to quantify the operational limits and constraints of multi-task locomotion in future work.

Chapter 8

Discussion

This chapter concludes the thesis by summarising its main contributions and situating them within the research questions outlined in Section 1.1. It briefly restates the chapter-specific results to clarify how they collectively address those questions.

The thesis seeks to advance our understanding of how joint torque and motion emerge from the coupling between active muscle-tendon dynamics and passive joint viscoelasticity. The work is organised around three research questions. First, how do active muscle–tendon dynamics and passive joint viscoelasticity interact to shape joint torque generation and motion? Second, under what conditions do passive joint mechanics dominate, stabilise, or meaningfully constrain joint motion, and to what extent can intrinsic joint mechanics themselves structure movement without requiring complex control schemes? Third, how can insights into passive joint dynamics be applied to the design and control of robotic joints?

These questions rest on the central claim that passive joint structures are key participants in movement rather than mere "background" stabilisers; a claim grounded here in insect-scale joints, but that extends qualitatively to larger animals, including humans, where passive structures remain key mechanical participants in movement, albeit with a shift toward series elasticity, and greater reliance on active neural control as gravitational loading and limb inertia increase with body size. To address them, the thesis adopts a hierarchical modelling approach that progressively increases biomechanical complexity while maintaining a consistent emphasis on the same mechanical interface: the transformation of time-varying muscle actuation into joint torque, joint motion, and mechanically feasible limb behaviour. By examining this transformation across isolated joints, multi-joint limbs, and whole-body models, the thesis evaluates whether the functional role of passive joint mechanics persists across scales and contexts.

8.1 Active-Passive Interactions in Joint Torque Generation and Motion

One of the achievements of our joint models presented in Chapter 5 was reproducing realistic extension-flexion trajectories consistent with experimental observations in insects [3]. A simplified model of a joint, comprising a viscoelastic muscle-tendon unit, a viscoelastic joint, appropriate geometry, driven by feedforward activation signals was sufficient to generate plausible movement. This demonstrates that intrinsic mechanical interactions between active and passive elements can generate structured joint motion in the absence of sensory feedback and neural control mechanisms. However, matching the model output to the single-spike experimental condition alone was not sufficient to distinguish between a fixed and an adaptive activation time constant, since both can produce plausible trajectories under that condition. This limitation became apparent when stimulation conditions were varied. Under repeated high-frequency stimulation (five spikes at 20 Hz), a fixed activation time constant failed to simultaneously reproduce both the single-spike and multi-spike joint responses (Sections 5.3.1 and 5.3.2).

This discrepancy points to a feature inherent to muscle dynamics: force generation depends on activation and deformation history [4, 27, 67]. In the models, this history dependence becomes evident when repeated or high-frequency stimulation produces slower relaxation and sustained force output that cannot be captured by a single, fixed activation time constant. The adaptive activation mechanism introduced in Section 5.3.3 provides a concrete representation of this effect by allowing activation dynamics to vary with stimulation context. Importantly, this mechanism does not alter passive joint properties; instead, it changes the time course of muscle force entering the joint. As a result, identical passive mechanics can produce qualitatively different joint trajectories depending on prior activation, highlighting that joint behaviour emerges from the interaction between passive joint viscoelastic filtering and history-dependent muscle force generation.

In contrast, when active muscle input is removed, the models show that passive joint elements alone are sufficient to generate structured relaxation behaviour, including return trajectories. In both Sections 5.3.1 and 6.2.1, the temporal profile of this passive motion was governed by joint viscoelastic parameters, with stiffness-dominated joints producing faster returns and viscosity joints producing slower, more gradual relaxation. In this case, the timing of passive motion is set by joint mechanics, independent of activation history. These findings support experimental descriptions in the literature about passive tissues shaping joint return dynamics [4, 63]. Importantly, the models sharpen this interpretation by showing that passive joint mechanics do not simply oppose motion, but instead define a baseline dynamical template that determines how the joint evolves once active force

generation ceases.

Therefore, there is a division of labour between passive joint mechanics and muscle activation. Passive mechanics establish the intrinsic temporal structure of joint motion, while muscle dynamics modulate how and when this structure is engaged. The interaction between these two processes determines the resulting joint trajectory. In biological systems, this interaction is further regulated by inhibitory mechanisms, such as common inhibitory motor neurones, which effectively shape muscle activation without altering the underlying joint mechanics [85, 125]. Although such inhibitory mechanisms are not modelled here, the present results provide a mechanical context in which their functional role can be interpreted. Inhibition can modulate how and when muscle forces act, while the passive joint continues to determine the timing and stability of the resulting joint motion.

8.2 Regime-dependent Role of Passive Joint Mechanics

The results above clarify how active and passive mechanics interact to generate motion. However, they do not yet totally explain when passive viscoelasticity stabilise motion and when they limit it. Chapter 6 addresses this by transition from mechanism demonstration to mechanism organisation, identifying how joint behaviour is structured by passive properties across operating regimes. A key step in enabling this transition was the formulation of a nondimensional representation of the joints equations of motion. To the best of our knowledge, this is a novel interpretation of muscle-joint dynamics. By using the nondimensional framework, joint behaviour can be analysed in a unified parameter space where changes in dynamics reflect genuine shifts in the balance between active and passive mechanisms, without worrying about particular parameter choices.

The results obtained from the nondimensional model revealed distinct emergent operating regimes. As observed in Section 6.2.1, passive joint mechanics give rise to qualitatively different relaxation behaviours, including overdamped and underdamped responses, depending on the relative contributions of stiffness and damping. When rhythmic, antagonistic actuation is introduced, these passive properties continue to structure joint behaviour by determining whether active input is effectively transmitted, progressively attenuated, or largely suppressed. We compared these behavioural regimes to a filter analogy (Section 6.2.2), which is also observed in other biological systems [30]. A nondimensional framework allow these regimes to be identified and compared systematically across excitation frequencies, loading conditions, and actuations strengths.

By analysing joint behaviour in a nondimensional framework, the model provides a principled answer to when passive mechanics stabilise motion and when they constrain it. In

regimes where passive stiffness is low and passive damping dominates, joint motion remains stable and responsive to actuation. In contrast, when passive stiffness is too high relative to passive damping, the response becomes increasingly constrained and active torques need to increase to compensate for this. This implies that in biological systems, passive joint mechanics must operate within a specific region of the regime space to support functional joint motion, as discussed in [104]. And, therefore, the viscoelastic properties of biological joints may be naturally tuned to operate within these mechanically favourable regimes. However, this needs further investigation across species and joint types. From a regime perspective, passive joint mechanics act as modulator of joint motion, determining when and how muscle actuation translates into movement.

The regime-based interpretation is closely aligned with earlier work by Sutton *et al.* [105]. Expressed in a nondimensional number, they showed that limb behaviour can be organised into mechanical regimes of limb length and cycle period in which properties such as elasticity, viscosity inertia, and gravitational load, dominate. Our nondimensional framework makes an analogous move but at a different level of description. Instead of classifying regimes by which external force component dominates, it classifies regimes by how passive joint impedance (stiffness-to-damping, inertia, and load) shapes the input–output transformation from muscle actuation to joint motion. In this sense, Sutton's work provide a broader scaling perspective, while the present framework complements it by tying regime shifts directly to muscle-driven joint performance limits and to how passive viscoelasticy structures the dynamic range of motion.

If joint behaviour is organised into mechanical regimes under symmetric actuation, what happens when actuation itself is asymmetric? As discussed earlier, biological joints operate with muscles that differ in muscle size and strength. The analysis in Section 6.2.3 show that passive joint properties can compensate for imbalances posed by asymmetric actuators. When one of the actuators is stronger than its antagonist counterpart, the dynamic range of the joint becomes directionally biased and generally reduced. Asymmetry can be beneficial in different task contexts, *e.g.* movement with needed directional biases and load bearing, but introduces inherent mobility costs that can be mitigated by passive mechanics or loading conditions. The results show that viscoelastic joints operating in a regime where passive stiffness is on the same order as its damping, or up to an order of magnitude larger ($1 < \eta_j < 10$), can maintain directional bias without compromising dynamic range. In this regime, passive joints support robust movement when actuation is limited or uneven. This highlights a functional role for passive viscoelasticity as a mechanical regulariser and represents a key contribution of the nondimensional-MTU joint model developed in this thesis.

Although this regime interpretation is derived from isolated joint analyses, the same regime structure persists under inter-joint coupling (Section 7.2.2) and whole-body dy-

namics, where joint mechanics interact with body dynamics, ground contact, and inter-leg coupling. In this broader context, joint loading becomes an additional and unavoidable factor shaping joint behaviour. Despite this increased complexity, Section 7.2.3 shows that stable and functional whole-body movement is most likely when joints operate near the same viscoelastic regime ($1 < \eta_j < 10$) that mitigate the consequences of asymmetric actuation. This suggests that these regimes reflect intrinsic properties of coupled muscle–joint mechanics rather than artefacts of simplified models.

At the whole-body level, the viscoelastic regime plays a critical organising role. Passive joint stiffness and damping help regulate timing and smooth interactions with the ground, reducing sensitivity to disturbances and coordination errors across limbs. At the same time, because passive mechanics do not dominate, active input retains enough capacity to adapt joint motion to task demands and environmental constraints, as demonstrated in Fig. 7.4 and Fig. 7.5. This balance is essential in locomotion, where joints must simultaneously support body weight, generate propulsion, and coordinate with other joints. When joints operate outside this regime, either passive mechanics are too weak to stabilise whole-body dynamics or too strong to permit effective control, leading to loss of coordination or failure to sustain movement. The persistence of this pattern across isolated joints, limbs, and whole-body models supports the interpretation that the balanced viscoelastic regime ($1 < \eta_j < 10$), where passive mechanics provide sufficient restoring force without dominating active contributions, reflects an intrinsic property of coupled muscle–joint mechanics, rather than a feature specific to simplified conditions.

8.3 Passive Joint Mechanics in Robotic Joints

In biological systems, such a balance is critical because it allows simple control to shape motion while passive mechanics provide predictable timing, intrinsic stabilisation, and load tolerance. At the whole-body level, this balance is particularly important because locomotion is not only about generating joint trajectories, but also about maintaining body support and coordinating motion across multiple joints and legs [21, 29, 122]. Indeed, Section 7.2.3 shows that stable and coordinated locomotion under low-level joint feedback control becomes feasible when passive joint properties are tuned to provide sufficient intrinsic stability. At the same time, appropriately tuned passive mechanics allow muscle-tendon actuation to modulate joint motion and adapt to changes in loading and contact conditions. These results help explain how robust whole-body movement can emerge from low-complexity control, provided that the mechanical system operates within a favourable region of the dynamical regime space, where passive stability and active modulation are naturally aligned.

The same principles are therefore directly relevant to engineering applications and provide a route to simplifying control through mechanical design. As demonstrated in legged robotic systems [47, 71, 98], limb compliance can align the natural dynamics of the body with the mechanical requirements of locomotion, including body support, stability, and stride timing. In this context, passive joint stiffness and damping are key design variables that determine the operating regime of the limb. Our results show that selecting these properties appropriately allows performance to be leveraged systematically, rather than tuned empirically. When joints are tuned within a balanced viscoelastic regime, simple feedback control can be effective because the body is already mechanically stabilised and does not demand high control bandwidth. This further explains why control strategies that succeed in constrained settings (*i.e.* fixed-body) do not automatically transfer to free-body locomotion (Section 7.2.2). Once body dynamics and ground contact are included, stable behaviour emerges only when passive support and active modulation coexist within a favourable mechanical regime.

From this perspective, several practical design principles follow. First, the desired operating regime should be identified on the locomotor requirements, expecting loading conditions, and characteristic movement frequencies. Second, passive viscoelasticity should be selected so that the joint remains both stable and responsive, avoiding overly compliant designs that amplify disturbances as well as excessively stiff or heavily damped designs that suppress motion and introduce tracking lag. Third, controller bandwidth and feedback gains must be matched to the mechanical impedance of the joint, since feedback cannot restore joint motion or timing that has already been attenuated or delayed by passive joint mechanics. Finally, performance should be evaluated across ranges of different operating conditions, such as variations in load and excitation frequency, as changes in these conditions can shift the system between dynamical regimes and thereby define the limits of stable locomotion.

Whereas leg compliance is often tuned empirically due to limited theoretical guidance [71, 116], the regime-based analysis presented here provides a principled framework for selecting joint viscoelastic properties. By targeting specific dynamical regimes, joint mechanics can be systematically chosen to support stable and efficient locomotion, reducing reliance on heuristic design and extensive trial-and-error. These guidelines follow directly from the observed regime-dependent behaviour across joint, limb, and whole-body contexts.

In conclusion, the role of passive joint properties revealed by this work can be understood in three complementary ways. First, passive properties are shown to be generative: they can complete movement cycles and provide reliable return dynamics even when neural drive is sparse. This supports the view that passive structures contribute to defining movement primitives at the joint level. Second, passive properties are shown to be organising: they

structure dynamical regimes that determine whether joints behave as responsive actuators, balanced filters, or heavily attenuated systems. In this sense, passive mechanics provide a predictive framework joint behaviour across different conditions. Third, passive properties are shown to be scalable and consequential: the same regime structure persists at the level of limbs and whole bodies, influencing locomotor stability and defining performance limits under low-level control. Passive joint mechanics thus matter not only for isolated kinematics, but also for whole-body functional robustness.

8.4 Limitations and Future Directions

The hierarchical modelling framework developed here provides a principled way to analyse how passive joint viscoelasticity shapes joint and whole-body dynamics, and to identify mechanically favourable operating regimes. While this approach enables the identification of effective passive properties (see Fig. 5.9), these properties represent aggregated approximations of the combined muscle-joint system. A remaining challenge is therefore to characterise the biological and structural origins of these effective viscoelastic properties. That is, to determine which specific tissues and structures contribute to the observed stiffness and damping in the system.

In the present modelling framework, joint stiffness and damping are represented using linear approximations, as discussed in Section 3.6. This choice reflects the goal of identifying the dominant dynamical structure governing joint and whole-body behaviour. The linear model captures the essential time scales, stability properties, and frequency-dependent responses that organise joint dynamics, while enabling clear identification of distinct operating regimes. Although biological joints exhibit additional nonlinear and state-dependent behaviour [32, 126, 127], we hypothesise that such effects primarily modulate the boundaries of the viscoelastic regimes rather than alter their fundamental organisation. Characterising these nonlinear contributions in greater detail thus represents an important direction for future work.

A related limitation concerns the representation of the force-length relationship and its geometric coupling to joint angle. In Hill-type muscle models, active force generation is maximal at an optimal muscle length, which corresponds to a specific joint angle through the moment arm geometry. In this thesis, the length L_t captures an activation-dependence of the muscle's operating point, but the bell-shaped force-length optimum characteristic of the Hill-type relationship (see Fig. 3.3) is not explicitly represented. Consequently, the coupling between optimal muscle length and optimal joint angle, which determines how force varies across the joint range, is not captured. In an antagonistic muscle arrangement, where each muscle may have a distinct optimal muscle length and therefore a distinct joint

angle of peak force production, this omission means that the model does not represent the full force-generating asymmetry that arises from geometric differences between muscles. Incorporating this feature into the active element, would be a natural extension to address this.

A further limitation of this work concerns the simplified treatment of muscle activation and control. Muscle activation patterns are either prescribed (Section 7.2.2) or regulated through local joint-level feedback (Section 7.2.3). We do not model neural circuitry explicitly. Consequently, the modelling framework does not address how rhythmic activation patterns are generated, coordinated across joints and legs, or adapted in response to sensory feedback. In biological systems, these functions are commonly associated with central pattern generators (CPGs), descending feedforward commands, and reflex pathways that modulate timing, amplitude, and inter-muscle coordination depending on the task and context. Animals are known to rely on a combination of feedforward and feedback mechanisms to produce stable and flexible movement [65]. Indeed, one of the biggest open questions in adaptive locomotion concerns how these feedforward and feedback control mechanisms interact with the biomechanics of the body. Incorporating such control elements into the present modelling framework would therefore enable systematic investigation of how neural dynamics operate within, and exploit, the mechanically defined regimes identified here.

Having said this, several next steps follow naturally from this work. The first extension of this work is to use a broader range of joint behaviours to further characterise the active and passive stiffness and damping of biological joints beyond those considered here. Integrating experimental data from joint operating under different functional conditions, such as varying postures, loading regimes, and movement speeds would allow the effective viscoelastic properties of the muscle-joint system to be inferred from observed dynamics. Moreover, applying this approach to larger joints and heavier animals would be particularly informative, as increased inertia may reveal how the relative contributions of active and passive mechanics shift with scale, and whether similar regime structures persist when inertial effects become comparable to or exceed viscoelastic forces.

A second important direction is to extend the framework to higher levels of behaviour by testing multi-task performance within a fixed mechanical system. Instead of retuning passive joint properties for each behaviour, body morphology and joint mechanics can be treated as fixed constraints, while control is varied through changes in muscle activation timing, coordination, and co-activation. This approach reflects the way biological systems reuse the same mechanical substrate across multiple tasks. Initial steps in this direction are already being explored in the whole-body insect model, as illustrated by preliminary results of locomotion over uneven terrain (see Fig. 7.7). Beyond locomotion, manipulation tasks are of particular interest. Behaviours such as dung beetle ball-rolling [76], which

require coordinated load handling and force redirection rather than purely periodic motion, provide a compelling test case for assessing whether our modelling framework can support both locomotor and manipulative functions.

Finally, from a robotics perspective, the most direct validation of the proposed principles lies in hardware implementation. A compliant joint prototype with adjustable stiffness and damping could be evaluated under controlled frequencies, loads, and actuation asymmetries to reproduce the predicted operating regimes and stability limits. Extending this approach to variable-stiffness actuators would further allow the operating point of limb to be shifted in response to changing task demands without altering morphology or substantially increasing control complexity. Such platforms would not only test the regime-based framework experimentally, but also demonstrate how multi-task locomotion and adaptability can be achieved within a single mechanical architecture.

References

[1] I. Abadía, A. Bruel, G. Courtine, A. J. Ijspeert, E. Ros, and N. R. Luque. "A neuromechanics solution for adjustable robot compliance and accuracy". In: *Science Robotics* 10.98 (2025). ISSN: 24709476. DOI: 10.1126/scirobotics.adp2356.

[2] B. C. Abbott and D. R. Wilkie. "The relation between velocity of shortening and the tension-length curve of skeletal muscle". In: *The Journal of Physiology* 120.1-2 (Apr. 1953), pp. 214–223. ISSN: 1469-7793. DOI: 10.1113/JPHYSIOL.1953.SP004886.

[3] J. M. Ache and T. Matheson. "Passive joint forces are tuned to limb use in insects and drive movements without motor activity". In: *Current Biology* 23.15 (2013), pp. 1418–1426. ISSN: 09609822. DOI: 10.1016/j.cub.2013.06.024.

[4] Jan M. Ache and Thomas Matheson. "Passive resting state and history of antagonist muscle activity shape active extensions in an insect limb". In: *Journal of Neurophysiology* 107.10 (May 2012), pp. 2756–2768. ISSN: 00223077. DOI: 10.1152/jn.01072.2011.

[5] S. Agrawal and J. C. Tuthill. "The two body problem: proprioception and motor control across the metamorphic divide". In: *Current opinion in neurobiology* 74 (June 2022), p. 102546. ISSN: 18736882. DOI: 10.1016/J.CONB.2022.102546.

[6] M. F. Ahmad, N. A. M. Isa, W. H. Lim, and K. M. Ang. "Differential evolution: A recent review based on state-of-the-art works". In: *Alexandria Engineering Journal* 61.5 (May 2022), pp. 3831–3872. ISSN: 1110-0168. DOI: 10.1016/J.AEJ.2021.09.013.

[7] R. M. Alexander. "Energy-Saving Mechanisms in Walking and Running". In: *Journal of Experimental Biology* 160.1 (1991), pp. 55–69. ISSN: 0022-0949. DOI: 10.1242/JEB.160.1.55.

[8] R. M. Alexander and H. C. Bennet-Clark. "Storage of elastic strain energy in muscle and other tissues". In: *Nature* 265.5590 (1977), pp. 114–117. ISSN: 1476-4687. DOI: 10.1038/265114a0.

[9] K. N. An, Y. Ueba, E. Y. Chao, W. P. Cooney, and R. L. Linscheid. "Tendon excursion and moment arm of index finger muscles". In: *Journal of Biomechanics* 16.6 (Jan. 1983), pp. 419–425. ISSN: 0021-9290. DOI: 10.1016/0021-9290(83)90074-X.

[10] H. C. Bennet Clark. "The energetics of the jump of the locust Schistocerca gregaria". In: *Journal of Experimental Biology* 63.1 (Aug. 1975), pp. 53–83. ISSN: 0022-0949. DOI: 10.1242/JEB.63.1.53.

[11] P. Billeschou, N. N. Bijma, L. B. Larsen, S. N. Gorb, J. C. Larsen, and P. Manoonpong. "Framework for Developing Bio-Inspired Morphologies for Walking Robots". In: *Applied Sciences 2020, Vol. 10,* 10.19 (Oct. 2020), pp. 1–20. ISSN: 2076-3417. DOI: 10.3390/APP10196986.

[12] B. I. Binder-Markey and W. M. Murray. "Incorporating the length-dependent passive-force generating muscle properties of the extrinsic finger muscles into a wrist and finger biomechanical musculoskeletal model". In: *Journal of Biomechanics* 61 (Aug. 2017), pp. 250–257. ISSN: 0021-9290. DOI: 10.1016/J.JBIOMECH.2017.06.026.

[13] *Blender - The Free and Open Source 3D Creation Software*. URL: https://www.blender.org/.

[14] J. H. Boyle, S. Berri, and N. Cohen. "Gait modulation in C. elegans: An integrated neuromechanical model". In: *Frontiers in Computational Neuroscience* 6.10 (2012), p. 17123. ISSN: 16625188. DOI: 10.3389/fncom.2012.00010.

[15] M. Bresadola. "Animal Electricity at the End of the Eighteenth Century: The Many Facets of a Great Scientific Controversy". In: *Journal of the History of the Neurosciences* 17.1 (Jan. 2008), pp. 8–32. ISSN: 0964704X. DOI: 10.1080/09647040600764787.

[16] R. E. Burke. "Motor unit types: functional specializations in motor control". In: *Trends in Neurosciences* 3.11 (Nov. 1980), pp. 255–258. ISSN: 0166-2236. DOI: 10.1016/0166-2236(80)90095-8.

[17] R. E. Burke, P. Rudomin, and F. E. Zajac. "The effect of activation history on tension production by individual muscle units". In: *Brain Research* 109.3 (June 1976), pp. 515–529. ISSN: 0006-8993. DOI: 10.1016/0006-8993(76)90031-7.

[18] M. D. Burns. "The Control of Walking in OrthopteraI. Leg Movements in Normal Walking". In: *Journal of Experimental Biology* 58.1 (Feb. 1973), pp. 45–58. ISSN: 0022-0949. DOI: 10.1242/JEB.58.1.45.

[19] M. Burrows and G. Morris. "The kinematics and neural control of high-speed kicking movements in the locust". In: *Journal of Experimental Biology* 204.20 (Oct. 2001), pp. 3471–3481. ISSN: 0022-0949. DOI: 10.1242/JEB.204.20.3471.

[20] M. Burrows, A. H.D. Watson, and D. Brunn. "Physiological and Ultrastructural Characterization of a Central Synaptic Connection between Identified Motor Neurons in the Locust". In: *European Journal of Neuroscience* 1.2 (Mar. 1989), pp. 111–126. ISSN: 1460-9568. DOI: 10.1111/J.1460-9568.1989.TB00778.X.

[21] R. F. Chapman. "Legs and locomotion". In: *The Insects* (June 1998), pp. 151–184. DOI: 10.1017/CBO9780511818202.009.

[22] D. G. Cochrane, H. Y. Elder, and P. N. Usherwood. "Physiology and ultrastructure of phasic and tonic skeletal muscle fibres in the locust, Schistocerca gregaria". In: *Journal of Cell Science* 10.2 (Mar. 1972), pp. 419–441. ISSN: 0021-9533. DOI: 10.1242/JCS.10.2.419.

[23] Alberto N. Conejo. "Non-dimensionalization of Differential Equations". In: *Fundamentals of Dimensional Analysis* (2021), pp. 347–378. DOI: 10.1007/978-981-16-1602-0{_}13.

[24] H. Cruse and Ch Bartling. "Movement of joint angles in the legs of a walking insect, Carausius morosus". In: *Journal of Insect Physiology* 41.9 (Sept. 1995), pp. 761–771. ISSN: 0022-1910. DOI: 10.1016/0022-1910(95)00032-P.

[25] H. Cruse, T. Kindermann, M. Schumm, J. Dean, and J. Schmitz. "Walknet—a biologically inspired network to control six-legged walking". In: *Neural Networks* 11.7-8 (Oct. 1998), pp. 1435–1447. ISSN: 0893-6080. DOI: 10.1016/S0893-6080(98)00067-7.

[26] M. A. Daley, G. Felix, and A. A. Biewener. "Running stability is enhanced by a proximo-distal gradient in joint neuromechanical control". In: *Journal of Experimental Biology* 210.3 (Feb. 2007), pp. 383–394. ISSN: 0022-0949. DOI: 10.1242/JEB.02668.

[27] M. A. Daley, A. Voloshina, and A. A. Biewener. "The role of intrinsic muscle mechanics in the neuromuscular control of stable running in the guinea fowl". In: *Journal of*

Physiology 587.11 (2009), pp. 2693–2707. ISSN: 00223751. DOI: 10.1113/JPHYSIOL.2009.171017.

[28] C. J. Dallmann, V. Dürr, and J. Schmitz. "Joint torques in a freely walking insect reveal distinct functions of leg joints in propulsion and posture control". In: *Proceedings of the Royal Society B: Biological Sciences* 283.1823 (Jan. 2016). ISSN: 14712954. DOI: 10.1098/RSPB.2015.1708/84343.

[29] F. Delcomyn. "Insect Walking and Robotics". In: *Annual Review of Entomology* 49.Volume 49, 2004 (Jan. 2004), pp. 51–70. ISSN: 00664170. DOI: 10.1146/annurev.ento.49.061802.123257.

[30] L. Deutz. "Gait Modulation of Undulatory Microswimmers through the Lens of Optimality". PhD thesis. University of Leeds, 2024.

[31] B. Diederich, M. Schumm, and H. Cruse. "Stick Insects Walking Along Inclined Surfaces". In: *Integrative and Comparative Biology* 42.1 (Feb. 2002), pp. 165–173. ISSN: 1540-7063. DOI: 10.1093/ICB/42.1.165.

[32] D. M. Dudek and R. J. Full. "Passive mechanical properties of legs from running insects". In: *Journal of Experimental Biology* 209.8 (2006), pp. 1502–1515. ISSN: 00220949. DOI: 10.1242/JEB.02146.

[33] S. Dutta, V. Kumar, A. Shukla, N. R. Mohapatra, and U. Ganguly. "Leaky Integrate and Fire Neuron by Charge-Discharge Dynamics in Floating-Body MOSFET". In: *Scientific Reports 2017 7:1* 7.1 (Aug. 2017), pp. 8257–. ISSN: 2045-2322. DOI: 10.1038/s41598-017-07418-y.

[34] D. H. Edwards. "Neuromechanical simulation". In: *Frontiers in Behavioral Neuroscience* 4.JUL (July 2010), p. 1732. ISSN: 16625153. DOI: 10.3389/fnbeh.2010.00040.

[35] Ö. Ekeberg. "A combined neuronal and mechanical model of fish swimming". In: *Biological Cybernetics* 69.5-6 (1993), pp. 363–374. ISSN: 14320770. DOI: 10.1007/BF01185408.

[36] Ö. Ekeberg, M. Blümel, and A. Büschges. "Dynamic simulation of insect walking". In: *Arthropod Structure & Development* 33.3 (July 2004), pp. 287–300. ISSN: 1467-8039. DOI: 10.1016/J.ASD.2004.05.002.

[37] M. Endo. "Calcium release from the sarcoplasmic reticulum". In: *Physiological Reviews* 57.1 (1977), pp. 71–108. ISSN: 00319333. DOI: 10.1152/physrev.1977.57.1.71.

[38] Wallace O. Fenn. "A quantitative comparison between the energy liberated and the work performed by the isolated sartorius muscle of the frog". In: *The Journal of Physiology* 58.2-3 (Dec. 1923), pp. 175–203. ISSN: 1469-7793. DOI: 10.1113/JPHYSIOL.1923.SP002115.

[39] L. H. Field and M. M.L. Coles. "The position-dependent nature of postural resistance reflexes in the locust". In: *Journal of Experimental Biology* 188.1 (Mar. 1994), pp. 65–88. ISSN: 0022-0949. DOI: 10.1242/JEB.188.1.65.

[40] R. J. Full and A. N. Ahn. "Static Forces and Moments Generated in the Insect Leg: Comparison of a Three-Dimensional Musculo-Skeletal Computer Model With Experimental Measurements". In: *Journal of Experimental Biology* 198.6 (June 1995), pp. 1285–1298. ISSN: 0022-0949. DOI: 10.1242/JEB.198.6.1285.

[41] R. J. Full, R. Blickhan, and L. H. Ting. "Leg design in hexapedal runners." In: *The Journal of experimental biology* 158 (1991), pp. 369–390. ISSN: 00220949. DOI: 10.1242/JEB.158.1.369.

[42] R. J. Full and D. E. Koditschek. "Templates and anchors: neuromechanical hypotheses of legged locomotion on land". In: *Journal of Experimental Biology* 202.23 (Dec. 1999), pp. 3325–3332. ISSN: 0022-0949. DOI: 10.1242/JEB.202.23.3325.

[43] R. J. Full and M. S. Tu. "Mechanics of a rapid running insect: Two-, four- and six-legged locomotion". In: *Journal of Experimental Biology* 156 (1991), pp. 215–231. ISSN: 00220949. DOI: 10.1242/JEB.156.1.215.

[44] M. Garcia, A. Kuo, A. Peattie, P. Wang, and R. J. Full. "Damping And Size: Insights And Biological Inspiration". In: *International Symposium on Adaptive Motion of Animals and Machines.* (2000), pp. 1–7.

[45] C. Gebehart and A. Büschges. "The processing of proprioceptive signals in distributed networks: insights from insect motor control". In: *Journal of Experimental Biology* 227.1 (Jan. 2024). ISSN: 14779145. DOI: 10.1242/JEB.246182/340235.

[46] R. M. Ghigliazza and P. Holmes. "Towards a neuromechanical model for insect locomotion: Hybrid dynamical systems". In: *Regular and Chaotic Dynamics* 10.2 (2005), pp. 193–225. ISSN: 14684845. DOI: 10.1070/RD2005V010N02ABEH000311.

[47] C. A. Goldsmith, N. S. Szczecinski, and R. D. Quinn. "Neurodynamic modeling of the fruit fly Drosophila melanogaster". In: *Bioinspiration & Biomimetics* 15.6 (2020), p. 065003. ISSN: 1748-3190. DOI: 10.1088/1748-3190/ab9e52.

[48] S. Guo, J. Lin, T. Wöhrl, and M. Liao. "A Neuro-Musculo-Skeletal Model for Insects With Data-driven Optimization". In: *Scientific Reports 2018 8:1* 8.1 (Feb. 2018), pp. 2129–. ISSN: 2045-2322. DOI: 10.1038/s41598-018-20093-x.

[49] C. Guschlbauer, H. Scharstein, and A. Büschges. "The extensor tibiae muscle of the stick insect: biomechanical properties of an insect walking leg muscle". In: *Journal of Experimental Biology* 210.6 (Mar. 2007), pp. 1092–1108. ISSN: 0022-0949. DOI: 10.1242/JEB.02729.

[50] Christoph Guschlbauer, Scott L. Hooper, Charalampos Mantziaris, Anna Schwarz, Nicholas S. Szczecinski, and Ansgar Büschges. "Correlation between ranges of leg walking angles and passive rest angles among leg types in stick insects". In: *Current Biology* 32.10 (May 2022), pp. 2334–2340. ISSN: 18790445. DOI: 10.1016/J.CUB.2022.04.013/ASSET/58F596A4-CE4C-4054-8E4A-82FFA55FF41F/MAIN.ASSETS/GR3.JPG.

[51] N. Harischandra, A. J. Clare, J. Zakotnik, L. M.L. Blackburn, T. Matheson, and V. Dürr. "Evaluation of linear and non-linear activation dynamics models for insect muscle". In: *PLOS Computational Biology* 15.10 (2019), e1007437. ISSN: 1553-7358. DOI: 10.1371/JOURNAL.PCBI.1007437.

[52] H. Hatze. "A myocybernetic control model of skeletal muscle". In: *Biological Cybernetics* 25.2 (June 1977), pp. 103–119. ISSN: 03401200. DOI: 10.1007/BF00337268.

[53] W. J. Heitler. "The locust jump - Specialisations of the metathoracic femoral-tibial joint". In: *Journal of Comparative Physiology* 89.1 (Mar. 1974), pp. 93–104. ISSN: 03407594. DOI: 10.1007/BF00696166.

[54] S. Heitmann, N. Ferns, and M. Breakspear. "Muscle co-contraction modulates damping and joint stability in a three-link biomechanical limb". In: *Frontiers in Neurorobotics* 5.JAN (Jan. 2012), p. 12403. ISSN: 16625218. DOI: 10.3389/FNBOT.2011.00005.

[55] E. Henneman. "The size-principle: a deterministic output emerges from a set of probabilistic connections". In: *Journal of Experimental Biology* 115.1 (Mar. 1985), pp. 105–112. ISSN: 0022-0949. DOI: 10.1242/JEB.115.1.105.

[56] R. D. Herbert, B. Bolsterlee, and S. C. Gandevia. "Passive changes in muscle length". In: *Journal of Applied Physiology* 126.5 (May 2019), pp. 1445–1453. ISSN: 15221601. DOI: 10.1152/japplphysiol.00673.2018.

[57] D. Hess and A. Büschges. "Role of proprioceptive signals from an insect femur-tibia joint in patterning motoneuronal activity of an adjacent leg joint". In: *Journal of Neurophysiology* 81.4 (1999), pp. 1856–1865. ISSN: 00223077. DOI: 10.1152/JN.1999.81.4.1856.

[58] A. V. Hill. "Length of muscle, and the heat and tension developed in an isometric contraction". In: *The Journal of Physiology* 60.4 (Sept. 1925), pp. 237–263. ISSN: 1469-7793. DOI: 10.1113/JPHYSIOL.1925.SP002242.

[59] A. V. Hill. "The heat of shortening and the dynamic constants of muscle". In: *Proceedings of the Royal Society of London. Series B - Biological Sciences* 126.843 (1938), pp. 136–195. ISSN: 2053-9193. DOI: 10.1098/rspb.1938.0050.

[60] A. L. Hodgkin and A. F. Huxley. "Currents carried by sodium and potassium ions through the membrane of the giant axon of Loligo". In: *The Journal of Physiology* 116.4 (Apr. 1952), pp. 449–472. ISSN: 1469-7793. DOI: 10.1113/JPHYSIOL.1952.SP004717.

[61] N. C. Holt, J. M. Wakeling, and A. A. Biewener. "The effect of fast and slow motor unit activation on whole-muscle mechanical performance: the size principle may not pose a mechanical paradox". In: *Proceedings. Biological sciences* 281.1783 (Apr. 2014). ISSN: 1471-2954. DOI: 10.1098/RSPB.2014.0002.

[62] N. C. Holt and C. D. Williams. "Can Strain Dependent Inhibition of Cross-Bridge Binding Explain Shifts in Optimum Muscle Length?" In: *Integrative and Comparative Biology* 58.2 (Aug. 2018), pp. 174–185. ISSN: 1540-7063. DOI: 10.1093/ICB/ICY050.

[63] S. L. Hooper, C. Guschlbauer, M. Blümel, P. Rosenbaum, M. Gruhn, T. Akay, and A. Büschges. "Neural Control of Unloaded Leg Posture and of Leg Swing in Stick Insect, Cockroach, and Mouse Differs from That in Larger Animals". In: *Journal of Neuroscience* 29.13 (2009), pp. 4109–4119. ISSN: 0270-6474. DOI: 10.1523/JNEUROSCI.5510-08.2009.

[64] Scott L. Hooper, Christoph Guschlbauer, Frederique Wieters, Markus Aswendt, and Ansgar Büschges. "Passive responses in mouse hind leg locomotion". In: *Current Biology* 35.7 (Apr. 2025), pp. 1459–1469. ISSN: 18790445. DOI: 10.1016/j.cub.2024.12.048.

[65] A. J. Ijspeert and M. A. Daley. "Integration of feedforward and feedback control in the neuromechanics of vertebrate locomotion: a review of experimental, simulation and robotic studies". In: *Journal of Experimental Biology* 226.15 (Aug. 2023). ISSN: 14779145. DOI: 10.1242/JEB.245784/325856.

[66] D. L. Jindrich and R. J. Full. "Dynamic stabilization of rapid hexapedal locomotion". In: *Journal of Experimental Biology* 205.18 (Sept. 2002), pp. 2803–2823. ISSN: 00220949. DOI: 10.1242/JEB.205.18.2803.

[67] R. K. Josephson. "Contraction dynamics and power output of skeletal muscle". In: *Annual Review of Physiology* 55.Volume 55, 1993 (Mar. 1993), pp. 527–546. ISSN: 00664278. DOI: 10.1146/annurev.ph.55.030193.002523.

[68] Bernhard Katz. "The relation between force and speed in muscular contraction". In: *The Journal of Physiology* 96.1 (June 1939), pp. 45–64. ISSN: 1469-7793. DOI: 10.1113/JPHYSIOL.1939.SP003756.

[69] D. Klocke and H. Schmitz. "The importance of water for the mechanical properties of insect cuticle". In: *https://doi.org/10.1117/12.879889* 7975 (Mar. 2011), pp. 84–90. ISSN: 0277786X. DOI: 10.1117/12.879889.

[70] S. Knops, T. I. Tóth, C. Guschlbauer, M. Gruhn, and S. Daun-Gruhn. "A neuromechanical model for the neuronal basis of curve walking in the stick insect". In: *Journal of Neurophysiology* 109.3 (2013), pp. 679–691. ISSN: 15221598. DOI: 10.1152/JN.00648.2012.

[71] D. E. Koditschek, R. J. Full, and M. Buehler. "Mechanical aspects of legged locomotion control". In: *Arthropod Structure and Development* 33.3 (2004), pp. 251–272. ISSN: 14678039. DOI: 10.1016/J.ASD.2004.06.003.

[72] J. J. Kozacik. "Stepping Patterns in the Cockroach, Periplaneta Americana". In: *Journal of Experimental Biology* 90.1 (Feb. 1981), pp. 357–360. ISSN: 0022-0949. DOI: 10.1242/JEB.90.1.357.

[73] J. Kukalová-Peck. "Origin of the insect wing and wing articulation from the arthropodan leg". In: *Canadian Journal of Zoology* 61.7 (July 1983), pp. 1618–1669. ISSN: 0008-4301. DOI: 10.1139/Z83-217.

[74] R. Kukillaya, J. Proctor, and P. Holmes. "Neuromechanical models for insect locomotion: Stability, maneuverability, and proprioceptive feedback". In: *Chaos* 19.2 (June 2009). ISSN: 10541500. DOI: 10.1063/1.3141306/909524.

[75] G. Laurent and D. Richard. "The Organization and Role During Locomotion of the Proximal Musculature of the Cricket Foreleg I. Anatomy and Innervation". In: *Journal of Experimental Biology* 123.1 (July 1986), pp. 255–283. ISSN: 0022-0949. DOI: 10.1242/JEB.123.1.255.

[76] B. Leung, N. Bijma, E. Baird, M. Dacke, S. Gorb, and P. Manoonpong. "Rules for the Leg Coordination of Dung Beetle Ball Rolling Behaviour". In: *Scientific Reports 2020 10:1* 10.1 (June 2020), pp. 9278–. ISSN: 2045-2322. DOI: 10.1038/s41598-020-66248-7.

[77] B. Leung, M. Thor, and P. Manoonpong. "Modular neural control for bio-inspired walking and ball rolling of a dung beetle-like robot". In: *ALIFE 2018 - 2018 Conference on Artificial Life: Beyond AI* (July 2020), pp. 335–342. DOI: 10.1162/ISAL{_}A{_}00064/99662.

[78] V. Lobato-Rios, S. T. Ramalingasetty, P. G. Özdil, J. Arreguit, A. J. Ijspeert, and P. Ramdya. "NeuroMechFly, a neuromechanical model of adult Drosophila melanogaster". In: *Nature Methods 2022 19:5* 19.5 (May 2022), pp. 620–627. ISSN: 1548-7105. DOI: 10.1038/s41592-022-01466-7.

[79] V. Loreau, W. Koolhaas, E. HY. Chan, P. D. Boissier, N. Brouilly, S. Avosani, A. Sane, C. Pitaval, S. Reiter, N. M. Luis, P. Mangeol, A. C. von Philipsborn, J.-F. Rupprecht, D. Görlich, B. H. Habermann, and F. Schnorrer. "Titin-dependent biomechanical feedback tailors sarcomeres to specialised muscle functions in insects". In: *bioRxiv* (Oct. 2024), p. 2024.09.30.615857. DOI: 10.1101/2024.09.30.615857.

[80] S. Lu and F. Xu. "Linear leaky-integrate-and-fire neuron model based spiking neural networks and its mapping relationship to deep neural networks". In: *Frontiers in Neuroscience* 16 (Aug. 2022), p. 857513. ISSN: 1662453X. DOI: 10.3389/FNINS.2022.857513.

[81] E. G. Matthews. "Observations on the Ball-Rolling Behavior of Canthon Pilularius (L.) (Coleoptera, Scarabaeidae)". In: *Psyche: A Journal of Entomology* 70.2 (Jan. 1963), pp. 75–93. ISSN: 1687-7438. DOI: 10.1155/1963/23630.

[82] J. M. Melis, I. Siwanowicz, and M. H. Dickinson. "Machine learning reveals the control mechanics of an insect wing hinge". In: *Nature 2024 628:8009* 628.8009 (Apr. 2024), pp. 795–803. ISSN: 1476-4687. DOI: 10.1038/s41586-024-07293-4.

[83] *MuJoCo — Advanced Physics Simulation*. URL: https://mujoco.org/.

[84] *MuJoCo Documentation*. URL: https://mujoco.readthedocs.io/en/stable/overview.html.

[85] M. Naris, N. S. Szczecinski, and R. D. Quinn. "A neuromechanical model exploring the role of the common inhibitor motor neuron in insect locomotion". In: *Biological*

Cybernetics 114.1 (Feb. 2020), pp. 23–41. ISSN: 14320770. DOI: 10.1007/s00422-019-00811-y.

[86] *Nevergrad - A gradient-free optimization platform*. URL: https://facebookresearch.github.io/nevergrad/.

[87] P. L. Newland and Y. Kondom. "Dynamics of neurons controlling movements of a locust hind leg: II. Flexor tibiae motor neurons". In: *Journal of Neurophysiology* 77.4 (1997), pp. 1731–1746. ISSN: 00223077. DOI: 10.1152/JN.1997.77.4.1731.

[88] S. Ostojic and N. Brunel. "From Spiking Neuron Models to Linear-Nonlinear Models". In: *PLOS Computational Biology* 7.1 (2011), e1001056. ISSN: 1553-7358. DOI: 10.1371/JOURNAL.PCBI.1001056.

[89] P. Gi. Özdil, C. Ning, J. S. Phelps, S. Wang-Chen, G. Elisha, A. Blanke, A. J. Ijspeert, and P. Ramdya. "Musculoskeletal simulation of limb movement biomechanics in Drosophila melanogaster". In: (Sept. 2025).

[90] S. N. Patek, D. M. Dudek, and M. V. Rosario. "From bouncy legs to poisoned arrows: Elastic movements in invertebrates". In: *Journal of Experimental Biology* 214.12 (2011), pp. 1973–1980. ISSN: 00220949. DOI: 10.1242/JEB.038596.

[91] J. W. S. Pringle. "Proprioception In InsectsI. A New Type Of Mechanical Receptor From The Palps Of The Cockroach". In: *Journal of Experimental Biology* 15.1 (Jan. 1938), pp. 101–113. ISSN: 0022-0949. DOI: 10.1242/JEB.15.1.101.

[92] J. W. S. Pringle. "The Motor Mechanism of the Insect Leg". In: *Journal of Experimental Biology* 16.2 (Apr. 1939), pp. 220–231. ISSN: 0022-0949. DOI: 10.1242/JEB.16.2.220.

[93] R. Raikova, J. Celichowski, M. Pogrzebna, H. Aladjov, and P. Krutki. "Modeling of summation of individual twitches into unfused tetanus for various types of rat motor units". In: *Journal of Electromyography and Kinesiology* 17.2 (Apr. 2007), pp. 121–130. ISSN: 1050-6411. DOI: 10.1016/J.JELEKIN.2006.01.005.

[94] R. Raikova, M. Pogrzebna, H. Drzymała, J. Celichowski, and H. Aladjov. "Variability of successive contractions subtracted from unfused tetanus of fast and slow motor units". In: *Journal of Electromyography and Kinesiology* 18.5 (Oct. 2008), pp. 741–751. ISSN: 1050-6411. DOI: 10.1016/J.JELEKIN.2007.02.010.

[95] P. Ramdya, R. Thandiackal, R. Cherney, T. Asselborn, R. Benton, A. J. Ijspeert, and D. Floreano. "Climbing favours the tripod gait over alternative faster insect gaits".

In: *Nature Communications 2017 8:1* 8.1 (Feb. 2017), pp. 14494–. ISSN: 2041-1723. DOI: 10.1038/ncomms14494.

[96] D. E. Rassier, B. R. MacIntosh, and W. Herzog. "Length dependence of active force production in skeletal muscle". In: *Journal of Applied Physiology* 86.5 (1999), pp. 1445–1457. ISSN: 87507587. DOI: 10.1152/JAPPL.1999.86.5.1445.

[97] R. Riener and T. Edrich. "Identification of passive elastic joint moments in the lower extremities". In: *Journal of Biomechanics* 32.5 (1999), pp. 539–544. ISSN: 0021-9290. DOI: 10.1016/S0021-9290(99)00009-3.

[98] S. Rubeo, N. S. Szczecinski, and R. D. Quinn. "A Synthetic Nervous System Controls a Simulated Cockroach". In: *Applied Sciences 2018, Vol. 8,* 8.1 (Dec. 2017). ISSN: 2076-3417. DOI: 10.3390/APP8010006.

[99] S. Ryckebusch and G. Laurent. "Rhythmic patterns evoked in locust leg motor neurons by the muscarinic agonist pilocarpine". In: *Journal of Neurophysiology* 69.5 (1993), pp. 1583–1595. ISSN: 00223077. DOI: 10.1152/JN.1993.69.5.1583.

[100] M. Schilling, T. Hoinville, J. Schmitz, and H. Cruse. "Walknet, a bio-inspired controller for hexapod walking". In: *Biological Cybernetics 2013 107:4* 107.4 (July 2013), pp. 397–419. ISSN: 1432-0770. DOI: 10.1007/S00422-013-0563-5.

[101] M. Schilling, J. Paskarbeit, T. Hoinville, A. Hüffmeier, A. Schneider, J. Schmitz, and H. Cruse. "A hexapod walker using a heterarchical architecture for action selection". In: *Frontiers in Computational Neuroscience* 7.SEP (Sept. 2013), p. 42494. ISSN: 16625188. DOI: 10.3389/FNCOM.2013.00126.

[102] J. Smolka, M. J. Byrne, C. H. Scholtz, and M. Dacke. "A new galloping gait in an insect". In: *Current Biology* 23.20 (Oct. 2013), R913–R915. ISSN: 0960-9822. DOI: 10.1016/J.CUB.2013.09.031.

[103] Rainer Storn and Kenneth Price. "Differential Evolution - A Simple and Efficient Heuristic for Global Optimization over Continuous Spaces". In: *Journal of Global Optimization* 11.4 (1997), pp. 341–359. ISSN: 09255001. DOI: 10.1023/A:1008202821328/METRICS.

[104] G. P. Sutton. "Biomechanics: Passive forces set the stage for stick insects". In: *Current Biology* 32.10 (May 2022), R472–R474. ISSN: 0960-9822. DOI: 10.1016/J.CUB.2022.03.042.

[105] G. P. Sutton, N. S. Szczecinski, R. D. Quinn, and H. J. Chiel. "Phase shift between joint rotation and actuation reflects dominant forces and predicts muscle activation

patterns". In: *PNAS Nexus* 2.10 (2023). ISSN: 27526542. DOI: 10.1093/pnasnexus/pgad298.

[106] N. S. Szczecinski, J. P. Martin, D. J. Bertsch, R. E. Ritzmann, and R. D. Quinn. "Neuromechanical model of praying mantis explores the role of descending commands in pre-strike pivots". In: *Bioinspiration and Biomimetics* 10.6 (Nov. 2015). ISSN: 17483190. DOI: 10.1088/1748-3190/10/6/065005.

[107] R. Tajiri, K. Misaki, S. Yonemura, and S. Hayashi. "Joint morphology in the insect leg: evolutionary history inferred from Notch loss-of-function phenotypes in Drosophila". In: *Development* 138.21 (Nov. 2011), pp. 4621–4626. ISSN: 0950-1991. DOI: 10.1242/DEV.067330.

[108] M. Thor, T. Strøm-Hansen, L. B. Larsen, A. Kovalev, S. N. Gorb, E. Baird, and P. Manoonpong. "A dung beetle-inspired robotic model and its distributed sensor-driven control for walking and ball rolling". In: *Artificial Life and Robotics* 23.4 (Dec. 2018), pp. 435–443. ISSN: 16147456. DOI: 10.1007/S10015-018-0456-8.

[109] T. I. Toth, J. Schmidt, A. Büschges, and S. Daun-Gruhn. "A Neuro-Mechanical Model of a Single Leg Joint Highlighting the Basic Physiological Role of Fast and Slow Muscle Fibres of an Insect Muscle System". In: *PLOS ONE* 8.11 (Nov. 2013), e78247. ISSN: 1932-6203. DOI: 10.1371/JOURNAL.PONE.0078247.

[110] T. I. Tóth, E. Berg, and S. Daun. "Modeling search movements of an insect's front leg". In: *Physiological Reports* 5.22 (Nov. 2017), e13489. ISSN: 2051-817X. DOI: 10.14814/PHY2.13489.

[111] T. I. Tóth, S. Knops, and S. Daun-Gruhn. "A neuromechanical model explaining forward and backward stepping in the stick insect". In: *Journal of Neurophysiology* 107.12 (June 2012), pp. 3267–3280. ISSN: 00223077. DOI: 10.1152/JN.01124.2011.

[112] A. von Twickel, C. Guschlbauer, S. L. Hooper, and A. Büschges. "Swing Velocity Profiles of Small Limbs Can Arise from Transient Passive Torques of the Antagonist Muscle Alone". In: *Current Biology* 29.1 (Jan. 2019), pp. 1–12. ISSN: 09609822. DOI: 10.1016/J.CUB.2018.11.016.

[113] T. K. Uchida and S. L. Delp. *Biomechanics of Movement: The Science of Sports, Robotics, and Rehabilitation.* 2021. ISBN: 9780262359191.

[114] Y. Ueyama and E. Miyashita. "Cocontraction of Pairs of Muscles around Joints May Improve an Accuracy of a Reaching Movement: a Numerical Simulation Study". In:

AIP Conference Proceedings 1371.1 (June 2011), pp. 73–82. ISSN: 0094-243X. DOI: 10.1063/1.3596629.

[115] F. J. Valero-Cuevas, H. Hoffmann, M. U. Kurse, J. J. Kutch, and E. A. Theodorou. "Computational Models for Neuromuscular Function". In: *IEEE Reviews in Biomedical Engineering* 2 (2009), pp. 110–135. ISSN: 19411189. DOI: 10.1109/RBME.2009.2034981.

[116] R. Vaxenburg, I. Siwanowicz, J. Merel, A. A. Robie, C. Morrow, G. Novati, Z. Stefanidi, G. J. Both, G. M. Card, M. B. Reiser, M. M. Botvinick, K. M. Branson, Y. Tassa, and S. C. Turaga. "Whole-body physics simulation of fruit fly locomotion". In: *Nature 2025 643:8074* 643.8074 (Apr. 2025), pp. 1312–1320. ISSN: 1476-4687. DOI: 10.1038/s41586-025-09029-4.

[117] T. Wadden and Ö. Ekeberg. "A neuro-mechanical model of legged locomotion: Single leg control". In: *Biological Cybernetics* 79.2 (1998), pp. 161–173. ISSN: 03401200. DOI: 10.1007/S004220050468.

[118] C. Wan and S. Gorb. "Functional morphology and biomechanics of arthropods". In: *Journal of Comparative Physiology A: Neuroethology, Sensory, Neural, and Behavioral Physiology* 209.2 (Mar. 2023), pp. 215–218. ISSN: 14321351. DOI: 10.1007/S00359-023-01621-1.

[119] R. Wang. "Basic Models and Applications of Resistor-Capacitor Circuits and Simulations Using Falstad". In: *Proceedings - 2021 4th World Conference on Mechanical Engineering and Intelligent Manufacturing, WCMEIM 2021* (2021), pp. 360–365. DOI: 10.1109/WCMEIM54377.2021.00080.

[120] R. Wang, S. Yan, M. Schlippe, O. Tarassova, G. V. Pennati, F. Lindberg, C. Körting, A. Destro, L. Yang, B. Shi, and A. Arndt. "Passive Mechanical Properties of Human Medial Gastrocnemius and Soleus Musculotendinous Unit". In: *BioMed Research International* 2021 (2021), p. 8899699. ISSN: 2314-6141. DOI: 10.1155/2021/8899699.

[121] *WebPlotDigitizer*. URL: https://web.eecs.utk.edu/~dcostine/personal/PowerDeviceLib/DigiTest/index.html.

[122] T. Weihmann. "Survey of biomechanical aspects of arthropod terrestrialisation – Substrate bound legged locomotion". In: *Arthropod Structure & Development* 59 (Nov. 2020), p. 100983. ISSN: 1467-8039. DOI: 10.1016/J.ASD.2020.100983.

[123] D. M. Wilson. "Insect walking." In: *Annual review of entomology* 11.Volume 11, 1966 (Jan. 1966), pp. 103–122. ISSN: 00664170. DOI: 10.1146/ANNUREV.EN.11.010166.000535.

[124] E. Wilson, E. Rustighi, B. R. MacE, and P. L. Newland. "Isometric force generated by locust skeletal muscle: Responses to single stimuli". In: *Biological Cybernetics* 102.6 (June 2010), pp. 503–511. ISSN: 03401200. DOI: 10.1007/S00422-010-0382-X.

[125] H. Wolf. "Inhibitory motoneurons in arthropod motor control: Organisation, function, evolution". In: *Journal of Comparative Physiology A: Neuroethology, Sensory, Neural, and Behavioral Physiology* 200.8 (June 2014), pp. 693–710. ISSN: 14321351. DOI: 10.1007/S00359-014-0922-2.

[126] F. E. Zajac. "Muscle and tendon: properties, models, scaling, and application to biomechanics and motor control." In: *Critical Reviews in Biomedical Engineering* 17.4 (1989), pp. 359–411. ISSN: 0278-940X.

[127] J. Zakotnik, T. Matheson, and V. Dürr. "Co-Contraction and Passive Forces Facilitate Load Compensation of Aimed Limb Movements". In: *Journal of Neuroscience* 26.19 (May 2006), pp. 4995–5007. ISSN: 0270-6474. DOI: 10.1523/JNEUROSCI.0161-06.2006.

Appendix A

Supplementary Information

A.1 Derivation of Nondimensional Equations of Motion

A.1.1 Muscle-Tendon Unit Model

In Section 4.2, the force generated by muscle-tendon unit (MTU) was defined as

$$F_i = f_a^{(i)} + f_p^{(i)}\,, \tag{A.1}$$

where $f_a^{(i)}$ and $f_p^{(i)}$ denote the the active and passive force components, respectively.

On the one hand, the active force is modelled as

$$f_a^{(i)} = \kappa_a^{(i)}(L_t^{(i)} - L_m^{(i)}) - \beta_a^{(i)}\dot{L}_m^{(i)}\,, \tag{A.2}$$

with the coefficients $\kappa_a^{(i)}$, $L_t^{(i)}$, and $\beta_a^{(i)}$ defined as

$$\begin{aligned} \kappa_a^{(i)} &= \kappa_{\max}^{(i)}\sigma(A_m^{(i)})\,, \\ L_t^{(i)} &= L_0^{(i)} - \sigma(A_m^{(i)})(L_0^{(i)} - L_{\min}^{(i)})\,, \\ \beta_a^{(i)} &= \beta_{\max}^{(i)}\sigma(A_m^{(i)})\,. \end{aligned}$$

On the other hand, the passive force is expressed as

$$f_p^{(i)} = \kappa_p^{(i)}(L_0^{(i)} - L_m^{(i)}) - \beta_p^{(i)}\dot{L}_m^{(i)}\,. \tag{A.3}$$

To nondimensionalise these equations, we define the characteristic length and time scales

as the muscle resting length L_0 and the joint cycle period τ, respectively. This leads to the following dimensionless length $\hat{L}_m$ and time $\hat{t}$ variables:

$$\hat{L}_m = \frac{L_m}{L_0}\,, \quad \hat{t} = \frac{t}{\tau}\,.$$

For the sake of simplicity, we omit the index (i) in the following derivations. Substituting the dimensionless variables into equation A.2 yields

$$f_a = \kappa_a(L_t - \hat{L}_m L_0) - \frac{\beta_a}{\tau}\frac{d(\hat{L}_m L_0)}{d\hat{t}}\,.$$

Multiplying by the term $1/L_0$ results in

$$\frac{f_a}{L_0} = \kappa_a(\hat{L}_t - \hat{L}_m) - \frac{\beta_a}{\tau}\frac{d\hat{L}_m}{d\hat{t}}\,,$$

where the dimensionless activation-dependant tension length $\hat{L}_t$ is defined as

$$\hat{L}_t = \frac{L_t}{L_0} = 1 - \sigma(A_m)\left(1 - \frac{L_{\min}}{L_0}\right)\,.$$

Substituting the terms κ_a and β_a gives

$$\frac{f_a}{L_0} = \sigma(A_m)\left[\kappa_{\max}(\hat{L}_t - \hat{L}_m) - \frac{\beta_{\max}}{\tau}\frac{d\hat{L}_m}{d\hat{t}}\right]\,,$$

To simplify further, we follow the common steps of nondimensionalisation [23], and divide the equation by the coefficient of the highest-order derivative term $\beta_{\max}/\tau$, resulting in

$$\frac{\tau f_a}{L_0\beta_{\max}} = \sigma(A_m)\left[\left\{\frac{\kappa_{\max}}{\beta_{\max}}\tau\right\}(\hat{L}_t - \hat{L}_m) - \frac{d\,\hat{L}_m}{d\hat{t}}\right]\,.$$

We now define the dimensionless stiffness-to-damping ratio η_a and the nondimensional MTU active force $\hat{f}_a$ as

$$\eta_a = \frac{\kappa_{\max}}{\beta_{\max}}\tau\,, \quad \hat{f}_a = \frac{\tau}{L_0\beta_{\max}}f_a\,.$$

Thus, the nondimensional form of the active force becomes

$$\hat{f}_a = \sigma(A_m)\left[\eta_a(\hat{L}_t - \hat{L}_m) - \dot{\hat{L}}_m\right]\,. \tag{A.4}$$

Similarly, substituting the variables $\hat{L}_m$ and $\hat{t}$ into equation A.3 results in

$$f_p = \kappa_p(L_0 - \hat{L}_m L_0) - \frac{\beta_p}{\tau}\frac{d(\hat{L}_m L_0)}{d\hat{t}}\,,$$

and following the same previous steps of nondimensionalisation, we obtain

$$\frac{\tau f_p}{L_0\beta_p} = \left\{\frac{\kappa_p}{\beta_p}\,\tau\right\}(1 - \hat{L}_m) - \frac{d\,\hat{L}_m}{d\hat{t}}\,.$$

Where we define the the corresponding dimensionless parameter η_p and the dimensionless MTU passive force $\hat{f}_p$ as follows

$$\eta_p = \frac{\kappa_p}{\beta_p}\,\tau\,, \quad \hat{f}_p = \frac{\tau}{L_0\beta_p} f_p\,.$$

The nondimensional passive force is then

$$\hat{f}_p = \eta_p(1 - \hat{L}_m) - \hat{\dot{L}}_m\,. \tag{A.5}$$

Combining the nondimensional active (equation A.4) and passive (equation A.5) forces into the total MTU force (equation A.1) gives

$$F = \frac{L_0\beta_{\max}}{\tau}\hat{f}_a + \frac{L_0\beta_p}{\tau}\hat{f}_p\,.$$

Multiplying by τ/L_0 yields

$$\frac{\tau F}{L_0} = \beta_{\max}\hat{f}_a + \beta_p\hat{f}_p\,.$$

We then divide by the passive damping β_p

$$\frac{\tau F}{L_0\beta_p} = \left\{\frac{\beta_{\max}}{\beta_p}\right\}\hat{f}_a + \hat{f}_p\,,$$

where we define the dimensionless parameter μ_j and the dimensionless total MTU force

$$\mu_j = \frac{\beta_{\max}}{\beta_p}\,, \quad \hat{F} = \frac{\tau}{L_0\beta_p}F\,.$$

Thus, the final nondimensional form of the total MTU force is

$$\hat{F} = \mu_j\hat{f}_a + \hat{f}_p\,. \tag{A.6}$$

This formulation eliminates all dimensional parameters, resulting in a fully nondimensional representation of the MTU model. To summarise, the final expressions are as follows:

- Active force:
$$\hat{f}_a^{(i)} = \sigma(A_m^{(i)}) \left[\eta_a^{(i)} (\hat{L}_t^{(i)} - \hat{L}_m^{(i)}) - \hat{\dot{L}}_m^{(i)} \right] .$$
- Passive force:
$$\hat{f}_p^{(i)} = \eta_p^{(i)} (1 - \hat{L}_m^{(i)}) - \hat{\dot{L}}_m^{(i)} .$$
- Total force:
$$\hat{F}_i = \mu_j^{(i)} \hat{f}_a^{(i)} + \hat{f}_p^{(i)} .$$

A.1.2 Single-MTU Joint Model

Section 4.3 establishes the joint equation of motion as

$$T_{\text{net}} = F_{\text{ext}} \, r_{\text{ext}} - \frac{mgl \sin\theta}{2} , \tag{A.7}$$

where r_{ext} is the moment arm of the extensor MTU, given by

$$r_{\text{ext}} = \frac{d \, L_m^{\text{ext}}}{d\theta} .$$

To express the moment arm in dimensionless form, we define the state variable of the system $\hat{\theta}$ as

$$\hat{\theta} = \theta, \quad d\hat{\theta} = d\theta ,$$

and thus, its second derivative is

$$\ddot{\theta} = \frac{\ddot{\hat{\theta}}}{\tau^2} .$$

Substituting the dimensionless variables $\hat{L}_m$ and $\hat{\theta}$ into the moment arm expression yields

$$r_{\text{ext}} = \frac{d \, \hat{L}_m^{\text{ext}} L_0^{\text{ext}}}{d\hat{\theta}} = L_0^{\text{ext}} \hat{r}_{\text{ext}} ,$$

where $\hat{r}_{\text{ext}}$ is the nondimensional moment arm of the extensor MTU.

Next, we substitute the force F_{ext} and moment arm r_{ext} terms in equation A.7 with their dimensionless counterparts $\hat{F}_{\text{ext}}$ and $\hat{r}_{\text{ext}}$, resulting in

$$T_{\text{net}} = \left(\frac{L_0^{\text{ext}} \beta_{\max}^{\text{ext}}}{\tau} \hat{F}_{\text{ext}} \right) L_0^{\text{ext}} \hat{r}_{\text{ext}} - \frac{mgl \sin\hat{\theta}}{2} .$$

Multiplying both sides by $\tau/(L_0^{\text{ext}})^2\beta_{\max}^{\text{ext}}$ gives

$$\frac{\tau}{(L_0^{\text{ext}})^2\beta_{\max}^{\text{ext}}}T_{\text{net}} = \hat{F}_{\text{ext}}\,\hat{r}_{\text{ext}} - \left(\frac{\tau}{(L_0^{\text{ext}})^2\beta_{\max}^{\text{ext}}}\right)\frac{mgl\sin\hat{\theta}}{2}\,,$$

from which we define the dimensionless parameter γ and the dimensionless net torque

$$\gamma = \frac{mgl}{2(L_0^{\text{ext}})^2\beta_{\max}^{\text{ext}}}\tau\,, \quad \hat{T}_{\text{net}} = \frac{\tau}{(L_0^{\text{ext}})^2\beta_{\max}^{\text{ext}}}T_{\text{net}}\,.$$

Thus, the nondimensional net torque equation becomes

$$\hat{T}_{\text{net}} = \hat{F}_{\text{ext}}\,\hat{r}_{\text{ext}} - \gamma\,(\sin\theta)\,. \tag{A.8}$$

Note that the joint angle θ is inherently dimensionless (measured in radians), so we omit the hat notation $(\hat{\cdot})$ for simplicity.

To derive the rotational equation of motion, we include the moment of inertia J of the distal link. Starting from the dimensional form

$$J\ddot{\theta} = T_{\text{net}}\,,$$

and substituting the dimensionless variable and the term T_{net}, we obtain

$$\frac{J\ddot{\theta}}{\tau^2} = \frac{(L_0^{\text{ext}})^2\beta_{\text{ext}}}{\tau}\hat{T}_{\text{net}}\,.$$

Rewriting this yields

$$\frac{J}{(L_0^{\text{ext}})^2\beta_{\text{ext}}\,\tau}\,\ddot{\theta} = \hat{F}_{\text{ext}}\,\hat{r}_{\text{ext}} - \gamma\,(\sin\theta)\,,$$

where we define the dimensionless moment of inertia $\hat{J}$ as

$$\hat{J} = \frac{J}{(L_0^{\text{ext}})^2\beta_{\text{ext}}\,\tau}\,.$$

Finally, the nondimensional rotational equation of motion for the joint becomes

$$\ddot{\theta} = \frac{1}{\hat{J}}\left[\hat{F}_{\text{ext}}\,\hat{r}_{\text{ext}} - \gamma\,(\sin\theta)\right]\,. \tag{A.9}$$

A.1.3 Antagonistic-MTU Joint Model

In Section 4.4, we introduced the antagonistic-MTU joint model, where the system is actuated by a pair of antagonistic muscles and the passive joint properties are represented by a rotational spring and damper. The equation of motion for this model is

$$T_{\text{net}} = \sum_{i=\{\text{fl, ext}\}} F_i\, r_i - \kappa_j\, \Delta\theta - \beta_j\, \dot{\theta} - \frac{mgl \sin\theta}{2}\,. \tag{A.10}$$

Here, the total MTU force is described by equation A.2:

$$F_i = \kappa_a^{(i)}(L_t^{(i)} - L_m^{(i)}) - \beta_a^{(i)} \dot{L}_m^{(i)}\,.$$

Substituting the dimensionless variables $\hat{L}_m$ and τ into this expression yields

$$\frac{\tau F_i}{L_0^{(i)} \beta_{\max}^{(i)}} = \sigma(A_m) \left[\left\{ \frac{\kappa_{\max}^{(i)}}{\beta_{\max}^{(i)}} \tau \right\} (\hat{L}_t^{(i)} - \hat{L}_m^{(i)}) - \frac{d\,\hat{L}_m^{(i)}}{d\hat{t}} \right],$$

from which we define the dimensionless parameter $\eta_a^{(i)}$ and the dimensionless form of the total MTU force as

$$\eta_a^{(i)} = \frac{\kappa_a^{(i)}}{\beta_a^{(i)}} \tau\,, \quad \hat{F}_i = \frac{\tau}{L_0^{(i)} \beta_{\max}^{(i)}} F_i\,.$$

Therefore, the nondimensional MTU total force becomes

$$\hat{F}_i = \sigma(A_m) \left[\eta_a^{(i)} (\hat{L}_t^{(i)} - \hat{L}_m^{(i)}) - \hat{\dot{L}}_m^{(i)} \right]. \tag{A.11}$$

Note that equation A.10 can be reformulated to express the net joint torque as the sum of its individual contributions: the torque generated by the muscle–tendon units T_{MTU}, the torque arising from passive joint properties T_{pass}, and the gravitational torque acting on the distal segment T_{grav}:

$$T_{\text{net}} = T_{\text{MTU}} + T_{\text{pass}} + T_{\text{grav}} \tag{A.12}$$

where

$$T_{\text{MTU}} = \sum_{i=\{\text{fl, ext}\}} F_i\, r_i\,,$$

$$T_{\text{pass}} = -(\,\kappa_j\, \Delta\theta + \beta_j\, \dot{\theta}\,)\,,$$

and

$$T_{\text{grav}} = \frac{mgl \sin\theta}{2}\,.$$

This allow us to nondimensionalise each individual torque contribution. By substituting each total force term F_i into T_{MTU} gives

$$T_{\mathrm{MTU}} = \left(\frac{L_0^{\mathrm{fl}}\,\beta_{\max}^{\mathrm{fl}}}{\tau}\right)\hat{F}_{\mathrm{fl}}\,r_{\mathrm{fl}} + \left(\frac{L_0^{\mathrm{ext}}\,\beta_{\max}^{\mathrm{ext}}}{\tau}\right)\hat{F}_{\mathrm{ext}}\,r_{\mathrm{ext}}\,.$$

Replacing r_i with its dimensionless form $\hat{r}_i = r_i/L_0^{(i)}$, we get

$$T_{\mathrm{MTU}} = \left(\frac{L_0^{\mathrm{fl}}\,\beta_{\max}^{\mathrm{fl}}}{\tau}\right)\hat{F}_{\mathrm{fl}}\,(L_0^{\mathrm{fl}}\,\hat{r}_{\mathrm{fl}}) + \left(\frac{L_0^{\mathrm{ext}}\,\beta_{\max}^{\mathrm{ext}}}{\tau}\right)\hat{F}_{\mathrm{ext}}\,(L_0^{\mathrm{ext}}\,\hat{r}_{\mathrm{ext}})\,.$$

Multiplying by $\tau/(L_0^{\mathrm{fl}})^2\,\beta_{\max}^{\mathrm{fl}}$ gives

$$\frac{\tau}{(L_0^{\mathrm{fl}})^2\,\beta_{\max}^{\mathrm{fl}}}\,T_{\mathrm{MTU}} = \hat{F}_{\mathrm{fl}}\,\hat{r}_{\mathrm{fl}} + \left\{\frac{(L_0^{\mathrm{ext}})^2\,\beta_{\max}^{\mathrm{ext}}}{(L_0^{\mathrm{fl}})^2\,\beta_{\max}^{\mathrm{fl}}}\right\}\hat{F}_{\mathrm{ext}}\,\hat{r}_{\mathrm{ext}}\,,$$

where we define the dimensionless asymmetry parameter μ_m and the dimensionless MTU torque as

$$\mu_m = \frac{(L_0^{\mathrm{ext}})^2\,\beta_{\max}^{\mathrm{ext}}}{(L_0^{\mathrm{fl}})^2\,\beta_{\max}^{\mathrm{fl}}}\,, \quad \hat{T}_{\mathrm{MTU}} = \frac{\tau}{(L_0^{\mathrm{fl}})^2\,\beta_{\max}^{\mathrm{fl}}}\,T_{\mathrm{MTU}}\,.$$

Next, we proceed with the nondimensionalisation of the passive torque contribution

$$T_{\mathrm{pass}} = -(\,\kappa_j\,\Delta\theta + \beta_j\,\dot{\theta}\,)\,,$$

where $\Delta\theta = \theta - \theta_{\mathrm{rest}}$. Substituting dimensionless variables and dividing by β_j/τ yields

$$\frac{\tau}{\beta_j}\,T_{\mathrm{pass}} = -\left\{\frac{\kappa_j}{\beta_j}\,\tau\right\}\Delta\theta - \dot{\theta}\,,$$

with the defined dimensionless parameter η_j and passive joint torque given by

$$\eta_j = \frac{\kappa_j}{\beta_j}\,\tau\,, \quad \hat{T}_{\mathrm{pass}} = \frac{\tau}{\beta_j}\,T_{\mathrm{pass}}\,.$$

Substituting T_{MTU} and T_{pass} by their dimensionless expressions into equation A.12 yields

$$T_{\mathrm{net}} = \left(\frac{(L_0^{\mathrm{fl}})^2\,\beta_{\max}^{\mathrm{fl}}}{\tau}\right)\hat{T}_{\mathrm{MTU}} - \left(\frac{\beta_j}{\tau}\right)\hat{T}_{\mathrm{pass}} - T_{\mathrm{grav}}\,,$$

and dividing by the term β_j/τ gives

$$\left(\frac{\tau}{\beta_j}\right)T_{\mathrm{net}} = \left\{\frac{(L_0^{\mathrm{fl}})^2\,\beta_{\max}^{\mathrm{fl}}}{\beta_j}\right\}\hat{T}_{\mathrm{MTU}} - \hat{T}_{\mathrm{pass}} - \left\{\frac{mgl\,\tau}{2\beta_j}\right\}\sin(\theta)\,,$$

where we define the dimensionless parameters μ_c and γ as

$$\mu_c = \frac{(L_0^{\mathrm{fl}})^2\,\beta_{\max}^{\mathrm{fl}}}{\beta_j}\,, \quad \gamma = \frac{mgl}{2\beta_j}\,\tau\,.$$

Additionally, to account for the combined contribution of both MTUs, we extend μ_c to include the extensor MTU. This gives

$$\mu_c = \frac{\beta_{\max}^{\mathrm{fl}}(L_0^{\mathrm{fl}})^2 + \beta_{\max}^{\mathrm{ext}}(L_0^{\mathrm{ext}})^2}{\beta_j}\,,$$

or more generally

$$\mu_c = \frac{\sum_{i=\mathrm{fl},\,\mathrm{ext}}\beta_{\max}^{(i)}\,(L_0^{(i)})^2}{\beta_j}\,.$$

Thus, the nondimensional equation A.12 becomes:

$$\left(\frac{\tau}{\beta_j}\right) T_{\mathrm{net}} = \mu_c\,(\hat{F}_{\mathrm{fl}}\,\hat{r}_{\mathrm{fl}} + \mu_m(\hat{F}_{\mathrm{ext}}\,\hat{r}_{\mathrm{ext}})\,) - \eta_j(\Delta\theta) - \dot{\theta} - \gamma\,(\sin\theta)\,,$$

with

$$\hat{T}_{\mathrm{net}} = \frac{\tau}{\beta_j}\,T_{\mathrm{net}}\,.$$

Finally, including the moment of inertia J and substituting dimensionless variables we obtain

$$\frac{J\ddot{\theta}}{\tau^2} = \frac{\beta_j}{\tau}\,\hat{T}_{\mathrm{net}}\,,$$

where the moment of inertia $\hat{J}$ is defined as

$$\hat{J} = \frac{J}{\beta_j\,\tau}\,.$$

Therefore, the final equation of motion for the joint model variant is

$$\ddot{\theta} = \frac{1}{\hat{J}}\left[\mu_c\,(\hat{F}_{\mathrm{fl}}\,\hat{r}_{\mathrm{fl}} + \mu_m(\hat{F}_{\mathrm{ext}}\,\hat{r}_{\mathrm{ext}})\,) - \eta_j(\Delta\theta) - \dot{\theta} - \gamma\,(\sin\theta)\right]\,. \tag{A.13}$$